HOKKAIDO UNIVERSITY

Title	Study on surface coil arrays for electron paramagnetic resonance imaging
Author(s)	榎本, 彩乃
Degree Grantor	北海道大学
Degree Name	博士(工学)
Dissertation Number	甲第11606号
Issue Date	2014-12-25
DOI	https://doi.org/10.14943/doctoral.k11606
Doc URL	https://hdl.handle.net/2115/57738
Type	doctoral thesis
File Information	Ayano_Enomoto.pdf

Hokkaido University Collection of Scholarly and Academic Papers : HUSCAP

Ph.D. Dissertation

Study on surface coil arrays for electron paramagnetic resonance imaging

Ayano Enomoto

Division of Bioengineering and Bioinformatics
Graduate School of Information Science and Technology
Hokkaido University

19 November 2014

Contents

Chapter 1

Introduction

1.1. Background 5

1.1.1. Free radicals 5
1.1.2. EPR spectroscopy 2
1.1.3. Small-animal EPR imaging 3
1.1.4. Challenges in *in vivo* EPR 5

1.2. Technical limitation of RF coils in EPR 5

1.3. Phased array coil in MRI 7

1.4. Goal of this study 8

1.5. Strategy of the study 9

References 13

Chapter 2

Sequential CW-EPR Image Acquisition with 760-MHz Surface Coil Array

2.1. Introduction 19

2.2. Methods 20

2.2.1. Sequential image acquisition 20
2.2.2. Surface coil array 21
2.2.3 Frequency and impedance matching adjustment 24
2.2.4 EPR imager and image reconstruction 25
2.2.5 Phantom imaging 26

2.3. Results 26

2.3.1. Decoupling of coils 26
2.3.2 Images measured with surface coil array 29

2.4. Discussion 30

2.5. Conclusions 32

References 33

Chapter 3

Four-channel surface coil array for sequential CW-EPR image acquisition

3.1. Introduction 38

3.2. Experimental 40

3.2.1. Configuration of the surface coil array and control circuit 40
3.2.2. Surface coil resonator 42
3.2.3. Coil-selection circuits 45
3.2.4. Phantom imaging 47
3.2.5. *In vivo* EPR imaging 48
3.2.6. Proton NMR imaging 48
3.2.7. Image coregistration 49
3.2.8. Simulation of the penetration of RF magnetic fields 49

3.3. Results 50

3.3.1. Resonator implementation 50
3.3.2. Phantom imaging 51
3.3.3. Mouse imaging 51
3.3.4. Simulated RF magnetic fields 53

3.4. Discussion 54

3.5. Conclusions 58

References 59

Chapter 4

Parallel image-acquisition in CW-EPR imaging with a surface coil array: Proof-of-concept experiments

4.1. Introduction 63

4.2. Methods 64

4.2.1. Multiplexing of EPR detection in the frequency domain 64
4.2.2. Experimental setup 65
4.2.3. EPR spectroscopy 67
4.2.4. Relation between the EPR signal intensity and the incident RF power 67
4.2.5. EPR imaging 68

4.3. Results 68

4.3.1. Decoupling of two resonators 68
4.3.2. EPR spectra in parallel detection 69
4.3.3. EPR signal intensity as a function of incident RF power 70
4.3.4. EPR imaging in parallel detection 71

4.4. Discussion 72

4.5. Conclusion 74

References 76

Chapter 5

Elimination of signal saturation under parallel detection in CW-EPR imaging

5.1. Introduction 79

5.2. Methods 80

5.2.1. Experimental setup 80
5.2.2. Relation between EPR signal intensity and incident RF power 83
5.2.3. Measured SNR with and without the second amplifier 83
5.2.4. Comparison of the SNRs under single feeding and simultaneous feeding 84
5.2.5. Phantom imaging 84
5.2.6. *In vivo* EPR imaging 85
5.2.7. Proton NMR imaging 86
5.2.8. EPR/NMR image co-registration 86

5.3. Results 87

5.3.1. Saturation of EPR signals 87
5.3.2. Effect of removing the second amplifier on the EPR spectrometer 88
5.3.3. Phantom imaging 90
5.3.4. *In vivo* imaging 91

5.4. Discussion 92

5.5. Conclusions 94

References 96

Chapter 6

Four-channel surface coil array for 300-MHz pulsed EPR imaging: Proof-of-concept experiments

6.1. Introduction 99

6.2. Methods 101

6.2.1. 300 MHz spectrometer/imager 101
6.2.2. Individual Surface Coils 103
6.2.3. Chemicals 104
6.2.4. Phantom imaging 105

6.3. Results 106

6.3.1. Phantom imaging 106
6.3.2. *In vivo* imaging 109

6.4. Discussion and conclusions 110
References 112

Chapter 7

Decoupling and remote switching of four-channel coils in 300-MHz pulsed EPR imaging

7.1. Introduction 116
7.2. Methods 117
7.2.1. Configuration of a pulsed EPR imaging system 117
7.2.2. Loop resonator 119
7.2.3. Chemical 121
7.2.4. Phantom imaging 121
7.2.5. *In vivo* mouse imaging 121
7.3. Results 122
7.3.1. Construction of the coil array 122
7.3.2. Phantom imaging 123
7.3.3. *In vivo* imaging 124
7.4. Discussion and Conclusions 125
References 128

Chapter 8 Concluding remarks 130

Publications and Honors 133

Acknowledgements 136

Chapter 1

Introduction

1.1. Background

1.1.1. Free radicals

Free radicals are atoms or molecules that have one or more unpaired electrons, and thus are unstable and highly reactive. In living systems, free radicals, including reactive oxygen species (ROS) and reactive nitrogen species (RNS), are generated intracellularly as a result of various biological processes such as aerobic metabolism and biological defense mechanisms. They also play important roles as second messengers in various signal transduction pathways [1.1,1.2]. Free radicals are thus essential for living systems to maintain their biological functions [1.3]. In general, the concentration of free radicals in living systems is kept at appropriate levels by several antioxidant defense systems. Outside of these levels, free radicals can seriously damage deoxyribonucleic acid (DNA) strands, proteins, and lipids [1.4-1.6]. When the concentration of free radicals increases and exceeds the capacity of antioxidant defense systems, as a result of ischemia and reperfusion, ultraviolet (UV) exposure, or other conditions, this can lead to a state called oxidative stress [1.7]. Oxidative stress induces aging, cellular disorder, and a variety of diseases such as cancer and brain dysfunction [1.6,1.8-1.10]. Thus, the distribution and dynamics of free radicals in a living system are very important for understanding such biological phenomena and diseases.

Free radicals can be detected by various methods, including chemical assay, and luminescence and fluorescence techniques [1.11-1.13]. Although these methods offer advantages in terms of sensitivity and specificity, some of the chemical probes used in these methods may interfere with the status of reduction, and may themselves generate ROS. In addition, these probes might not be stable under some conditions [1.13]. Therefore, it can be

difficult to determine the distribution of free radicals with a very short lifetime. Moreover, non-invasive measurement techniques are required to detect free radicals in living systems. In addition to these other methods for detecting free radicals, electron paramagnetic resonance (EPR) spectroscopy can detect free radicals in animals non-invasively. Although it is difficult to observe endogenous free radicals, exogenous probes such as nitroxyl radicals have been widely used in the EPR method.

1.1.2. EPR spectroscopy

Figure 1.1 illustrates the concept of EPR. When an electron spins under a static magnetic field, its energy states split into two levels due to the Zeeman effect. The spins at a low energy level are called beta spins and the direction of their magnetic moments are parallel to the static magnetic field. In contrast, the spins at a high energy level are called alpha spins, and the directions of their magnetic moments are antiparallel to the direction of the magnetic field. There is an energy gap between the alpha spins and beta spins. When beta spins absorb microwave energy that is the same as the energy gap between the two spins, they are excited

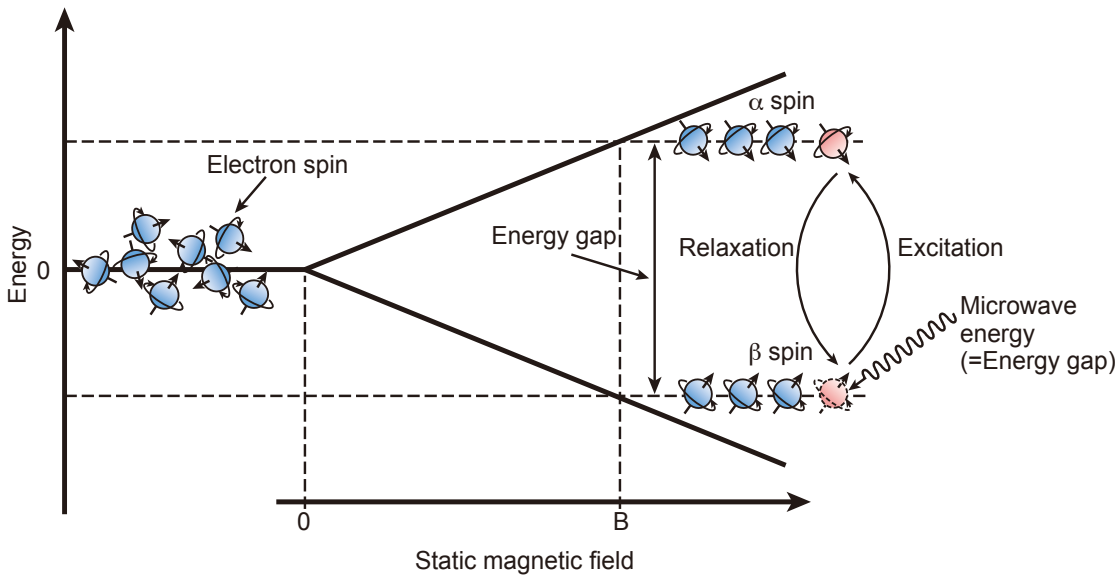


Fig. 1.1. Schematic of the concept of EPR.

and transition to alpha spins. EPR spectroscopy observes this spin transition.

1.1.3. Small-animal EPR imaging

Since the EPR method can be used to detect the free radicals in living organisms non-invasively, it is suitable for *in vivo* EPR measurements. Moreover, it enables us to determine the distribution of free radicals. Visualization of the distribution of free radicals is useful for understanding the mechanisms of free radical-related phenomena or diseases. Thus, progress in EPR imaging techniques with respect to fast data acquisition and the high-resolution imaging of a broader region is highly desirable in free-radical-related studies.

In *in vivo* EPR imaging, operating frequencies ranging from 250 MHz to 1.2 GHz have been used because of the penetration depth of microwaves in an animal body and the sensitivity of EPR detection [1.14]. The sensitivity of EPR detection can be improved with higher frequencies, since the energy gap caused by the Zeeman effect is larger than that with low frequencies. The penetration depth of electromagnetic waves is given by

$$\delta = \sqrt{\frac{2}{2\pi f \mu \sigma}} \tag{1.1}$$

where f is the microwave frequency, μ is the permeability, and σ is the conductivity. In addition, the dielectric loss is generally higher in animal tissues, which have a high dielectric constant. Figure 1.2 shows the relationship between the depth of penetration of RF in different types of human tissue and the microwave frequency (from reference [1.15]). According to Figure 1.2, the penetration depth is approximately 4 cm in muscle at 500 MHz. Thus, a microwave frequency that is as low as possible is required in terms of the penetration depth into animal tissues. However, since EPR spectroscopy with a low frequency leads to a decrease in the sensitivity of EPR signals, the frequencies used in *in vivo* EPR measurements are determined by the trade-off between the sensitivity and the penetration depth.

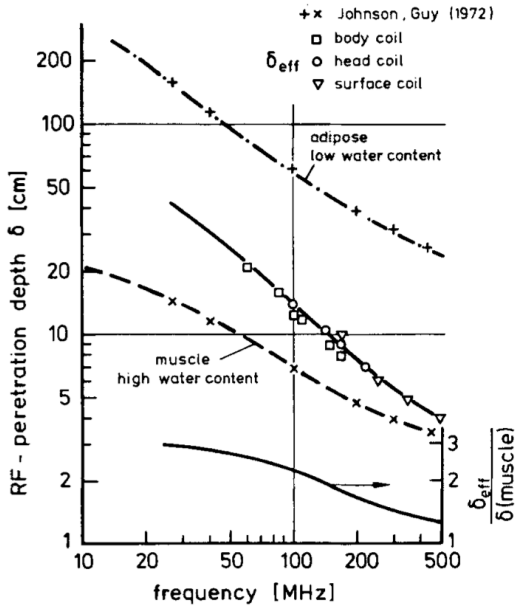


Fig. 1.2. The effective depth δ_{eff} of magnetic field penetration into a human body as a function of frequency. The solid curve at the bottom represents the ratio δ_{eff}/δ (muscle) Reprinted from *Med. Phys.*, Vol. 14 (6), P. Röschmann, Radiofrequency penetration and absorption in the human body: Limitations to high field wholebody nuclear magnetic resonance imaging, pp. 922-931. Copyright 1987, with permission from The American Association of Physicists in Medicine.]

The method of spin-trapping is often used in EPR spectroscopy to detect free radicals with short half-lives [1.16]. The half-lives of free radicals in a living system such as hydroxyl radicals and superoxides range from several nanoseconds to several microseconds, which is too short to observe directly by EPR spectroscopy. In spin-trapping, spin traps react with target free radicals and form stable adducts. As a result, it becomes possible to detect the target free radicals using EPR spectroscopy. However, since the rate of free radical formation in living systems is too low for *in vivo* EPR spectroscopy, even if spin-trapping is applied to *in vivo* EPR measurements, it is still very challenging to detect endogenous free radicals directly due to the low sensitivity of EPR detection [1.17]. Although there have been some reports on the detection of free radicals through the use of spin-trapping in live animals, these experiments were performed in the presence of many free radicals induced by some stimulus, such as exposure of the subjects to UV light [1.18]. EPR measurements have also been

performed indirectly with the use of spin probes or spin labels [1.19]. EPR spectroscopy is also useful for mapping of the partial pressure of oxygen (pO_2) and pH in biological tissues [1.20-1.22], which are important for investigating the physiological status and therapies for various diseases.

1.1.4. Challenges in in vivo EPR

As mentioned above, EPR spectroscopy and imaging are useful for determining the distribution of free radicals in animals. However, *in vivo* EPR spectroscopy presents several challenges. First, the visualization area is limited due to the limitation of the coil size of the RF resonator. This limitation becomes a disadvantage in EPR imaging for the whole body of larger animals like pigs or the skin of humans. Another limitation is the acquisition time. Although the half-lives of spin probes are long enough for use in EPR, those of some spin probes are still too short to obtain three-dimensional (3D) image data due to the reduction reaction of the spin probes in living systems [1.23]. Finally, EPR imaging can show low spatial resolution due to a lack of detection sensitivity or a broad linewidth in EPR absorption spectra [1.24].

1.2. Technical limitation of RF coils in EPR

For *in vivo* EPR measurements, two types of resonators have been used, i.e., volume-coil and surface-coil resonators (Fig. 1.3) [1.25-1.28]. While a volume coil such as a loop-gap resonator has ~~a~~ good RF homogeneity in the coil, the size of the subject is limited to the diameter of the coil [1.26]. In contrast, with a surface coil, while the visualization area is limited to the size of the surface coil, as with a volume coil, there are no constraints on the size or shape of the subject. In addition, the sensitivity of EPR detection on the surface of subjects is greater than that with a volume coil, since the RF magnetic field B_1, for exciting

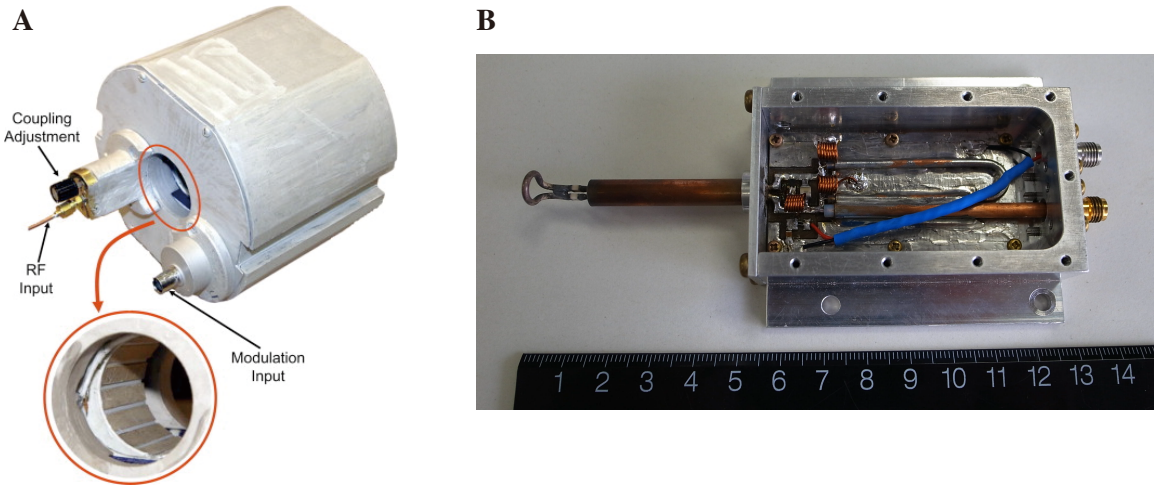


Fig. 1.3. Two types of resonator used for EPR imaging. (A) Volume-type resonator [Reprinted from *J. Magn. Reson*., Vol. 188, S. Petryakov, A. Samouilov, E. Kesselring, T. Wasowicz, G. L. Caia, J. L. Zweier, Single loop multi-gap resonator for whole body EPR imaging of mice at 1.2 GHz, pp. 68-73. Copyright 2007, with permission from Elsevier] (B) Surface coil resonator [© 2014 IEEE. Reprinted, with permission, from H. Sugawara, H. Hirata, S. Petryakov, P. Lesniewski, B. B. Williams, A. B. Flood, H. M. Swartz, Design and evaluation of a 1.1-GHz surface coil resonator for electron paramagnetic resonance-based tooth dosimetry, IEEE Transactions on Biomedical Engineering, June, 2014]

electron spins, generated with a surface coil is greater than that for a volume coil.

The coils should be small in comparison to the wavelength of the electromagnetic waves at the operating frequencies used. *In vivo* EPR spectroscopy and imaging typically use frequencies from 250 MHz to 1.2 GHz [1.14]. This frequency range allows the sufficient penetration of electromagnetic waves in biological tissue, and minimizes tissue heating due to RF absorption. However, this requirement is a compromise with the need to achieve higher sensitivity, which generally requires higher microwave frequencies. This work used RF electromagnetic waves at two different frequencies: 750 MHz for continuous-wave (CW)-EPR and 300 MHz for pulsed EPR. Furthermore, even if the diameter of the coil is smaller than the wavelength at the operating frequency used, a coil with a larger diameter is less efficient at generating an RF magnetic field and results in the inhomogeneity of RF magnetic fields.

As a consequence, further studies are needed to expand the visualization area with both a volume coil and a surface coil. For example, to overcome the limitation of the coil dimensions, Petryakov *et al*. developed a larger surface coil resonator that operated at 1.1 GHz using four loop segments [1.29]. They also reported a single-loop multi-gap resonator for a whole-body mouse at 1.2 GHz [1.26]. Since a large single loop cannot provide a homogeneous signal intensity over a broad region of the subject surface, a surface coil array is a suitable approach for measuring a broader region near the subject surface, such as the skin of a subject animal.

1.3. Phased array coil in MRI

Surface coil arrays have been studied for a long time for use in MRI [1.30-1.34]. In the early history of MRI, a switched surface coil array for a single receiver was first proposed to reduce the total image acquisition time required for an area that could not be covered by a single coil [1.31]. A phased array coil that uses multiple receivers was suggested by Roemer *et al*. in 1990 [1.32], and is now being used clinically. A phased array coil makes it possible to achieve a high signal-to-noise ratio (SNR), better resolution, and a large field-of-view (FOV) without an increase in the data acquisition time [1.32]. The main technical problem with a phased array coil is coupling between the coils. Roemer *et al.* eliminated the interaction of coils by overlapping the coils and using a low-input impedance preamplifier to eliminate interference with other coils [1.32]. Since then, phased array coils have been studied from various perspectives, such as the decoupling method, shape and sensitivity [1.35-1.37]. For example, many improvements in the pulse sequence used for parallel imaging to accelerate data acquisition with a phased array coil have been proposed [1.38,1.39]. Furthermore, phased array coils have been developed to optimize the homogeneity, sensitivity and overall shape of the coils for specific body parts such as the

spinal cord, wrist, breast, and brain [1.40–1.43]. With these improvements in phased array coils, many techniques for minimizing mutual coupling between coils have also been proposed to obtain better image data [1.44].

1.4. Goal of this study

The main purpose of this study was to establish methods for using a surface coil array in EPR imaging, with a main goal of achieving a larger visualization area. With a larger visualization area of free radicals, it may be possible to expand the applicability of EPR imaging to large animals and human organs.

Two methods of EPR detection, i.e., CW-EPR and pulsed EPR, have been used with a surface coil array. CW-EPR and pulsed EPR differ with respect to the characteristics of the resonator. A high quality factor (Q factor) is required for the resonator in CW-EPR to generate higher RF magnetic fields B_1 that excite electron spins, as in $B_1^2 \propto Q\eta\sqrt{P}$ (1.2) where η and P represent the filling factor and the applied input power, respectively. The Q factor for resonators in pulsed-EPR should be set low enough to reduce the ringing that causes dead time [1.45]. Due to this difference, it is necessary to develop surface coil arrays that are appropriate for each type of EPR system.

For the development of a surface coil array for use in an EPR imager, different techniques are required apart from those that are already used in MRI. Although there have been many reports on the use of a surface coil array in MRI, the use of a surface coil array in MRI cannot be directly applied to CW-EPR imaging due to the difference in the signal detection system. In modern MRI, the transmit channel for nuclear-spin excitation and the receive channels for signal detection are separated from each other. Thus, in MRI, multiple receiver channels can be used in a phased array coil without increasing the number of transmit channels. However, in commonly used reflection-type RF bridges in CW-EPR

spectrometers, electromagnetic waves for electron-spin excitation and reflected waves that are modulated due to EPR absorption pass through the same transmission line. Hence, the phased array coil system used in MRI has not been used in CW-EPR imaging. In contrast, since the method used for signal detection in pulsed EPR is similar to that in MRI, it may be possible, at least in principle, to apply a surface coil array used in MRI to a pulsed EPR system. However, in contrast to modern MRI, there is only one receiver channel in a pulsed EPR system. Although it may be possible to increase the number of receiver channels, this has not yet been reported. Thus, a surface coil array for one receiver channel should be constructed for use in a conventional pulsed EPR system. Although the use of a switched surface coil array with one receiver channel has been reported in MRI, decoupling with this switched surface coil array is achieved by arranging the coils far enough apart to suppress the interaction between coils. However, for parallel imaging in pulsed EPR imaging, it would be desirable to construct a surface coil array that uses a surface coil similar to the phased coil array in MRI. Thus, it is important to develop a surface coil array for use in both CW-EPR and pulsed EPR.

1.5. Strategy of the study

The main problem in the development of a surface coil array is mutual inductive coupling between adjacent coils. Figure 1.4 presents the author's strategy for how to overcome this technical challenge. The ultimate goal of this study was to establish a surface coil array to achieve a large visualization area in EPR imaging. An important technical challenge is decoupling of the coils. Two methods were used to achieve the goal of this study: multiplexing in the time domain and multiplexing in the frequency domain. These methods of multiplexing were applied to both CW-EPR spectroscopy and pulsed EPR spectroscopy as follows:

(1) Sequential data acquisition for CW-EPR (multiplexing in the time domain for CW-EPR)

To suppress mutual coupling between the coils of a surface coil array, the resonance frequency of individual resonators is shifted far from the operating frequency when they are not driven. Data acquisition is performed sequentially by switching the channel that corresponds to the resonator. The channels are electrically switched by PIN-diodes. To verify the feasibility of this method, a two-channel surface coil array was first constructed. This array was controlled manually. Next, a four-channel surface coil array with automatic switching was constructed and used in EPR imaging with mice. To achieve automatic data acquisition, a switching circuit was also developed for use with this four-channel surface coil array.

(2) Parallel data acquisition for CW-EPR (multiplexing in the frequency domain)

Although sequential acquisition by the multiplexing of EPR detection in the time domain can be applied to CW-EPR, the acquisition time can be expected to increase in proportion to the number of coils. Since a long acquisition time is a disadvantage for *in vivo* EPR imaging, a parallel imaging method is required. In CW-EPR, the author used multiple frequencies to suppress mutual inductive coupling between the coils; i.e., the multiplexing of EPR detection in the frequency domain. To verify the feasibility of parallel data acquisition by multiplexing in the frequency domain, a two-channel surface coil array was developed separately from that used in sequential data acquisition. Both spectral acquisition and imaging of a phantom and mice were performed with the parallel detection scheme. However, this method could not be applied to pulsed EPR imaging because the operating frequency in a pulsed EPR system is fixed at a specific frequency.

(3) Sequential data acquisition for pulsed EPR (multiplexing in the time domain for pulsed

EPR)

A surface coil array that used the multiplexing of EPR detection in the time domain was also expected to be applicable to pulsed EPR. However, since a higher incident RF power is used in pulsed EPR, it was difficult to use the small signal solid-state elements that are used for automatic acquisition in CW-EPR. Thus, a different switching technique was required. First, a surface coil array that is robust to a high RF power was developed for 300 MHz pulsed EPR. Next, sequential EPR data acquisition was performed manually for both a phantom and mice.

Although sequential data acquisition can be performed by manual switching, remote switching is more desirable to reduce both the switching time and complications associated with switching. Since it is difficult to use the same electronic components for remote switching, such as PIN diodes, another method was needed to suppress mutual coupling between the coils. To achieve remote switching in a pulsed EPR imager, sequential data acquisition without a shift in the resonant frequency was achieved in this study. To suppress the interaction between coils, the author used the characteristics of a conventional resonator for pulsed EPR, i.e., a low Q factor, to reduce the dead time [1.45]. In addition to a low Q factor, a low coupling coefficient due to the arrangement of the coils was also used to suppress mutual inductive coupling between the coils.

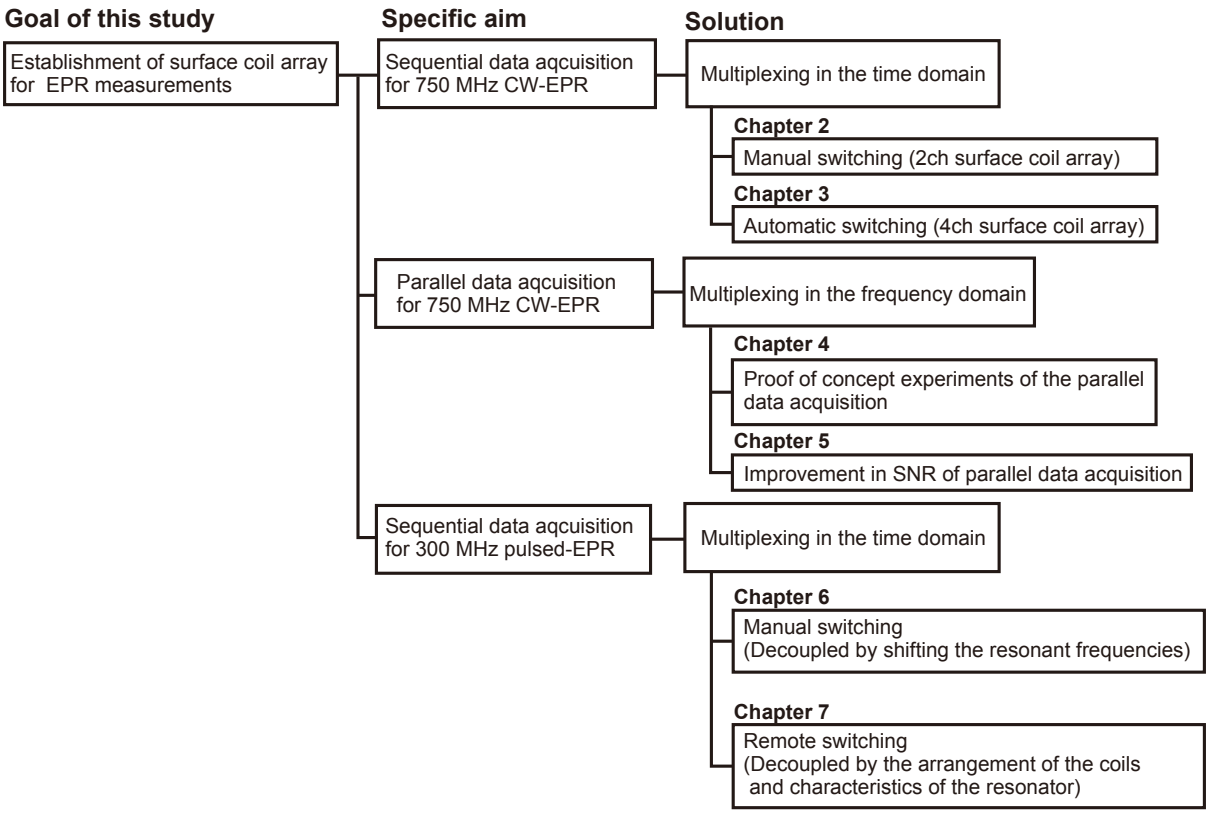


Fig. 1.4. Overview of the strategy in this study.

References

[1.1] J. L. Zweier, M. A. H. Talukder, The role of oxidants and free radicals in reperfusion injury, Cardiovasc. Res. 70 (2006) 181–190.

[1.2] M. Valko, D. Leibfritz, J. Moncol, M. T. D. Cronin, M. Mazur, J. Telser, Free radicals and antioxidants in normal physiological functions and human disease, Int. J. Biochem. Cell Biol. 39 (2007) 44–84.

[1.3] P. D. Ray, B-W. Huang, Y. Tsuji, Reactive oxygen species (ROS) homeostasis and redox regulation in cellular signaling, Cell. Signal. 24 (2012) 981–990.

[1.4] M. L. Circu, T. Y. Aw, Reactive oxygen species, cellular redox systems, and apoptosis, Free Radic. Biol. Med. 48 (2010) 749–762.

[1.5] M. Dizdaroglu, P. Jaruga, M. Birincioglu, H. Rodriguez, Free radical-induced damage to DNA: mechanisms and measurement, Free Radic. Biol. Med. 32 (2002) 1102–1115.

[1.6] M. Valko, M. Izakovic, M. Mazur, C. J. Rhodes, J. Telser, Role of oxygen radicals in DNA damage and cancer incidence, Mol. Cell. Biochem. 266 (2004) 37–56.

[1.7] J. L. Martindale, N. J. Holbrook, Cellular response to oxidative stress: signaling for suicide and survival, J. Cell. Physiol. 192 (2002) 1–15.

[1.8] B. N. Ames, M. K. Shigenaga, T. M Hagen, Oxidants, antioxidants, and the degenerative diseases of aging, Proc. Natl. Acad. Sci. U.S.A. 90, (1993) 7915–7922.

[1.9] D. Dreher, A. F. Junod, Role of oxygen free radicals in cancer development, Eur. J. Cancer. 32 (1996) 30–38.

[1.10] M. A. Smith, C. A. Rottkamp, A. Nunomura, A. K. Raina, G. Perry, Oxidative stress in Alzheimer's disease, Biochim. Biophys. Acta-Mol. Basis Dis. 1502, 26 (2000) 139–144.

[1.11] M. M. Tarpey, D. A. Wink, M. B. Grisham, Methods for detection of reactive

metabolites of oxygen and nitrogen: in vitro and in vivo considerations, Am. J. Physiol. Regul. Integr. Comp. Physiol. 286 (2004), R431–R444.

[1.12] C. Rota, Y. C. Fann, R. P. Mason, Phenoxyl free radical formation during the oxidation of the fluorescent dye 2,7-dichlorofluorescein by horseradish peroxidase: Possible consequences for oxidative stress measurements, J. Biol. Chem. 274 (1999) 28161–28168.

[1.13] M. B. Grisham, Methods to detect hydrogen peroxide in living cells: Possibilities and pitfalls, Comp. Biochem. Physiol. Part A: Mol. Integr. Physiol. 165 (2013) 429–438.

[1.14] G. R Eaton, S. S. Eaton, EPR spectrometers at frequencies below X-band, in: C. J. Bender, L. J. Berliner (Eds.), Biological Magnetic Resonance Vol. 21, Kluwer Academic/Plenum Publishers, New York, 2004, pp. 59–114.

[1.15] P. Röschmann, Radiofrequency penetration and absorption in the human body: Limitations to high-field whole-body nuclear magnetic resonance imaging. Med. Phys. 14 (1987) 922–931.

[1.16] R. P. Mason, M. B. Kadiiska, In vivo spin trapping of free radical metabolites of drugs and toxic chemicals utilizing ex vivo detection, in: S. R. Eaton, G. R. Eaton, L. J. Berliner (Eds.), Biological Magnetic Resonance Vol. 23, Kluwer Academic/Plenum Publishers, New York, 2005, pp. 93–109.

[1.17] G. S. Timmins, K. J. Liu, Spin trapping in vivo: facts and artifacts, in: L. J. Berliner (Ed.), Biological Magnetic Resonance Vol. 18, Kluwer Academic/Plenum Publishers, New York, 2005, pp. 285–308.

[1.18] K. Takeshita, C. Chi, H. Hirata, M. Ono, T. Ozawa, In vivo generation of free radicals in the skin of live mice under ultraviolet light, measured by L-band EPR spectroscopy, Free Radic. Biol. Med. 40 (2006) 876–885.

[1.19] B. B. Williams, H. J. Halpern, In vivo EPR imaging, in: S. R. Eaton, G. R. Eaton, L. J.

Berliner (Eds.), Biological Magnetic Resonance Vol. 23, Kluwer Academic/Plenum Publishers, New York, 2005, pp. 283–319.

[1.20] A. A. Bobko, T. D. Eubank, J. L. Voorhees, O. V. Efimova, I. A. Kirilyuk, S. Petryakov, D. G. Trofimiov, C. B. Marsh, J. L. Zweier, I. A. Grigor'ev, A. Samouilov, V. V. Khramtsov, In vivo monitoring of pH, redox status, and glutathione using L-band EPR for assessment of therapeutic effectiveness in solid tumors, Magn. Reson. Med. 67, 1827–1836.

[1.21] S. Subramanian, K. Yamada, A. Irie, R. Murugesan, J. A. Cook, N. Devasahayam, G. M. Van Dam, J. B. Mitchell, M. C. Krishna, Noninvasive in vivo oximetric imaging by radiofrequency FT EPR, Magn. Reson. Med. 47 (2002) 1001–1008.

[1.22] J. Goodwin, K. Yachi, M. Nagane, H. Yasui, Y. Miyake, O. Inanami, A. A. Bobko, V. V. Khramtsov, H. Hirata, *In vivo* tumour extracellular pH monitoring using electron paramagnetic resonance: the effect of X-ray irradiation, NMR Biomed. 27(2014) 453–458.

[1.23] A. C. Kulkarni, A. Bratasz, B. Rivera, M. C. Krishna, P. Kuppusamy, mapping of biological samples using EPR imaging, Israel J. Chem. 48(2008) 27–31.

[1.24] P. Kuppusamy, M. Chzhan, J. L. Zweier, Principle of imaging, in: L. J. Berliner (Ed.), Biological Magnetic Resonance Vol. 18, Kluwer Academic/Plenum Publishers, New York, 2005, pp. 99–152.

[1.25] W. Froncisz, J. S. Hyde, The loop-gap resonator: a new microwave lumped circuit ESR sample structure, J. Magn. Reson. 47 (1982) 515–521.

[1.26] S. Petryakov, A. Samouilov, E. Kesselring, T. Wasowicz, G. L. Caia, J. L. Zweier, Single loop multi-gap resonator for whole body EPR imaging of mice at 1.2 GHz, J. Magn. Reson. 188 (2007) 68–73.

[1.27] H. Sugawara, H. Hirata, S. Petryakov, P. Lesniewski, B. B. Williams, A. B. Flood, H.

M. Swartz, Design and evaluation of a 1.1 GHz surface coil resonator for electron paramagnetic resonance-based tooth dosimetry, IEEE Trans. Biomed. Eng. 61 (2014) 1894–1901.

[1.28] G. He, S. P. Evalappan, H. Hirata, Y. Deng, S. Petryakov, P. Kuppusamy, J. L. Zweier, Mapping of the B_1 field distribution of a surface coil resonator using EPR imaging. Magn. Reson. Med. 48 (2002) 1057–1062.

[1.29] S. Petryakov, A. Samouilov, M. Chzhan-Roytenberg, E. Kesselring, Z. Q. Sun, J. L. Zweier, Segmented surface coil resonator for in vivo EPR applications at 1.1 GHz, J. Magn. Reson. 198 (2008) 8–14.

[1.30] D. Kwiat, S. Einav, G. Navon, A decoupled coil detector array for fast image acquisition in magnetic resonance imaging, Med. Phys. 18 (1991) 251–265.

[1.31] J. S. Hyde, A. Jesmanowicz, W. Froncisz, J. B. Kneeland, T. M. Grist, Parallel image acquisition from noninteracting local coils, J. Magn. Reson. 70 (1986) 512–517.

[1.32] P. B. Roemer, W. A. Edelstein, C. E. Hayes, S. P. Souza, O. M. Mueller, The NMR phased array, Magn. Reson. Med. 16 (1990) 192–225.

[1.33] M. A. Ohliger, D. K. Sodickson, An introduction to coil array design for parallel MRI, NMR Biomed. 19 (2006) 300–315.

[1.34] D. J. Larkman, R. Nunes, Parallel magnetic resonance imaging, Phys. Med. Biol. 52 (2007) R15–R55.

[1.35] J. Cohen-Adad, A. Mareyam, B. Keil, J. R. Polimeni, L. L. Wald, 32-channel RF coil optimized for brain and cervical spinal cord at 3 T, Magn. Reson. Med. 66 (2011) 1198–1208.

[1.36] V. S. Lee, E. M. Hecht, B. Taouli, Q. Chen, K. Prince, N. Oesingmann, Body and cardiovascular MR imaging at 3.0 T, Radiology 244 (2007) 692–705.

[1.37] A-L. Perrier, J-C. Goebel, A. Pinzano-Watrin, E. Roeder, P. Gillet, D. Grenier, O.

Beuf, Design of a four-channel surface receiver coil array without preamplifiers for the decoupling between elements: Validation for high-resolution rat knee MR imaging, IEEE Sensors J. 13 (2013) 2450–2458.

[1.38] K. P. Pruessmann, M. Weiger, M. B. Scheidegger, P. Boesiger, SENSE: Sensitivity encoding for fast MRI, Magn. Reson. Med. 42 (1999) 952–962.

[1.39] M. A. Griswold, P. M. Jakob, R. M. Heidemann, M. Nittka, V. Jellus, J. Wang, B. Kiefer, A. Haase, Generalized autocalibrating partially parallel acquisitions (GRAPPA), Magn. Reson. Med. 47 (1999) 1202–1210.

[1.40] J. D. Kaggie, J. R. Hadley, J. Badal, J. R. Campbell, D. J. Park, D. L. Parker, G. Morrell, R. D. Newbould, A. F. Wood, N. K. Bangerter, A 3 T sodium and proton composite array breast coil, Magn. Reson. Med. 71 (2014) 2231–2242.

[1.41] O. Kraff, A. K. Bitz, S. Kruszona, S. Orzada, L. C. Schaefer, J. M. Theysohn, S. Maderwald, M. E. Ladd, H. H. Quick, An eight-channel phased array RF coil for spine MR imaging at 7 T, Invest. Radiol. 44 (2009) 734–740.

[1.42] J. A. Nordmeyer-Massner, M. Wyss, G. Andreisek, K. P. Pruessmann, J. Hodler, In vitro and in vivo comparison of wrist MR imaging at 3.0 and 7.0 tesla using a gradient echo sequence and identical eight-channel coil array designs, J. Magn. Reson. Imaging. 33 (2011) 661–667.

[1.43] J. Cohen-Adad, A. Mareyam, B. Keil, J. R. Polimeni, L. L. Wald, 32-channel RF coil optimized for brain and cervical spinal cord at 3 T, Magn. Reson. Med. 66 (2011) 1198–1208.

[1.44] S. M. Wright, L. L. Wald, Theory and application of array coils in MR spectroscopy, NMR Biomed. 10 (1997) 394–410.

[1.45] S. Subramanian, J. B. Mitchell, M. C. Krishna, Time-domain radio frequency EPR imaging, in: L. J. Berliner (Ed.), Biological Magnetic Resonance Vol. 18, Kluwer

Academic/Plenum Publishers, New York, 2005, pp. 153–200.

Chapter 2

Sequential CW-EPR Image Acquisition with 760-MHz Surface Coil Array

2.1. Introduction

Electron paramagnetic resonance (EPR) imaging is an important technique to detect free radicals in subject animals noninvasively [2.1]. It is widely recognized that free radicals are associated with many diseases, such as inflammation and ischemia/reperfusion injury [2.2,2.3]. Therefore, the visualization of the distribution of free radicals in small animals is useful to understand the mechanisms of free-radical-related diseases. In EPR imaging, typically two types of resonators have been used, namely, volume-coil [2.4–2.9] and surface-coil resonators [2.10–2.12]. The dimensions of the coils are small in comparison to the wavelength of the operation frequencies of *in vivo* EPR spectroscopy and imaging, which typically range from 250 MHz to 1.2 GHz [2.13,2.14]. This frequency range is chosen to allow sufficient penetration in biological tissue, and to minimize tissue heating due to RF absorption. However this requirement is a compromise with the need to obtain higher sensitivity, which is generally achieved with higher microwave frequencies [2.15]. To overcome the constraints of resonator size imposed by frequency requirements, Petryakov *et al*. developed a larger surface coil resonator with a 1.1 GHz operation frequency, by combining four identical loop segments [2.16]. Similarly, phased-array coils have been utilized in proton magnetic resonance imaging (MRI) [2.17–2.19], and applied clinically for visualization of large regions of interest such as human spine [2.20]. However, one of the main obstacles to the use of the arrayed coil design in MRI and EPR imaging, is the need to suppress the mutual coupling, or inductive interaction of the coils [2.21].

Preliminary surface coil array designs for CW-EPR imaging, are similar to MRI coil arrays in that they are both designed to extend the area of visualization, however there are a

number of fundamental differences between MRI and CW-EPR scanning techniques, primarily related to the method of signal detection. As such, in developing surface coil arrays for CW-EPR imaging, the following considerations must be addressed:

(i) The imaging sample and the resonator(s) are exposed to magnetic field modulation in CW-EPR detection. MRI does not use low frequency (~100 kHz) magnetic field modulation. Therefore, decoupling circuits should be situated away from region of magnetic field modulation to avoid interference at low modulation frequencies.

(ii) Since the resonator is constantly driven in CW-EPR imaging, the microwave carrier frequency or the resonance frequency of the resonator(s) should be controlled to make the reflected microwaves from the resonator minimal by a negative feedback control system.

The goal of this work was to demonstrate the feasibility of the surface coil array for CW-EPR imaging that can extend the area of visualization of the surface coils. By shifting the resonance frequency of one of the surface coil resonators with a PIN-diode switch, the author was able to suppress mutual coupling and extend the area of visualization of EPR imaging.

2.2. Methods

2.2.1. Sequential image acquisition

As illustrated in Fig. 2.1, the surface coil array consists of two surface coil resonators and two kinds of switches, i.e., RF coaxial (919C70100, Transco Products Inc., Camarillo, CA) and PIN-diode switches. When the PIN-diode switch in the resonator circuit is turned on, the resonance frequency of the resonator is shifted, thereby suppressing the mutual coupling due to the difference in the resonance frequencies of the two circuits. EPR data acquisition was sequentially performed for each resonator, such that when obtaining measurements with

the first resonator, microwaves were not fed to the second resonator. This was achieved using low resistance PIN-diodes, causing a shift in the resonance frequency of the second resonator. After imaging with the first resonator, the process was repeated by connecting the second resonator to the EPR bridge, allowing images to be acquired with the second resonator.

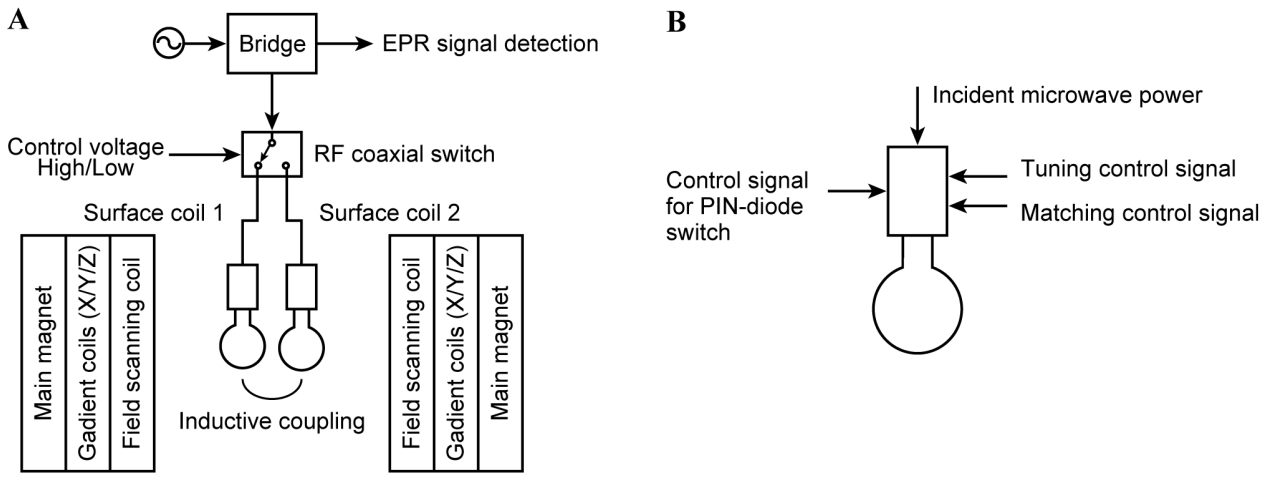


Fig. 2.1. Schematic diagram of surface coil array and a CW-EPR spectrometer. (A) Configuration of two surface coils and an RF coaxial switch. (B) Input signals applied to an individual surface coil.

2.2.2. Surface coil array

Figure 2.2 shows the configuration of the surface coil resonator. The LC resonance circuit was driven through a parallel transmission line, with a matching circuit using varactor diodes connected in parallel to the transmission line [2.22,2.23]. Frequency adjustment was achieved by changing the capacitive reactance using varactor diodes connected in series to the transmission line. The development of the resonator was based largely on a previously reported 300 MHz loop resonator [2.23], with the addition of electronic tuning and matching control functions, which have previously been used in CW-EPR spectrometers [2.8,2.24–2.27]. The substrate of the surface coils was made from copper laminate (DiClad 880, Arlon Inc., Santa Ana, CA), and for impedance matching, frequency tuning, and PIN-diode switch

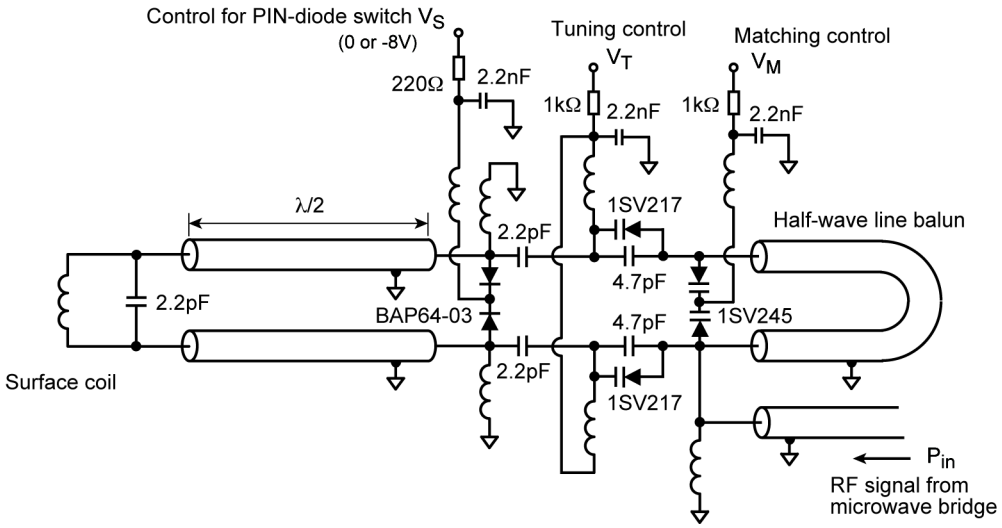


Fig. 2.2. Circuitry diagram of individual surface coil. The PIN-diode switch becomes a low-impedance when the negative voltage (-8 V) is applied to the control port V_S. Decoupling of the coils is achieved by changing the negative voltage on (-8 V) and off (0 V).

circuits, another substrate was used (FR-4, Sunhayato, Tokyo, Japan). The copper laminate on the backside of the substrate of the surface coils was removed, and several coil arrays were constructed, with a coil inner diameter and width of 7 mm and 2 mm respectively. The constructed arrays were fixed onto the substrate, in each case with varying distances between the centers of two coils ranging from 4 mm to 7 mm, resulting in a partial overlap of the coils. To assess the characteristics of the surface coil array when distances between the centers of the coils were greater than 7 mm, two separately fabricated, non-overlapping coils were used. To electrically insulate the coils from each other, polytetrafluoroethylene sheets were inserted into the overlapping regions. The non-magnetic chip capacitors (11-2R2-C-1000-S for 2.2 pF, 11-4R7-C-1000-S for 4.7 pF, Voltronics, Denville, NJ) were used in the tuning and impedance matching circuit to prevent the effect of magnetic field modulation. When the surface coils were exposed to magnetic field modulation, the electromotive force is generated at the frequency of field modulation. If the electromotive force is transferred to the tuning and matching circuits through the coaxial transmission lines, the reverse-bias voltage applied to the varactor diodes is modulated at the frequency of field modulation and it leads to a shift

in the resonance frequency and the reflection of the incident microwaves at the resonator. This effect causes the shift in the baseline of detected EPR spectra. To prevent this unwanted effect of magnetic field modulation, the author used capacitors, which have small capacitance (2.2 pF), connected in series between the transmission lines and the varactor diodes. Because these capacitors have large impedance at the frequency of field modulation (90 kHz), the electromotive force due to magnetic field modulation cannot be transferred to the varactor diodes.

To adjust the tuning and impedance matching electronically, varactor diodes (1SV217 for the tuning circuit, 1SV245 for the matching circuit, Toshiba, Tokyo, Japan) were used in both the tuning and matching circuits. For adjustment of impedance matching, the reverse-bias voltage applied to the varactor diodes was changed. The resonance frequencies of the resonators were adjusted to the microwave carrier frequency, where the adjustable range of the resonance frequency of the resonator was approximately 8 MHz. PIN diodes (BAP64-03, Royal Philips Electronics, Netherland) were used for shifting the resonance frequency of the resonator to decouple the surface coils. By placing PIN diodes between the coaxial lines (Fig. 2.2) and applying a negative voltage, the transmission line was shorted due to the low resistance of the PIN diodes. Thus, the resonance frequency of the resonator was significantly altered due to the change in resonance circuit properties. The parallel transmission line and the half-wave line balun were made from semi-rigid coaxial cables (3.6 mm in diameter and characteristic impedance of 50 Ω, SX-36, Sanken Corp., Tokyo, Japan). The return loss and the quality factor of each resonator were measured with a network analyzer (E5062A, Agilent Technologies, Palo Alto, CA) to check the operation of the surface coil array.

In Figs. 2.3A and 2.3B, the two coils and the complete resonator construction are pictured respectively. Each coil was connected to the end of the transmission line. The frequency tuning and impedance matching circuits were encased in copper housing to prevent interference due to magnetic field modulation, and aluminum plates were inserted into the gap of the resonators to adjust the distance between the coils. The entire length of the resonators including the shielding box was 236 mm. Since the diameter of the coils for magnetic field modulation was 100 mm and the length of transmission line (half-wave line) was 126 mm, the copper shielding case was away from the region of magnetic field modulation. Moreover, the shielding case was placed in the outside of the static magnetic field because the most homogeneous region of the static magnetic field was 30 mm in diameter of spherical volume. Hence, the eddy current problem was not caused with the shielding case made by bulky copper boxes.

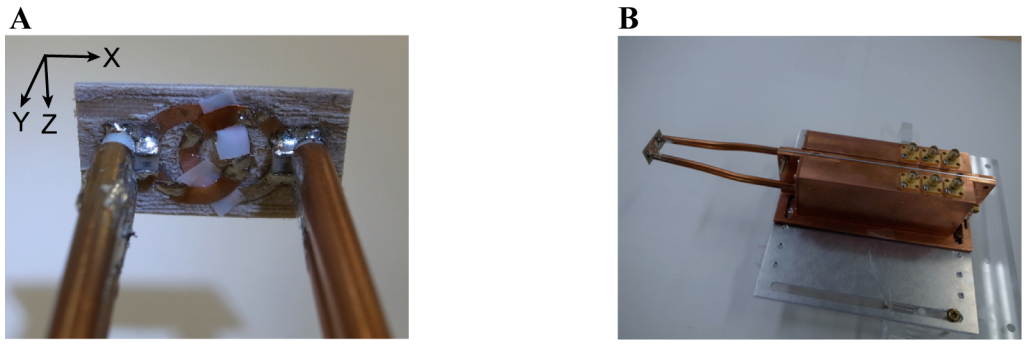


Fig. 2.3. Photographs of surface coils (A) and whole structure of the prototype coil array (B).

2.2.3 Frequency and impedance matching adjustment

To make sequential measurements easier, impedance matching and frequency tuning of the individual resonators were adjusted in advance. The resonance frequencies of the resonators have to be tuned in the lock-in range of automatic tuning control (ATC). However, it is difficult to make multiple resonators with identical characteristics. Since the ATC system can adjust only one resonator, the author built an electrical circuit that selects the resonator

being adjusted in terms of its frequency and impedance matching. Figure 2.4A illustrates a block diagram of the electrical circuits of the frequency and impedance matching adjustment, while in Fig. 2.4B the summing amplifier used for the frequency tuning of the resonators is schematically shown. On the right side of the summing amplifier, the author employed a compensator (lag-lead filter) to prevent the unwanted oscillation of the feedback loop in ATC [2.28]. Before the measurements, the impedance matching of each resonator was adjusted to the 50-ohm coaxial line connected to the EPR bridge.

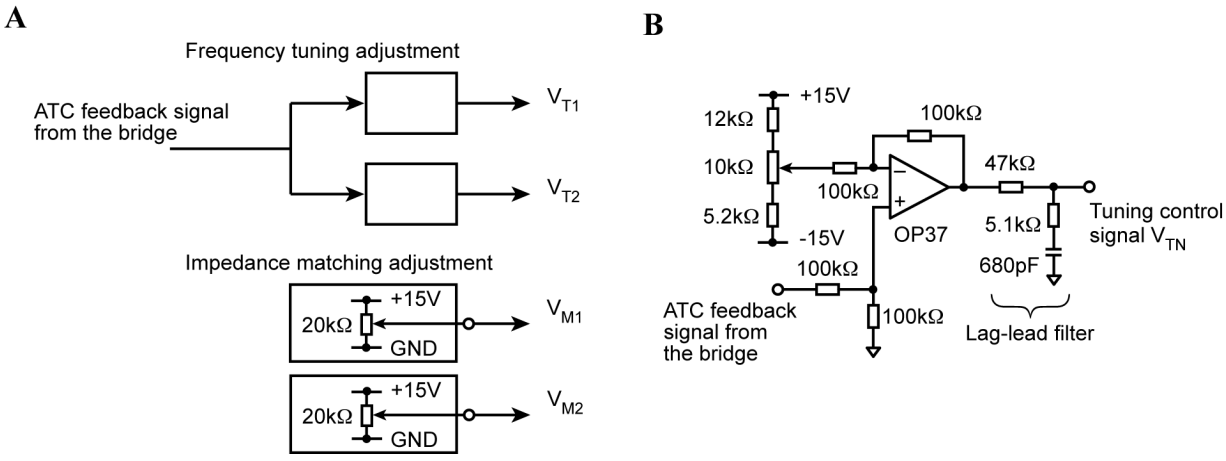


Fig. 2.4. Diagram of voltage adjustment circuits. (A) Block diagram of the adjustment for tuning and matching control voltages. (B) Voltage adjustment circuit for frequency tuning.

2.2.4 EPR imager and image reconstruction

A previously reported laboratory-built 750-MHz CW-EPR imager [2.29,2.30] was used in the experiments, consisting of a set of 3D field gradient coils, with a 60 mm gap between the two magnets. The author used a Helmholtz coil pair with a 50 mm gap as a modulation coil and placed it between the magnets. After acquiring EPR spectra with both resonators, two-dimensional (2D) images were individually reconstructed on the basis of the filtered back-projection algorithm [2.31], and the reconstructed images were combined to form the final image using the "Add" function of ImageJ software (National Institutes of Health,

Bethesda, MD) [2.32].

2.2.5 Phantom imaging

To investigate the area of visualization of the surface coil array, the author measured 2D EPR images of a glass cell phantom (10 × 10 × 45 mm) filled with 4.5mL of a solution of 1mM 4-hydroxy-2,2,6,6-tetramethylpiperidine-d_{17}-1-^{15}N-oxyl (TEMPOL-d_{17}-^{15}N). The distance between the centers of two coils was varied from 4 mm to 7 mm, with a field-of-view (FOV) set to 40 mm. The parameters for EPR imaging were as follows: scanning field 2.0 mT, magnetic field gradient 50 mT/m, magnetic field modulation 0.15 mT, modulation frequency 90 kHz, scan time 1.0 s, time constant 0.3 ms, applied microwave power 20 mW, number of projections 32, with 5 averages, giving a total image acquisition time of 3 min.

2.3. Results

2.3.1. Decoupling of coils

Figure 2.5 shows the characteristics of return loss (scattering matrix parameter S_{11}) measured for an individual surface coil resonator when the PIN-diode switch was off and on. As shown in Fig. 2.5, the resonance frequency of the resonator was shifted from 760 MHz to 1.01 GHz when PIN-diode switch was turned on (the status of low resistance). When the resonance frequencies of the two coils are significantly different from each other, one does not affect the impedance of the other coil. This is because impedance of a non-resonant surface coil is high enough and it leads to less interaction between two resonant circuits, even if the two coils are situated in the proximity of each coil . This is the major cause to decouple the surface coils by using the PIN-diode switch.

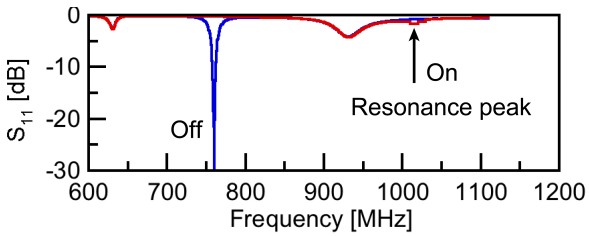


Fig. 2.5. Typical scattering-matrix parameter S_{11} for an individual surface coil resonator when the PIN-diode switch was off and on.

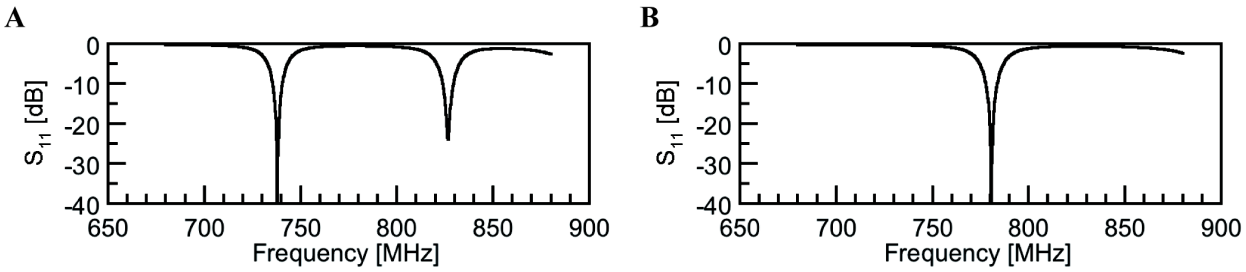


Fig. 2.6. Typical scattering-matrix parameter S_{11} for one of the two resonators in the surface coil array when the PIN-diode switch was off (A) and on (B).

Figure 2.6 shows the typical traces of the return loss of an individual surface coil. As shown in Fig. 2.6A, when the PIN-diode switch of one of two resonators was off, dual-peak resonance appeared, due to the effect of mutual coupling between two coils. Whereas the resonance frequency of the coil that was not driven by the EPR bridge, was shifted more than 200 MHz when the PIN-diode switch of one of two resonators was on, giving a single resonance peak as shown in Fig. 2.6B. This result demonstrates the effectiveness of using the PIN-diode switch (Fig. 2.2) for the suppression of mutual coupling.

Figures 2.7A and 2.7B show the characteristics of the resonance peaks when the distance between the centers of the two coils was varied in a lateral direction (the X-direction in Fig. 2.3A), with the resonance frequency of the resonators set to 760 MHz, for PIN diode off and on conditions respectively. As shown in Fig. 2.7A, under the presence of the mutual coupling, the dual-peak resonance appeared and the frequencies of their peaks deviated away from 760 MHz. When the distance between the two coils was closer, the difference in the

frequencies of their peaks was larger. The motional electromotive force generated in the coil is minus the rate of changing magnetic flux through the coil (Faraday's low). When the distance between the two coils was larger, the flux through the coil obviously became smaller and this results in a smaller motional electromotive force. This means less mutual inductance between the two coils. Because the frequency response curve of inductively coupled resonant circuits (the type of transformer coupling) depends on the amount of coupling [2.33], the frequencies of the dual-peak response vary as a function of the distance between the two coils. However, when the distance between the centers of the coils was 7 mm, the resonance peaks appeared at the same frequency, suggesting an apparent absence of mutual coupling. At the specific geometry of two adjacent coils, their mutual inductance becomes zero and that can eliminate the problem of the dual-peak resonance for the inductively coupled resonant circuits [2.17]. The resonance frequencies at the distance of 7 mm in Fig. 2.7A were the same, and this means that the mutual inductance became small in that geometry of the two coils. This result was consistent to the knowledge in the prior work of NMR array coils. On the other hand, as shown in Fig. 2.7B, when the PIN-diode switch was on and the mutual

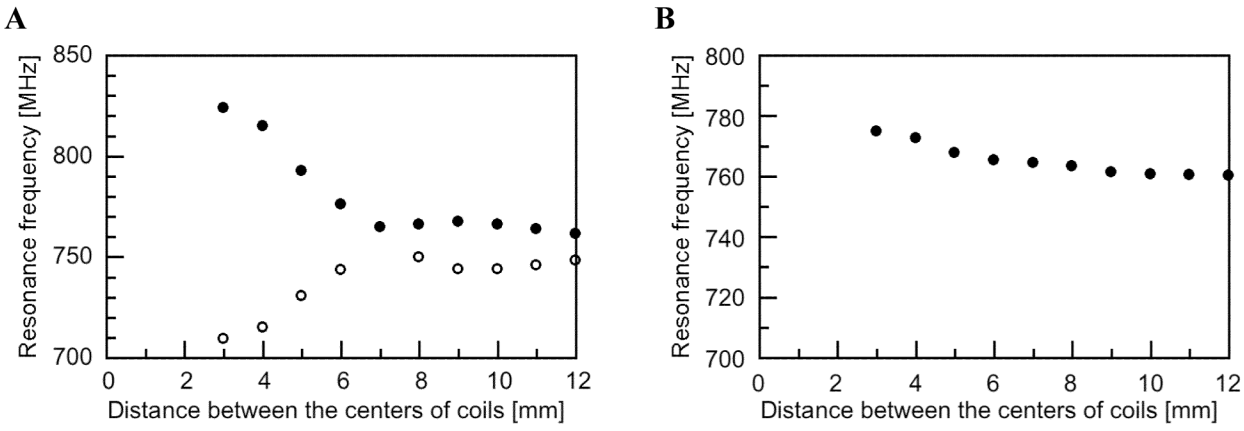


Fig. 2.7. A shift in the resonance frequencies for (A) inductively coupled surface coil and (B) decoupled surface coil. For dual-peak resonance, the frequencies of upper peak (closed circle) and lower peak (open circle) are plotted as a function of the distance between the centers of the coils in Fig. 2.7A. For the decoupled coil, a single peak of resonance appeared, and its resonance frequency was plotted in Fig. 2.7B.

coupling was suppressed, the single resonance peak appeared close to the resonance frequency of 760 MHz, irrespective of the distance between the coils with a maximum frequency difference less than 15 MHz, which decreased as the distance between the coils was increased. Table 2.1 lists the unloaded quality factors of the resonators. The voltage of frequency tuning was set to 8 V, when those parameters were measured.

Table 2.1
Quality factor of individual surface coil resonators.

Distance between coils [mm]	Quality factor	
	Resonator 1	Resonator 2
4	102	100
5	110	105
6	111	107
7	110	104

2.3.2 Images measured with surface coil array

To investigate the area of visualization of the surface coil array, the author measured a glass cell phantom (Fig. 2.8A). Figure 2.8B shows 2D EPR images of the phantom, acquired with a single coil in XY- and XZ-planes. Figures 2.8C and 2.8D show the combined EPR images measured with the surface coil array, with varying distances between centers of the coils. When the distance between the centers of two coils was 7 mm, the distribution of signal intensity was not uniform in both planes. When the distance of coils was greater than 7 mm, the area of visualization was split into two areas that correspond to two non-overlapping coils. In the XZ-plane, the area of visualization was approximately equal to the inner area of the coils, with signal intensity enhancement near the center of each image due to the lens effect [2.34,2.35]. The images in the XY-plane show the sensitivity of depth to be approximately 3 mm in each distance.

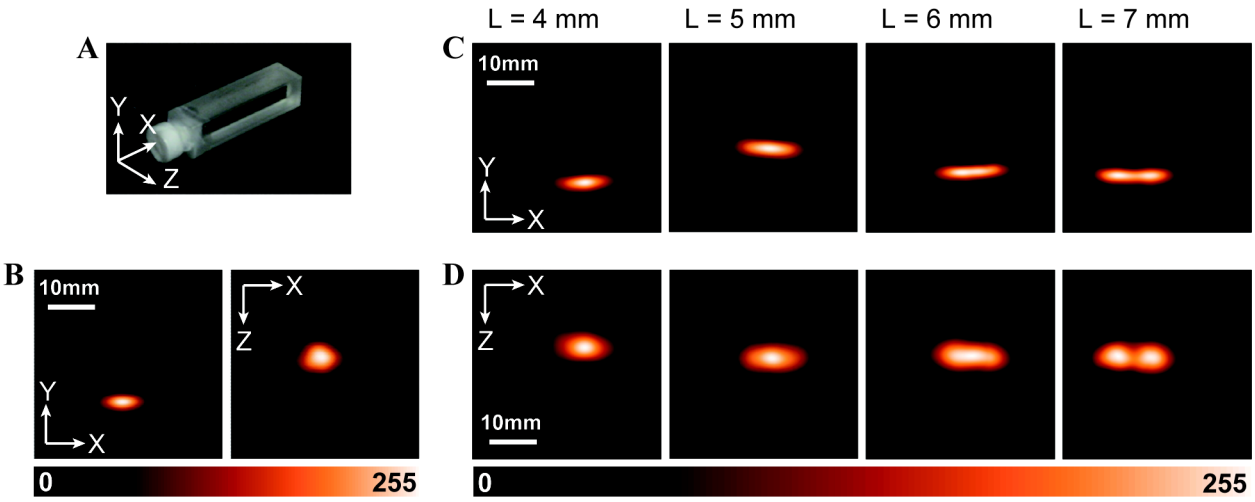


Fig. 2.8. EPR images of nitroxyl radicals measured with a surface coil array. (A) Photograph of the glass cell used as a phantom. It was filled with 1 mM TEMPOL-d_{17}-^{15}N solution. (B) 2D EPR images measured with a single surface coil. Measured 2D EPR images with the surface coil array in the XY-plane (C) and the XZ-plane (D). The distance (L) between the centers of the coils was changed. The surface coil array was placed on the glass cell filled with a solution of 1 mM TEMPOL-d_{17}-^{15}N.

2.4. Discussion

The experimental results showed that the surface coil array could extend the area of visualization in CW-EPR imaging. The area of visualization with the surface coil array was extended approximately 2-fold in comparison to that of a conventional surface coil. In this experimental results, a drop in the signal intensity of the EPR image in Figs. 2.8C and 2.8D was observed when the distance between the centers of two coils was 7 mm. This is because the intensity of RF magnetic field decreased in the outside of a surface coil. Although there was another coil in the array coil system, that coil could not compensate the decrease of the sensitivity of EPR detection in that region if the distance between the two coils became larger. Although the microwave characteristics of the medium surrounding the coils affects the RF magnetic field distribution, the results in Fig. 2.8 demonstrate the feasibility of the surface coil array in CW-EPR imaging.

One of the important technical issues regarding the surface coil array was decoupling of

the coils. The PIN-diode switches in the resonators could suppress the mutual coupling of the coils. However, the resonance frequency was slightly shifted when the PIN-diode switch was turned on, because the mutual coupling of coils could not be removed completely. Decoupling techniques of coil arrays have previously been investigated in MRI [2.36,2.37], and although modern MRI methods are based on a pulsed protocol, knowledge of decoupling techniques regarding coil arrays can also be applied in CW-EPR imaging. This may become increasingly relevant for future work, where decoupling techniques for an increased number of coils will be a key technical challenge.

A shift in the resonance frequency of more than 200 MHz was observed when using the surface coil array developed in this study with the PIN-diode switch was on. Since this shift in the frequency was enough to decouple the coils, the dual-peak resonance, disappeared, as illustrated in Figs. 2.6A and 2.6B. Similarly, Yokoyama investigated the twin-loop resonator system at 245 MHz [2.38]. While dual-peak resonance appeared in the two-loop resonator system, it was suppressed with a combination of a phase shifter and a power combiner. Two coils were excited together in the twin resonator system.

When the area of visualization is extended, the signal-to-noise ratios of the reconstructed images were not sacrificed regardless of the position of the surface coils. This is because the data acquisition of EPR spectra under magnetic field gradients was performed with each coil sequentially, and the effect of mutual coupling between the two coils was suppressed by shifting the resonance frequency of the resonator, which was not fed. Thus, the signal-to-noise ratios of the obtained images depend on the sensitivity of each resonator. In this experimental setup, the efficiency of generating RF magnetic field of each resonator was similar to that of a conventional (individual) surface coil resonator, and thereby the array coil system does not affect the signal-to-noise ratios of the resultant EPR images.

In future work, the following technical issues regarding the use of the surface coil array

in CW-EPR imaging will need to be addressed: (i) The variation of the resonance frequencies of individual resonators should be less that several MHz. This was constrained with the characteristics of ATC. In the preliminary experiments, the author could not perform measurements when the difference in resonator frequencies was greater than 5 MHz, because each resonator could not be tuned to the microwave carrier frequency. (ii) Bulky shielding cases should be re-designed to accommodate a set of tuning and matching circuits for a number of surface coils.

2.5. Conclusions

The author demonstrated the feasibility of using a surface coil array in CW-EPR imaging. The prototype showed good suppression of the mutual coupling of the coils in CW-ERP detection. The results in this chapter highlight fundamental characteristics of the surface coil array in CW-EPR imaging, in particular the increased region of visualization that is attainable when compared to conventional surface coils, which may be particularly beneficial for the imaging of free radical distribution in small animals.

References

[2.1] H. M. Swartz, L. J. Berliner, Introduction to in vivo EPR, in: L. J. Berliner (Ed.), Biological Magnetic Resonance Vol. 18, Kluwer Academic/Prenum Publishers, New York, 2003, pp. 1–20.

[2.2] S. Cuzzocrea, D. P. Riley, A. P. Caputi, D. Salvemini, Antioxidant therapy: A new pharmacological approach in shock, inflammation, and ischemia/reperfusion injury, Pharmacol. Rev. 53 (2001) 135–159.

[2.3] J. L. Zweier, M. A. H. Talukder, The role of oxidants and free radicals in reperfusion injury, Cardiovasc. Res. 70 (2006) 181–190.

[2.4] W. Froncisz, J. S. Hyde, The loop-gap resonator: a new microwave lumped circuit ESR sample structure, J. Magn. Reson. 47 (1982) 515–521.

[2.5] H. J. Halpern, D. P. Spencer, J. van Polen, M. K. Bowman, A. C. Nelson, E. M. Dowey, B. A. Teicher, Imaging radio-frequency electron-spin-resonance spectrometer with high-resolution and sensitivity for in vivo measurements, Rev. Sci. Instrum, 60 (1989) 1040–1050.

[2.6] P. Kuppusamy, M. Chzhan, K. Vij, M. Shteynbuk, D. J. Lefer, E. Giannella, J. L. Zweier, Three-dimensional spectral spatial EPR imaging of free-radicals in the heart – A technique for imaging tissue metabolism and oxygenation, Proc. Natl. Acad. Sci. U.S.A. 91 (1994) 3388–2292.

[2.7] M. Afeworki, G. M. van Dam, N. Devasahayam, R. Murugesan, J. Cook, D. Coffin, J. H. A.-Larsen, J.B. Mitchell, S. Subramanian, M.C. Krishna, Three-dimensional whole body imaging of spin probes in mice by time-domain radiofrequency electron paramagnetic resonance, Magn. Reson. Med. 43 (2000) 375–382.

[2.8] J. A. Brivati, A. D. Stevens, M. C. R. Symons, A radiofrequency ESR spectrometer for in vivo imaging, J. Magn. Reson. 92 (1991) 480–489.

[2.9] S. Ishida, S. Matsumoto, H. Yokoyama, N. Mori, H. Kumashiro, N. Tsuchihashi, T. Ogata, M. Yamada, M. Ono, T. Kitajima, H. Kamada, E. Yoshida, An ESR-CT imaging of the head of a living rat receiving an administration of a nitroxide radical, Magn. Reson. Imaging 10 (1992) 109–114.

[2.10] G. He, S. P. Evalappan, H. Hirata, Y. Deng, S. Petryakov, P. Kuppusamy, J.L. Zweier, Mapping of the B_1 field distribution of a surface coil resonator using EPR imaging. Magn. Reson. Med. 48 (2002) 1057–1062.

[2.11] S. Petryakov, M. Chzhan, A. Samouilov, G. He, P. Kuppusamy, J. L. Zweier, A bridged loop-gap S-band surface resonator for topical EPR spectroscopy, J. Magn. Reson. 151 (2001) 124–128.

[2.12] A. D. Stevens, A moderately sized resonator/surface coil for radiofrequency electron paramagnetic resonance spectroscopy and imaging in vivo, Br. J. Radiol. 67 (1994) 1243–1248.

[2.13] B. B. Williams, H. J. Halpern, In vivo EPR imaging, in: S.S. Eaton, G.R. Eaton, L. J. Berliner (Eds.), Biological Magnetic Resonance Vol. 23, Kluwer Academic/Prenum Publishers, New York, 2005, pp. 283–319.

[2.14] G. R. Eaton, S. S. Eaton, EPR spectrometers at frequencies below X-band, in: C. J. Bender and L.J. Berliner (Eds.), Biological Magnetic Resonance Vol. 21, Kluwer Academic/Prenum Publishers, New York, 2004, pp. 59–114.

[2.15] G. A. Rinard, R. W. Quine, S. S. Eaton, G. R. Eaton, Frequency dependence of EPR sensitivity, in: C. J. Bender and L. J. Berliner (Eds.), Biological Magnetic Resonance Vol. 21, Kluwer Academic/Prenum Publishers, New York, 2004, pp. 115–154.

[2.16] S. Petryakov, A. Samouilov, M. Chzhan-Roytenberg, E. Kesselring, Z. Q. Sun, J. L. Zweier, Segmented surface coil resonator for in vivo EPR applications at 1.1 GHz, J. Magn. Reson. 198 (2008) 8–14.

[2.17] P. B. Roemer, W. A. Edelstein, C. E. Hayes, S. P. Souza, O. M. Mueller, The NMR phased array, Magn. Reson. Med. 16 (1990) 192–225.

[2.18] W. E. Kwok, J. Zhong, Z. You, G. Seo, S. M. S. Totterman, A four-element phased array coil for high resolution and parallel MR imaging of the knee, Magn. Reson. Imaging 21 (2003) 961–967.

[2.19] K. V. Mogatadakala, J. A. Bankson, P. A. Narayana, Three-element phased-array coil for imaging of rat spinal cord at 7T, Magn. Reson. Med. 60 (2008) 1498–1505.

[2.20] G. J. L. A. Nijeholt, M. A. A. van Walderveen, J. A. Castelijns, J. H. T. M. van Waesberghe, C. Polman, P. Scheltens, P.F.W.M. Rosier, P.J.H. Jongen, F. Barkhof, Brain and spinal cord abnormalities in multiple sclerosis – Correlation between MRI parameters, clinical subtypes and symptoms, Brain 121 (1998) 687–697.

[2.21] C. von Morze, J. Tropp, S. Banerjee, D. Xu, K. Karpodinis, L. Carvajal, C. P. Hess, P. Mukherjee, S. Majumdar, D.B. Vigneron, An eight-channel, nonoverlapping phased array coil with capacitive decoupling for parallel MRI at 3 T, Concept. Magn. Reson. B Magn. Reson. Eng. 31B (2007) 37–43.

[2.22] G. A. Rinard, R. W. Quine, S. S. Eaton, G. R. Eaton, Microwave coupling structues for spectroscopy, J. Magn. Reson. Ser. A 105 (1993) 137–144.

[2.23] H. Hirata, G. He, Y. Deng, I. Salikhov, S. Petryakov, J. L. Zweier, A loop resonator for slice-selective in vivo EPR imaging in rats, J. Magn. Reson. 190 (2008) 124–134.

[2.24] H. Hirata, T. Walczak, H. M. Swartz, Electronically tunable surface-coil-type resonator for L-band EPR spectroscopy, J. Magn. Reson. 142 (2000) 159–167.

[2.25] S. McCallum, F. Resmer, Automatic coupling control system for radio frequency in vivo electron paramagnetic resonance based on a piezoelectric controlled capacitor, Rev. Sci. Instrum. 70 (1999) 4706–4710.

[2.26] M. Chzhan, P. Kuppusamy, J. L. Zweier, Development of an electronically tunable L-band resonator for EPR spectroscopy and imaging of biological samples, J. Magn. Reson. Ser. B 108 (1995) 67–72.

[2.27] G. He, S. Petryakov, A. Samoulilov, M. Chzhan, P. Kuppusamy, J. L. Zweier, Development of a resonator with automatic tuning and coupling capability to minimize sample motion noise for 0 EPR spectroscopy, J. Magn. Reson. 149 (2001) 218–227.

[2.28] H. Hirata, Z.-W. Luo, Stability analysis and design of automatic frequency control system for in vivo EPR spectroscopy, Magn. Reson. Med. 46 (2001) 1209–1215; Erratum 49 (2003) 977.

[2.29] H. Sato-Akaba, H. Fujii, H. Hirata, Improvement of temporal resolution for three-dimensional continuous-wave electron paramagnetic resonance imaging, Rev. Sci. Instrum. 79 (2008) 123701.

[2.30] H. Sato-Akaba, Y. Kuwahara, H. Fujii, H. Hirata, Half-life mapping of nitroxyl radicals with three-dimensional electron paramagnetic resonance imaging at an interval of 3.6 seconds, Anal. Chem. 81 (2009) 7501–7506.

[2.31] Z.-P. Liang, P. C. Lauterbur, Principles of Magnetic Resonance Imaging: A Signal Processing Perspective, IEEE Press, Piscataway, NJ, 2000, pp. 207–209.

[2.32] http://rsbweb.nih.gov/ij/

[2.33] C. Bowick, RF Circuit Design, Newnes, Boston, MA, 1982, pp. 37–43.

[2.34] T. Ogata, Y. Ishikawa, M. Ono, L.J. Berliner, Visualization of eddy-current losses in L-Band ESR imaging, J. Magn. Reson. 97 (1992) 616–622.

[2.35] M. Sueki, G. A. Rinard, S. S. Eaton, G. R. Eaton, Effect of eddy currents on EPR spectra, J. Magn. Reson. Ser. A 103 (1993) 208–216.

[2.36] B. Wu, X. L. Zhang, P. Qu, G. X. Shen, Design of an inductively decoupled

microstrip array at 9.4 T, J. Magn. Reson. 182 (2006) 126–132.

[2.37] R. F. Lee, R.O. Giaquinto, C.J. Hardy, Coupling and decoupling theory and its application to the MRI phased array, Magn. Reson. Med. 48 (2002) 203–213.

[2.38] H. Yokoyama, Twin LC resonator system for EPR measurements operating at radio-frequency, Appl. Magn. Reson. 38 (2010) 501–509.

Chapter 3

Four-channel surface coil array for sequential CW-EPR image acquisition

3.1. Introduction

In vivo electron paramagnetic resonance (EPR) imaging is an important technique for visualizing the distribution of free radicals in animals noninvasively [3.1,3.2]. Volume coil and surface coil resonators have been used for *in vivo* EPR imaging [3.3–3.9]. However, the dimensions of both types of resonators are limited, since the circumference of the coil should be small enough in comparison to the wavelength of RF electromagnetic waves to generate homogeneous magnetic fields. Electromagnetic waves in the frequencies from 250 MHz to 1.2 GHz have been mainly used for *in vivo* small animal EPR imaging [3.10,3.11]. This is because sufficient penetration of RF magnetic fields in biological tissues is required, and tissue heating due to absorption of electromagnetic waves should be decreased [3.12]. In this frequency band, an increase of the visualization area is an important technical challenge in small animal EPR imaging, and should enhance the applicability of surface coils to animal imaging. However, it is difficult to visualize a broader region using conventional surface coils. To overcome the limitation of the coil dimensions, Petryakov *et al*. developed a larger surface coil resonator that operated at 1.1 GHz using four loop segments [3.13]. Petryakov *et al*. also reported a single-loop multi-gap resonator for whole-body mouse at 1.2 GHz [3.14]. However, these resonators were intended to make possible a single loop with a larger diameter. A surface coil array with multiple small surface coils has three advantages: i.e., (i) potentially higher signal-to-noise ratio for the surface region of the subject, (ii) better homogeneity of the signal intensity over a broader region of the subject surface, and (iii) ease of extension of the field-of-view with additional coils. Since a large single loop cannot provide a homogeneous signal intensity over a broader region of the subject surface, a surface

coil array is a suitable approach for measuring the broader region near the subject surface, e.g., skin of a subject animal. In contrast to EPR imaging, phased array coils have been often used in proton magnetic resonance imaging (MRI) [3.15–3.17] and have been used to visualize broader regions of the human body in a clinical setting, i.e., spine, brain, and heart [3.18–3.20]. There have been many reports on the use of phased array coils in MRI and methods for decoupling between neighboring coils [3.21,3.22]. However, these methods are not necessarily applicable to CW-EPR imaging, since the signal detection protocol in CW-EPR imaging is different from that in time-domain MRI.

Recent MRI systems frequently use a large coil as a transmitter coil and multiple small coils as receiver coils. In this case, the technique for array coils in MRI is difficult to apply to CW-EPR imaging, since low-field CW-EPR spectrometers operate in the reflection-mode that detects the reflected electromagnetic waves from a resonator as EPR signals. However, Hyde and colleagues reported a technique of switching coils in MRI [3.23]. This technique used multiple coils and one receiver, and the image data were sequentially acquired by switching coils. It can be applied to CW-EPR imaging because multiple receivers and a transmitter/receiver switch are not needed to detect EPR signals. However, it is difficult to set all of the coils to exactly the same resonance frequency in CW-EPR due to mutual coupling between the coils. Therefore, some modifications are required to apply the technique of switching coils to CW-EPR imaging. Specific technologies are needed to build a surface coil array in CW-EPR imaging. The author previously reported proof-of-concept experiments for a 2-channel surface coil array in CW-EPR imaging in Chapter 2 [3.24]. To suppress the mutual inductive coupling between coils, the resonance frequency of one of the surface coil resonators was shifted with a PIN diode switch. In Chapter 2, the author was able to increase the area of visualization in EPR imaging. However, the 2-channel surface coil array was operated manually to achieve sequential data acquisition. A 4-channel surface coil array was

also tested in pulsed EPR imaging with manually operated coil-selection [3.25]. Due to manual operation of the surface coil array, it was difficult to visualize free radicals in sequential image acquisition with a limited time. In animal experiments, since the lifetimes of EPR imaging agents are often limited, electronic control circuits and control software, instead of manual operation, will be necessary for operation of a multiple-channel coil array and EPR data acquisition.

In this chapter, the author focuses on a 4-channel surface coil array and the control circuits for CW-EPR imaging to achieve sequential data acquisition. The combination of the coil array and control circuits is important for automatic sequential data acquisition in EPR imaging. The author also describes EPR images measured with the 4-channel surface coil array using a phantom and a living mouse. In this study, the author achieved the *in vivo* CW-EPR imaging of a mouse with a four-channel surface coil array and nitroxyl radical imaging agents that have a modest lifetime. To date, only EPR images of mice using trityl-based radicals, which have a longer lifetime, have been reported in EPR studies with a surface coil array [3.25]. The author demonstrated for the first time small animal imaging with a four-channel surface coil array and relevant control circuits with the use of nitroxyl radical imaging agents.

3.2. Experimental

3.2.1. Configuration of the surface coil array and control circuit

Figure 3.1 illustrates the setup of the EPR imager and the 4-channel surface coil array used in this experiments. The details of the laboratory-built 750-MHz CW-EPR imager have been reported elsewhere [3.26]. The surface coil array was formed with four surface coil resonators and operated with three kinds of switches. An RF coaxial switch (87104B, Agilent Technologies, Santa Clara, CA), a PIN diode switch, and a signal selection switch of an auto

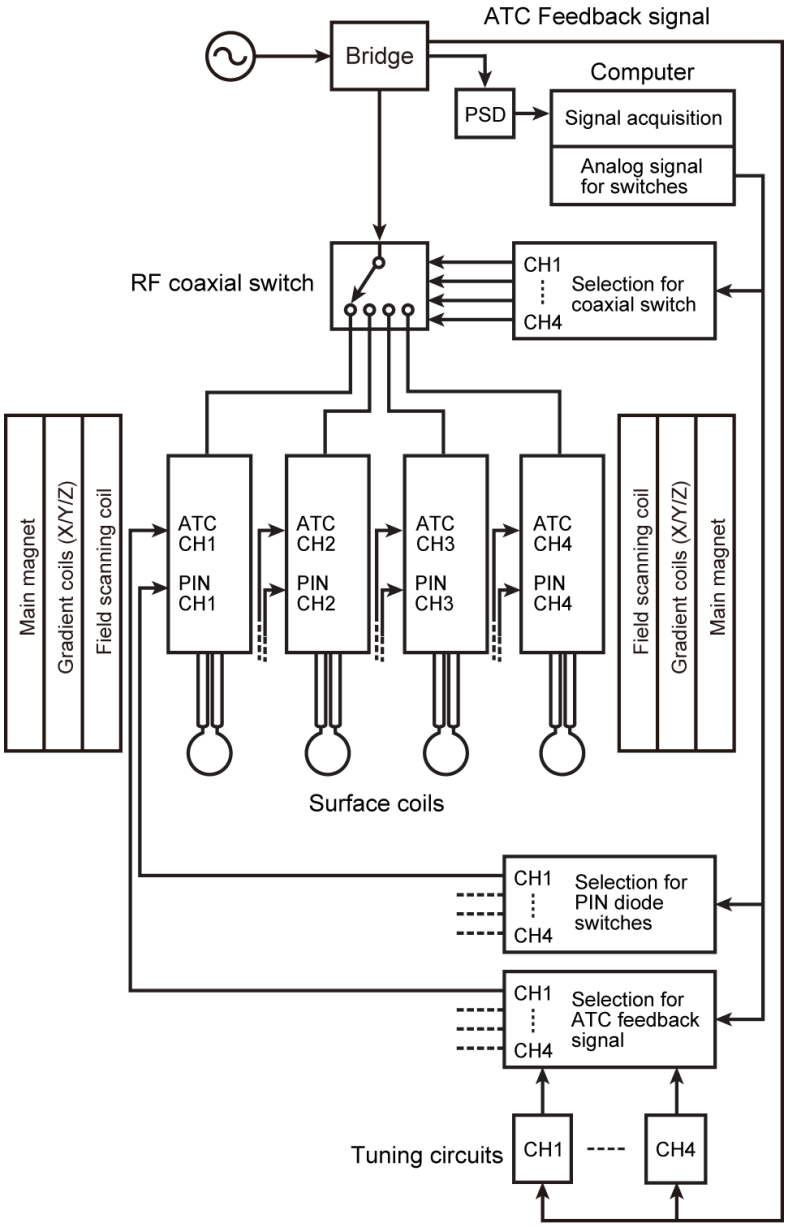


Fig. 3.1. Schematic diagram of the 4-channel surface coil array and the CW-EPR spectrometer with coil-selection circuits. The coil-selection circuits were driven by an analog signal from the computer. PSD = phase-sensitive detection by a lock-in amplifier. Magnetic field modulation coils are not depicted in this diagram.

tuning control (ATC) feedback loop were controlled by an analog signal from a computer. In CW-EPR imaging using the surface coil array, EPR data acquisition was performed sequentially for each resonator. During the measurement with the first resonator, RF waves were not fed to the three other resonators. When one resonator was driven for EPR data

acquisition, the resonance frequencies of the other resonators were shifted with the PIN diode switch to suppress inductive coupling with the driven resonator. After data acquisition with the first resonator, the switches were changed, and the second and subsequent measurements were performed with each resonator as with the first resonator. The switching rates of PIN diodes and an RF coaxial switch were 1.55 μs and 15 ms, respectively. The time constant of an RC-filter connected to PIN diodes was 0.48 ms. Thus, the resultant switching rate was limited by the rate of the RF coaxial switch (15 ms). Switches were changed after the acquisition of a set of whole projection data with a single coil. After EPR spectra were acquired with the four resonators sequentially, images of the subject were individually reconstructed and combined to obtain the final image using MATLAB-based software (MathWorks, Natick, MA).

3.2.2. Surface coil resonator

Figure 3.2 shows the configuration of an individual surface coil resonator used for the surface coil array. The resonator has an LC-resonant circuit, a parallel transmission line, varactors (1SV217, Toshiba, Tokyo, Japan) for frequency adjustment, varactors (1SV245, Toshiba, Tokyo, Japan) for impedance matching adjustment, and a PIN diode switch for controlling the resonance frequency [3.24]. The surface coils were made from copper-laminated substrate (18 μm of copper, NPC-H220A, Nippon Pillar Packing Corp., Osaka, Japan), and the FR-4 equivalent substrate (34R, Sunhayato, Tokyo, Japan) was used for a surface-mounted circuit board for impedance matching, frequency tuning, and the PIN diode switch. The surface coils were square and all corners were chamfered to prevent the unwanted radiation of RF waves.

Since the author focused on measurements of the back of a subject mouse, the planar design of the surface coil array was appropriate for that purpose. In addition, the magnet the author used produced a homogeneous magnetic field over a spherical volume with a diameter of 30 mm. Thus, the surface coil array was set to cover a length of approximately 30 mm. As shown in Fig. 3.3A, the coils had an inner size of 8 × 8 mm and the copper lines were 1.6 mm wide. The coils were overlapped to minimize inductive coupling with neighboring coils. In addition, two dummy coils were placed on both ends of the coil array to make each coil symmetrical, which reduced the variance of the resonance frequencies of the resonators. To electrically insulate the coils from each other, polytetrafluoroethylene (PTFE) sheets (0.1mm-thick) were inserted into the overlapping regions. The resonance frequencies of the resonators were adjusted to the RF carrier frequency with the tuning circuit; the author calls this feedback system ATC instead of automatic frequency control (AFC). The adjustable

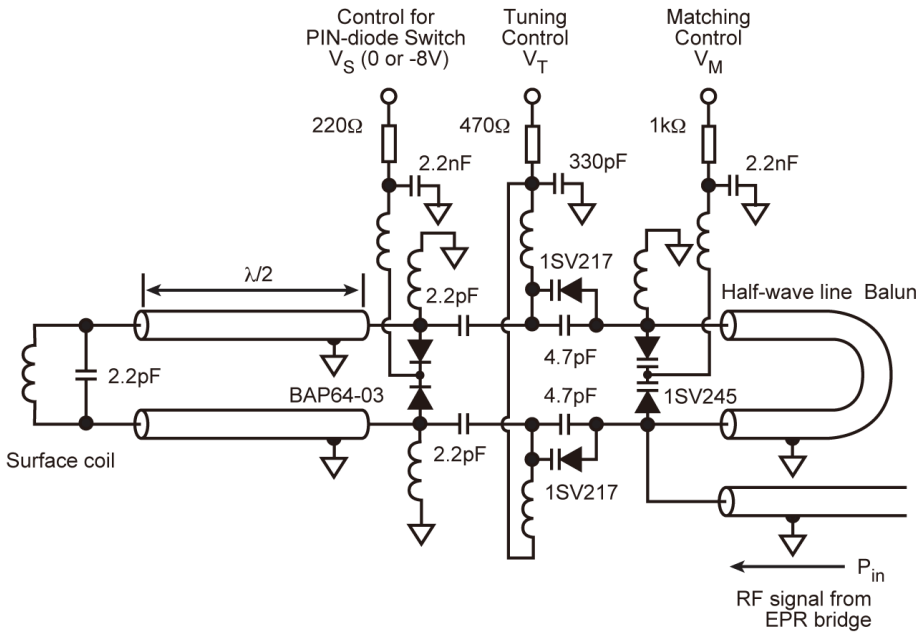


Fig. 3.2. Diagram of an individual surface coil resonator. A PIN diode switch was formed with two PIN diodes connected in series. When a negative voltage (-8V) was applied to the PIN diode switch, the impedance of the PIN diodes became low. The resonance frequency of the resonator was then shifted approximately 250 MHz, and inductive coupling between the coils was suppressed.

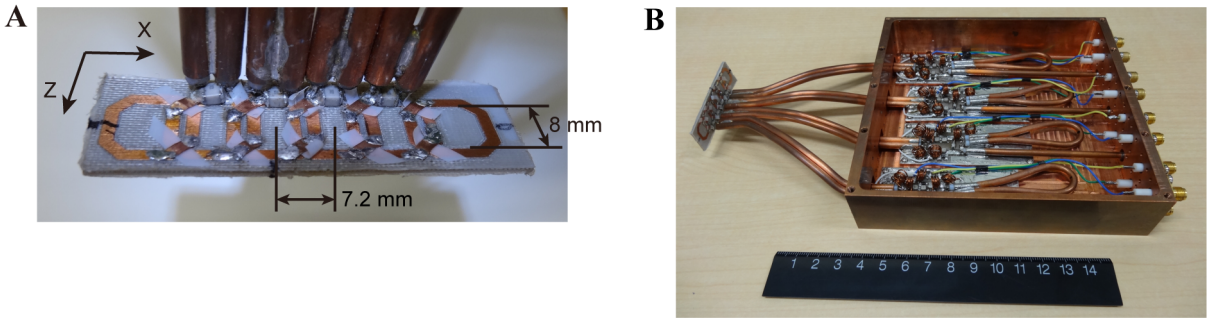


Fig. 3.3. Developed surface coil array. (A) Photographs of the surface coils. The distance between the centers of neighboring coils was 7.2 mm, and the inner distance of the printed coils was 8.0 mm. (B) The whole structure of the surface coil array. Both ends of the coils in Fig. 3.3A were dummy coils and placed to decrease the difference in the resonance frequencies of individual resonators.

range of the resonance frequency of the resonator was approximately 8 MHz. Two PIN diodes (BAP64-03, Royal Philips Electronics, Netherlands) were used as a switch to shift the resonance frequency of the resonator to suppress inductive coupling between the coils. The PIN diodes were placed between the coaxial lines. When the forward-bias voltage was applied to the PIN diodes, the resistance of the PIN diodes became low, and the end of the transmission line was shorted. The resonance frequency of the resonator was therefore shifted enough to suppress inductive coupling between neighboring coils. The parallel transmission line and the half-wave line balun were made from 50-ohm non-magnetic semi-rigid coaxial cables (3.6 mm in diameter, SX-36-Cu, Sanken Corp., Tokyo, Japan).

Figure 3.3B shows an overview of the surface coil array. Each coil was connected to the end of the transmission line. The PIN diode switches, frequency tuning and impedance matching circuits were shielded by a copper box (4 mm-thick) to prevent interference with magnetic field modulation. The entire length of the resonators including the shielding box was 230 mm. The transmission lines were bent to conform to the distance between the surface coils and the coupling circuits.

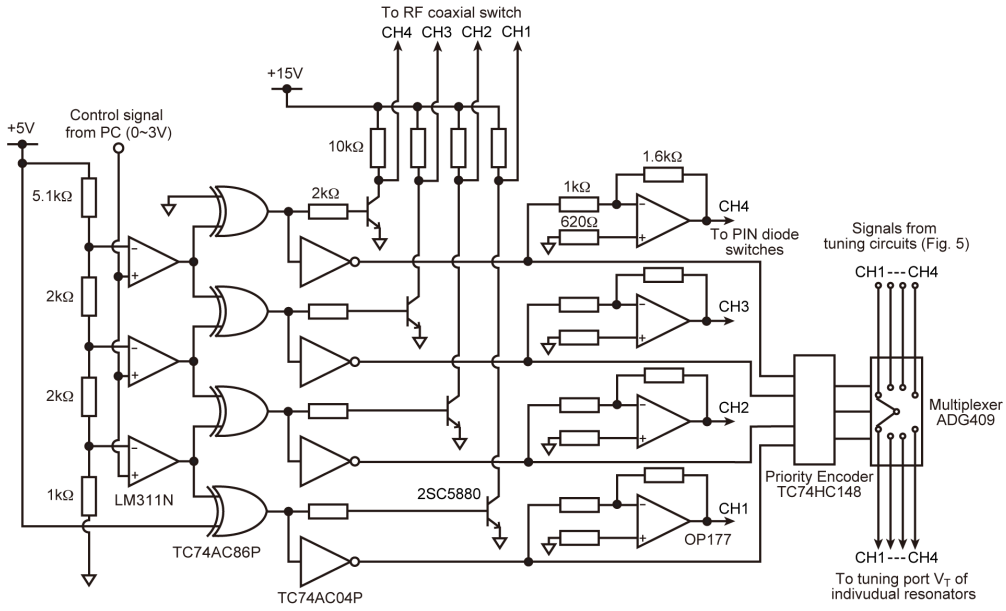


Fig. 3.4. Circuit diagram of the coil-selection circuits. When an analog signal (0, 1, 2, and 3 V) from the computer was applied to the coil-selection circuit, logic gates and transistors selected the individual surface coil resonator to be excited.

3.2.3. Coil-selection circuits

Coil-selection circuits were built to systematically operate the three switches. Figure 3.4 shows a diagram of the coil-selection circuits. An analog voltage signal from a computer drove the coil-selection circuits. Analog voltage signals (0, 1, 2 and 3 V) from the computer corresponded to each coil. The computer was controlled by LabVIEW-based software (National Instruments, Austin, TX). When the voltage signals from the computer were applied to the comparators (LM311N, STMicroelectronics, Geneva, Switzerland), exclusive-OR (XOR) logic gates (TC74AC86P, Toshiba, Tokyo, Japan) output digital signals of either 0 or 5 V, depending on the voltage signal from the computer. The following circuits were driven using these digital signals generated from the analog voltage signal. The circuit for the RF coaxial switch consisted of four NPN transistors (2SC5880, Rohm Co., Kyoto, Japan). When the digital signals from the XOR logic gates were transferred to the selection circuit for the RF coaxial switch, one transistor was driven with a voltage of 5 V from the

XOR logic gate. The terminal of the corresponding channel of the RF coaxial switch was then grounded to connect the feed line to the resonator to be excited. The digital signals from the XOR logic gates were changed to their opposite logic-level by inverters (TC74AC04P, Toshiba, Tokyo, Japan). The inverted digital signals were transferred to the selection circuit for the PIN diode switches and the selection switch of the ATC feedback signal. The selection circuit for the PIN diode switches consisted of four inverting amplifiers, since the PIN diode switches required negative voltage (-8 V) to be turned on. The selection circuit for the ATC feedback signal consisted of a priority encoder (TC74HC148, Toshiba, Tokyo, Japan) and a multiplexer (ADG409, Analog Devices, Cambridge, MA).

Since the adjustable frequency range of the ATC system was limited and the four resonators had slightly different resonance frequencies, adjustable frequency tuning circuits for individual channels of the resonators were required. This additional frequency tuning circuit, as shown in Fig. 3.5, can change the resonance frequency of the resonator by approximately 5 MHz. Four identical circuits were made and used for each resonator in the surface coil array.

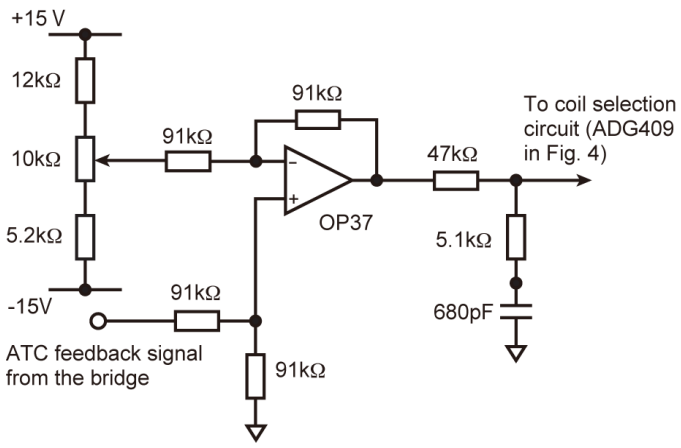


Fig. 3.5. Circuit diagram of the frequency adjustment circuit for the ATC feedback signal. The resonance frequency of the individual resonator was adjusted with the output voltage from this circuit in addition to the ATC feedback control system.

3.2.4. Phantom imaging

To investigate the area of visualization with the surface coil array, the author measured three-dimensional (3D) EPR images of a glass cell (10 × 20 × 45 mm) filled with 9 mL of a solution of 1 mM 3-carbamoyl-2,2,5,5-tetramethylpyrrolidine-1-oxyl (3-CP) (purchased from Wako Pure Chemical Industries, Ltd., Osaka, Japan) that was prepared in distilled water. An EPR absorption peak at a lower field of three absorption peaks of 3-CP was measured for image scanning of the phantom. To simplify sequential measurements, frequency tuning and impedance matching of the individual resonators were adjusted in advance. The field-of-view (FOV) was set to 52 mm. The parameters for EPR imaging were as follows: scanning field 5.0 mT, magnetic field gradient 100 mT/m, magnetic field modulation 0.2 mT, modulation frequency 90 kHz, field scanning period 0.5 s, time constant of the lock-in amplifier 0.3 ms, applied RF power 4 mW, number of projections 126, with three averages, giving a total image acquisition time of 16 min. To obtain less noisy images in 3D phantom imaging, the author accumulated all projection data 3 times. One-step 3D filtered-back projection was used in image reconstruction for individual surface coils [3.27]. The signal intensity S_{combined} in the combined image was obtained as the square root of the sum of the squares of the intensities S_i in the individual images:

$$S_{\text{combined}} = \sqrt{S_1^2 + S_2^2 + S_3^2 + S_4^2} \qquad (3.1)$$

where the subscript *i* denotes individual coils. The square root of the sum of squares is an image-combination technique used with a phased array coil in MRI [3.15]. This image-combination technique is easy to apply because it does not require a magnetic field distribution map or exact knowledge of the position of the coils, which is difficult to obtain in this surface coil array. Therefore, the square root of the sum of squares method is appropriate for combining the images in this study. Surface-rendered images were drawn using IDL 7.1 data visualization software (ITT Visual Information Solution, Boulder, CO). The level of the

isosurface was set at half of the maximum intensity in each image [3.26].

3.2.5. In vivo EPR imaging

Three-dimensional EPR imaging was performed with male C3H HeJ mice that were 7 weeks old and weighed 22 g. A subject mouse was anesthetized using isoflurane (1-2% maintain) and intraperitoneally administered 300 μL of 300 mM 3-CP that was prepared in physiological saline solution. A subject mouse was placed on a bed in a prone position and covered by a PTFE plate (0.5 mm-thick) to suppress the noise derived from motion of the animal. Image scanning was started after the EPR signal amplitude reached a plateau. The protocol for all animal experiments was approved by the Hokkaido University Animal Care and Use Committee. The parameters for EPR imaging were as follows: scanning field 5.0 mT, magnetic field gradient 60 mT/m, magnetic field modulation 0.2 mT, modulation frequency 90 kHz, field scanning period 0.5 s, time constant of lock-in amplifier 0.3 ms, applied RF power 4 mW, and number of projections 126. The total image acquisition time was 5 min. In contrast to phantom imaging, in *in vivo* experiments the author had to measure all projection data before 3-CP in the mouse body was metabolized. Thus, the image acquisition time was 5 minutes in *in vivo* 3D imaging. The FOV was changed from 83.3 mm to 50 mm after image reconstruction. Surface-rendered images of a subject mouse were drawn the same as in phantom imaging.

3.2.6. Proton NMR imaging

The author used a 7-T proton MRI scanner (Unity/INOVA 300/183, Varian, Palo Alto, CA) to obtain an anatomical map of the subject mouse, which was another male C3H HeJ mouse (7 weeks old, weight 22 g). The mouse was anesthetized using isoflurane (1-2% maintain) during NMR image scanning. In this image acquisition, a spin-echo multi-slice

T_2-weighted sequence was used. The FOV was set to 50 × 50 mm. Parameters for proton NMR imaging were as follows: repetition time 3.5 s, echo time 80 ms, matrix 256 × 256, number of excitations 3, and slice thickness 0.5 mm, with a total acquisition time of approximately 45 min.

3.2.7. Image coregistration

EPR/NMR image coregistration was performed to clarify the area of visualization with the surface coil array. An EPR slice-selective image in the XY-plane (sagittal plane) was obtained from the center of the combined 3D image measured from the subject mouse. To clarify the region of surface-rendered 3D images, the threshold of 50% of the maximum intensity was applied to the slice-selective EPR image. This is the same as in surface-rendered images in 3D visualization. Before EPR/NMR image coregistration, the author performed preliminary image scans to confirm the centers of the FOVs for EPR and NMR images. Scanned mice were placed at the same location of the mouse-bed by visual inspection. The FOV of the slice-selective EPR image generated from the 3D EPR image was adjusted to that of the NMR image, and the EPR image was overlaid on the NMR image.

3.2.8. Simulation of the penetration of RF magnetic fields

To investigate the penetration depth, the magnetic field distributions in air and muscle were numerically computed using an electromagnetic field simulator (HFSS, ANSYS Inc., Canonsburg, PA). In the simulation, the author used a single coil, which was the same as a coil of the surface coil array that the author developed, and the dielectric constant and conductivity of muscle were obtained from the literature [3.28]. In the numerical model, the author neglected skin and fat layers near the surface of mice, since the author was seeking to clarify the approximate distribution of RF magnetic fields in biological tissue. The square of

the magnetic field intensity and its fitted exponential function were obtained from the magnetic field distribution along the depth direction from the center of the coil. This is because the EPR signal intensity (filling factor) is proportional to the square of the magnetic field intensity. Using the fitted curve, the author calculated the rate of the decrease in magnetic fields as a function of the distance from the center of the coil. In addition, the author applied a low-pass filter (Hamming window) to the fitted exponential function to obtain blurred images in biological tissue (muscle), since the low-pass filter was applied when EPR images were reconstructed. The cutoff frequency of the low-pass filter was set to the same value as that used for image reconstruction.

3.3. Results

3.3.1. Resonator implementation

The developed surface coil array is shown in Fig. 3.3B. Since the lengths of the RF feeding line were different between the inner two resonators and the outer two resonators, additional coaxial lines of different lengths were connected to each resonator to make the total lengths of the feeding lines from the EPR bridge to the resonators the same. The quality factors of the individual surface coil resonators were approximately 100, as measured by a vector network analyzer (E5062A, Agilent Technologies, Santa Clara, CA). During the measurement of quality factors, the resonance frequency of each surface coil resonator was set to 776 MHz. The conversion efficiency of RF magnetic field generation for each resonator was 50 $\mu T/W^{1/2}$, as measured just below the substrate of the surface coil by the perturbing metal sphere method [3.29]. The tunable range of the resonators was approximately 5 MHz in each resonator when the tuning voltage was altered from 3 to 13 V.

3.3.2. Phantom imaging

The author measured a glass cell phantom shown in Fig. 3.6A to clarify the area of visualization of the surface coil array. The 3-CP in the glass cell is a commonly used redox-sensitive imaging agent for *in vivo* EPR imaging. Figure 3.6B shows 3D EPR images acquired with individual coils. Figure 3.6C shows the combined 3D EPR images obtained from the images in Fig. 3.6B. The area of visualization was approximately 32 mm in length (X-direction) and 7.5 mm in width (Z-direction), which is almost equal to the dimensions of the coil array. The depth of visualization (Y-direction) was approximately 4.5 mm.

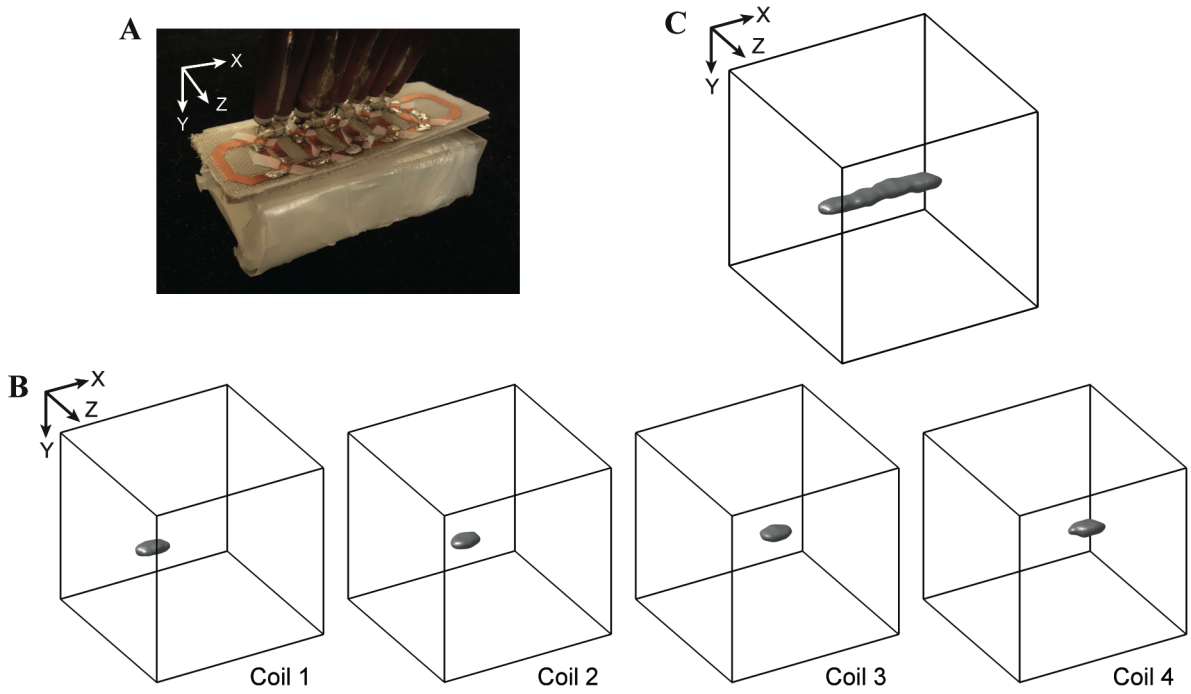


Fig. 3.6. Three-dimensional EPR images of a nitroxyl radical solution measured with the surface coil array. (A) Photograph of the glass cell phantom filled with 1 mM 3-CP solution. The surface coil array was placed on the glass cell phantom. (B) Three-dimensional EPR images measured with the individual surface coils. (C) Combined 3D EPR image. The threshold of surface rendering for all 3D images was set to 50% of the peak signal intensity.

3.3.3. Mouse imaging

Figure 3.7A shows a photograph of the subject mouse placed on the sample bed and the surface coil array. Figure 3.7B shows 3D EPR images acquired with individual coils. Figure

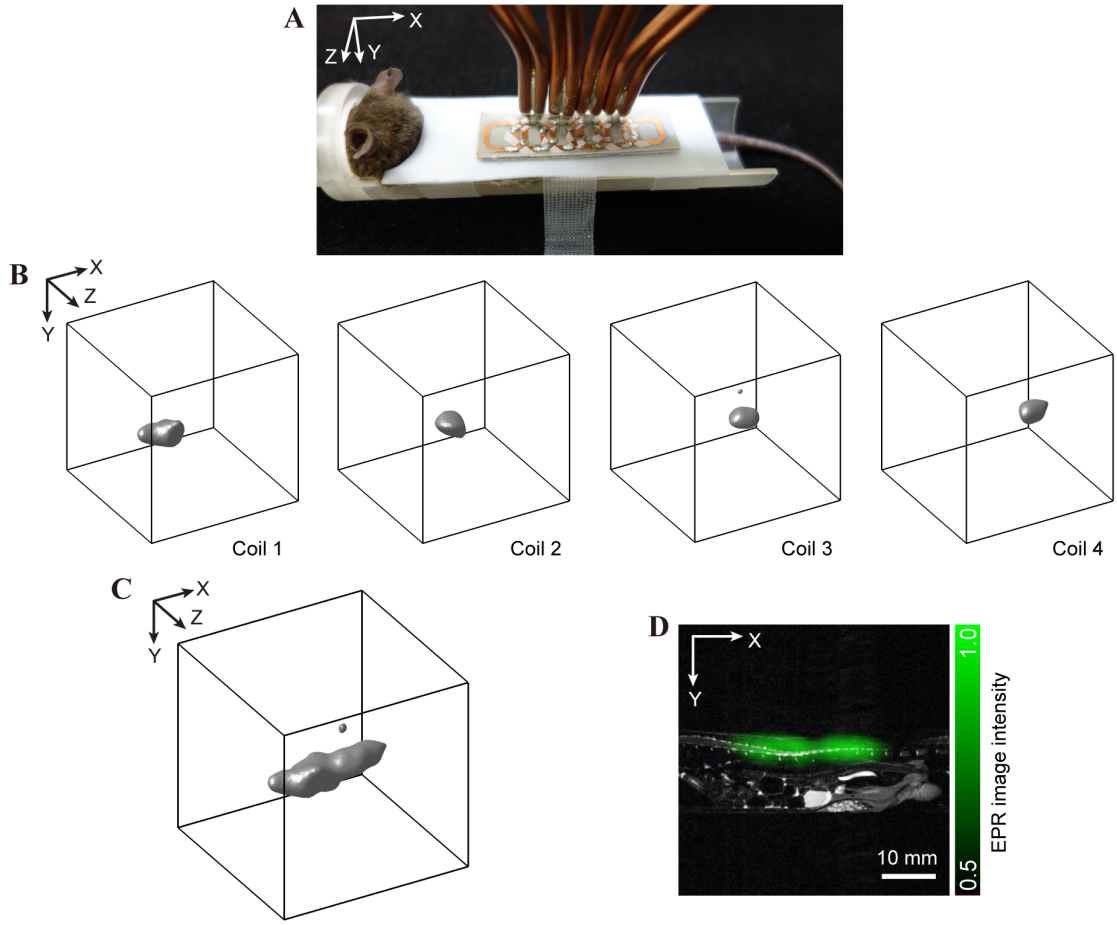


Fig. 3.7. Photograph of a subject mouse on the bed of the EPR imager and three-dimensional EPR images of the subject mouse. (A) A subject mouse was covered with a PTFE plate to suppress its motion. (B) Three-dimensional EPR images measured with individual surface coils. (C) Combined 3D EPR image of the 3-CP imaging agent. The threshold of surface rendering for 3D images was set to 50% of the peak signal intensity. (D) EPR/NMR coregistration image. The 2D EPR image was obtained from the 3D combined image in Fig. 3.7C.

3.7C shows the combined 3D EPR image generated from the images in Fig. 3.7B. Figure 3.7D shows a coregistration image of the EPR image of 3-CP and a T_2-weighted NMR image. The depth penetration in Fig. 3.7D was approximately 5.7 mm, which was deeper than the result with the phantom image. As shown in Fig. 3.7D, it was possible to visualize the distribution of 3-CP as deep as about the backbone of the mouse. When the subject mouse was placed on the high B_1 field, the intensity of noise derived from animal motion was stronger than the EPR signal intensity. Therefore, the author had to place the subject mouse at

a distance sufficient to suppress this noise effect, and the author found that a PTFE plate was appropriate for maintaining separation between the coils and the subject mouse. In addition, the author could limit unnecessary motion of the animal by covering it with the PTFE plate and fixing it to the bed using adhesive tape.

3.3.4. Simulated RF magnetic fields

Figure 3.8 shows the simulated distribution of RF magnetic fields near the surface coil in the numerical model. RF magnetic fields in air (Fig. 3.8B) and in muscle (Fig. 3.8C) were normalized to the peak magnitude of RF magnetic fields in air. The distance within which the signal intensity became half of the peak signal intensity was predicted to be 6.1 mm when the parameters of muscle were given in the bottom half space in the numerical model. The corresponding value measured in a subject mouse was 5.7 mm from the center of the coil in the depth direction (Fig. 3.7). This clearly shows that the RF magnetic fields in muscle are localized near the surface of the subject (bottom half space) in comparison to the distribution of RF magnetic fields in air.

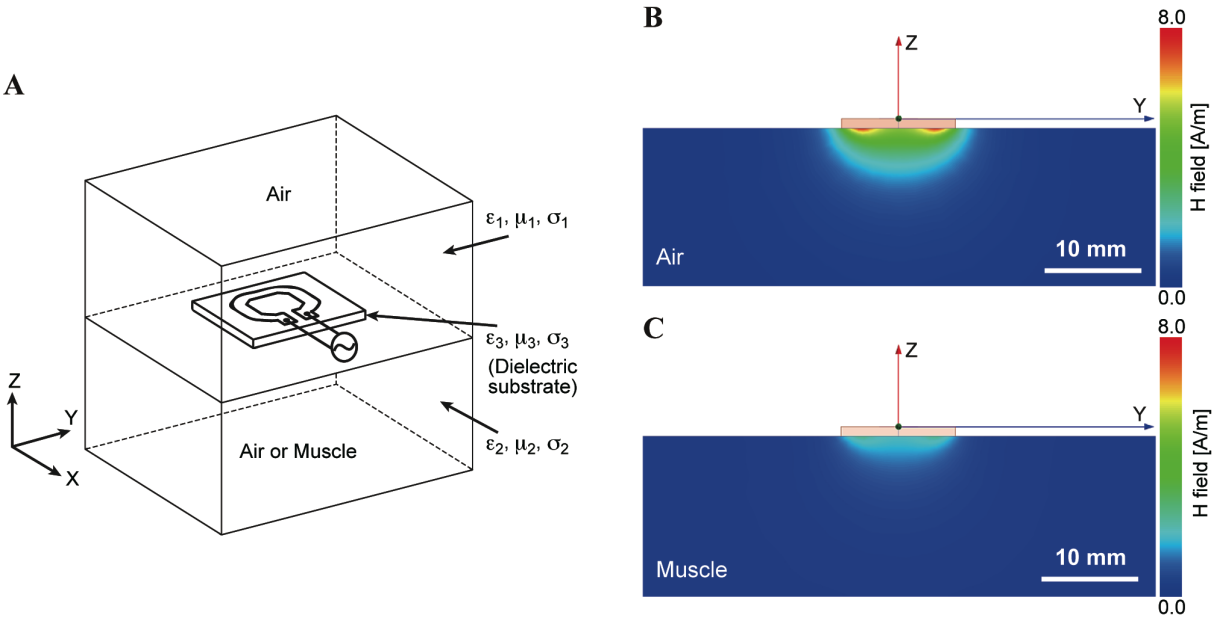


Fig. 3.8. Numerical simulation of RF magnetic fields near a surface coil. (A) Simulation of RF magnetic fields. The space of the upper half was assumed to be air (permittivity $\varepsilon_1=1.0006\varepsilon_0$ F/m, permeability $\mu_1=4\pi\times10^{-7}$ H/m, conductivity $\sigma_0=0$ S/m, permittivity of free space $\varepsilon_0=8.854\times10^{-12}$ F/m), and the space of the bottom half was assumed to be air ($\varepsilon_2=1.0006\varepsilon_0$ F/m, $\mu_2=4\pi\times10^{-7}$ H/m, $\sigma_1=0$ S/m) or muscle ($\varepsilon_2=63.8\varepsilon_0$ F/m, $\mu_2=4\pi\times10^{-7}$ H/m, $\sigma_2=1.25$ S/m). Subscripts 1, 2, and 3 designate the upper half space, the bottom half space, and the dielectric substrate, respectively. The thickness (1.0 mm) and the parameters of the dielectric substrate were also given as in the simulation model ($\varepsilon_3=2.17\varepsilon_0$ F/m, $\mu_3=4\pi\times10^{-7}$ H/m, $\sigma_3=0$ S/m). The calculated space was 200 × 200 × 200 mm, and the radiation boundary condition was used in the simulation. (B) RF magnetic field distribution in air. (C) RF magnetic field distribution in muscle. In the calculations for both RF field distributions, the applied RF power was 4 mW. An RF frequency of 775 MHz was used in the numerical simulations.

3.4. Discussion

The quality factors and generation efficiencies of the RF magnetic fields of the four surface coil resonators were similar to those of the 2-channel surface coil array the author reported in Chapter 2 [3.24] . Thus, an increase in the number of coils did not degrade the performance of the resonators. This also suggests that a multiple-channel surface coil array of more than 4 channels may be possible for CW-EPR imaging.

Since the surface coil array was operated sequentially with control circuits, it can be applied to existing CW-EPR imagers. Moreover, the area of visualization can be easily

increased, since complicated image processing is not required to increase the number of channels. However, the total acquisition time increases in proportion to the number of channels for sequential acquisition. Thus, the surface coil array in sequential CW-EPR imaging cannot be applied to experiments that use a probe molecule with a short lifetime.

The experimental results in Figs. 3.6 and 3.7 demonstrate the developed surface coil array and control circuits under *in vitro* and *in vivo* conditions. As shown in Fig. 3.6, the area of visualization using the surface coil array was increased 3.5-fold in the X-direction compared to that with a single surface coil. If the author considered the area of overlap for the coils (see Fig. 3.3A), this is a reasonable result because the increase in area roughly corresponds to the dimensions of the surface coil array.

Although the author switched the coils and relevant circuits after obtaining a set of projection data for the entire single image acquisition with a single coil, two other protocols of switching timings are possible using the surface coil array. (i) Four coils can be switched in an interleave acquisition manner during a single field scan, and (ii) four coils can be switched sequentially after each projection is acquired under a given magnetic field gradient. Protocol (i) may be considered quasi-parallel acquisition. However, if protocol (i) is applied to the surface coil array system in this chapter, the required switching time in a single field scan will be approximately 30 seconds (15 ms × 512 points × 4 channels) if the author considered the switching rate of the RF coaxial switch. Due to this longer duration of switching, this approach would be less practical. However, if a faster RF coaxial switch with a switching rate on the order of microseconds is used, protocol (i) could be useful in animal imaging. In protocol (ii), a single field-scanning period is the same as the scanning period in this study. However, to acquire a set of projection data on each channel, every switching duration must be added to the time required for the acquisition of projections. While neither of these potential protocols offers any advantage from the perspective of the acquisition time,

they may be able to reduce the variance of EPR signal intensities for individual coils during the process of signal decay due to the reduction reaction of imaging agents in animals.

The surface coil array in this chapter has the advantages of an increased FOV and flexibility, as well as homogeneity of a large portion of the obtained image. With regard to the FOV, although it should also be possible to increase the FOV for a large surface coil resonator that consists of multiple loop segments [3.13] or a large volume coil that consists of multiple gaps and a single loop [3.14] by increasing the number of loop segments or gaps, the coils will need to be redesigned to achieve the desired frequency. Additionally, the overall shape of the coils is restricted. In contrast, in the surface coil array developed in this chapter, the FOV can be increased simply by adding coils, which all have the same dimension. Complicated calculation of the resonance frequency of the resonator is not required. Furthermore, there is no restriction regarding the overall shape of the surface coil array. Thus, the surface coil array can be formed to fit the shape of the subject, as with an array coil for the head or knee in MRI, which can be expected to improve the signal-to-noise ratio.

The homogeneity of the signal intensity over the broader region of the subject is greater than that with a single large coil. The distribution of the signal intensity of a single large coil tends to be stronger near the loop than that at the center of the coil. With the use of a small single coil, similar to the elements of the surface coil array developed in this chapter, the difference in signal intensity between near the loop and the center of the coil can be reduced because the magnetic flux density decreases inversely with the distance. Therefore, the surface coil array in this chapter could achieve greater homogeneity of the signal intensity for the subject surface, in comparison to a single large coil.

For a surface coil array, the sensitive area of EPR signals is localized near the subject surface. This is because the individual coils of the surface coil array were smaller in diameter than other types of coils. This is a suitable feature of a surface coil array for measurements of

a subject surface, such as the skin of mice.

The surface coil array required a difference of less than 5 MHz in the resonance frequencies of individual resonators because of its capacity for frequency adjustment. This might be a practical consideration for the fabrication of a multiple-channel surface coil array. An increase in the tunable frequency range should improve the tolerance for variance of the resonance frequencies of the individual resonators. The use of well-fabricated printed circuits using surface-mounted components could reduce the variance of the resonance frequencies of the individual resonators. If the number of channels continues to increase, this could become a technical issue in practical fabrication.

One of the practical considerations for the surface coil array in this article is the problem of interaction of the modulation field with varactors. If the potential voltage, which is applied to the varactors, at the end of the coaxial lines connected to the surface coil was influenced by magnetic field modulation, the resonance frequency of the resonator was modulated at the frequency of magnetic field modulation. This leads to impedance mismatching of the resonator and a shift in the baseline of EPR spectra. In the extreme case, it causes saturation of a lock-in amplifier used for the phase-sensitive detection of EPR absorption. To suppress such a shift in the EPR spectral baseline, the author constructed a high-pass filter (DC block) by inserting capacitors of 2.2 pF between the coaxial lines and the varactors, and placed the coils parallel to the modulation field. If the surface coil is not directly connected to the coaxial lines, this should solve the problem of the influence of magnetic field modulation. For example, if the capacitors are placed in series between the surface coil and the coaxial line, this technical issue can be addressed.

With regard to the sensitivity along the depth direction, the penetration depth (half of the maximum sensitivity at the center of the coil) determined experimentally in a mouse was 5.7 mm. This value in *in vivo* mouse experiments was not dramatically different from that in

the numerical model in muscle (6.1 mm).

A potential application of this surface coil array in EPR imaging is the visualization of imaging agents in the skin of animal disease models [3.30,3.31]. EPR volume coil resonators are not suitable for EPR imaging of skin, since the filling factor of a volume coil resonator will be low compared to that of a surface coil in general. This surface coil array could be a better approach for visualizing the distribution of EPR imaging agents in skin because it can take an advantage of the fact that a surface coil has better sensitivity for samples with a limited distribution for the depth of imaging agents.

3.5. Conclusions

This surface coil array could increase the area of visualization with no decrease in the performance of the resonators. The coil-selection circuits enabled the systematic switching of the developed coil array for EPR imaging *in vitro* and *in vivo*. Further progress in the development of array coils will be useful for topical and surface visualization in *in vivo* EPR imaging. The sequential acquisition method reported here is based on time-division multiplexing using a multiple-channel coil array. To really perform parallel acquisition, the author may need to apply frequency-division multiplexing. This further advancement may require a new concept for a multiple-channel surface coil array in CW-EPR imaging.

References

[3.1] S. Subramanian, K. Matsumoto, J. B. Mitchell, M. C. Krishna, Radio frequency continuous-wave and time-domain EPR imaging and Overhauser-enhanced magnetic resonance imaging of small animals: instrumental developments and comparison of relative merits for functional imaging, NMR Biomed. 17 (2004) 263–294.

[3.2] P. Kuppusamy, J.L. Zweier, Cardiac applications of EPR imaging, NMR Biomed. 17 (2004) 226–239.

[3.3] H. J. Halpern, D. P. Spencer, J. van Polen, M. K. Bowman, A. C. Nelson, E. M. Dowey, B.A. Teicher, Imaging radio frequency electron-spin-resonance spectrometer with high resolution and sensitivity for in vivo measurements, Rev. Sci. Instrum. 60 (1989) 1040−1050.

[3.4] S. Ishida, S. Matsumoto, H. Yokoyama, N. Mori, H. Kumashiro, N. Tsuchihashi, T. Ogata, M. Yamada, M. Ono, T. Kitajima, H. Kamada, E. Yoshida, An ESR-CT imaging of the head of a living rat receiving an administration of a nitroxide radical, Magn. Reson. Imaging. 10 (1992) 109–114.

[3.5] M. Chzhan, M. Shteynbuk, P. Kuppusamy, J. L. Zweier, An optimized L-band ceramic resonator for EPR imaging of biological samples, J. Magn. Reson. 105 (1993) 49−53.

[3.6] N. Devasahayam, S. Subramanian, R. Murugesan, J. A. Cook, M. Afeworki, R. G. Tschudin, J. B. Mitchell, M. C. Krishna, Parallel coil resonators for time-domain radiofrequency electron paramagnetic resonance imaging of biological objects, J. Magn. Reson. 142 (2000) 168–176.

[3.7] H. Hirata, T. Walczak, H. M. Swartz, Electronically tunable surface-coil-type resonator for L-band EPR spectroscopy, J. Magn. Reson.142 (2000) 159–167.

[3.8] S. Petryakov, M. Chzhan, A. Samouilov, G. He, P. Kuppusamy, J.L. Zweier, A

bridged loop-gap S-band surface resonator for topical EPR spectroscopy, J. Magn. Reson. 151 (2001) 124–128.

[3.9] A. Samouilov, G. L. Caia, E. Kesselring, S. Petryakov, T. Wasowicz, J. L. Zweier, Development of a hybrid EPR/NMR coimaging system, Magn. Reson. Med. 58 (2007) 156–166.

[3.10] G. R Eaton, S. S. Eaton, EPR spectrometers at frequencies below X-band, in: C.J. Bender, L. J. Berliner (Eds.), Biological Magnetic Resonance Vol. 21, Kluwer Academic/Plenum Publishers, New York, 2004, pp. 59–114.

[3.11] B. B. Williams, H. J. Halpern, In vivo EPR imaging, in: S.R. Eaton, G.R. Eaton, L.J. Berliner (Eds.), Biological Magnetic Resonance Vol. 23, Kluwer Academic/Plenum Publishers, New York, 2005, pp. 283–319.

[3.12] J. M. S. Hutchison, Frequency and power considerations for in vivo EPR and related techniques, in: L. J. Berliner (Ed.), Biological Magnetic Resonance Vol. 18, Kluwer Academic/Plenum Publishers, New York, 2003, pp. 41–59.

[3.13] S. Petryakov, A. Samouilov, M. Chzhan-Roytenberg, E. Kesselring, Z. Sun, J. L. Zweier, Segmented surface coil resonator for in vivo EPR applications at 1.1 GHz, J. Magn. Reson. 198 (2008) 8–14.

[3.14] S. Petryakov, A. Samouilov, E. Kesselring, T. Wasowicz, G. L. Caia, J. L. Zweier, Single loop multi-gap resonator for whole body EPR imaging of mice at 1.2 GHz, J. Magn. Reson. 188 (2007) 68–73.

[3.15] P. B. Roemer, W. A. Edelstein, C. E. Hayes, S.P. Souza, O.M. Mueller, The NMR phased array, Magn. Reson. Med. 16 (1990) 192–225.

[3.16] M. A. Ohliger, D. K. Sodickson, An introduction to coil array design for parallel MRI, NMR Biomed. 19 (2006) 300–315.

[3.17] D. J. Larkman, R. Nunes, Parallel magnetic resonance imaging, Phys. Med. Biol. 52

(2007) R15–R55.

[3.18] W. A. Willinek, J. Gieseke, M. von Falkenhausen, B. Neuen, H. H. Schild, C. K. Kuhl, Sensitivity encoding for fast MR imaging of the brain in patients with stroke, Radiology 228 (2003) 669–675.

[3.19] V. S. Lee, E. M. Hecht, B. Taouli, Q. Chen, K. Prince, N. Oesingmann, Body and cardiovascular MR imaging at 3.0 T, Radiology 244 (2007) 692–705.

[3.20] J. Cohen-Adad, A. Mareyam, B. Keil, J. R. Polimeni, L.L. Wald, 32-channel RF coil optimized for brain and cervical spinal cord at 3 T, Magn. Reson. Med. 66 (2011) 1198–1208.

[3.21] R. F. Lee, R. O. Giaquinto, C. J. Hardy, Coupling and decoupling theory and its application to the MRI phased array, Magn. Reson. Med. 48 (2002) 203–213.

[3.22] C. Constantinides, S. Angeli, Elimination of mutual inductance in NMR phased arrays: The paddle design revisited, J. Magn. Reson. 222 (2012) 59–67.

[3.23] J. S. Hyde, A. Jesmanowicz, W. Froncisz, J. B. Kneeland, T. M. Grist, Parallel image acquisition from noninteracting local coils, J. Magn. Reson. 70 (1986) 512–517.

[3.24] A. Enomoto, H. Hirata, Sequential CW-EPR image acquisition with 760-MHz surface coil array, J. Magn. Reson. 209 (2011) 244–249.

[3.25] A. Enomoto, H. Hirata, S. Matsumoto, K. Saito, S. Subramanian, M.C. Krishna, N. Devasahayam, Four-channel surface coil array for 300-MHz pulsed EPR imaging: Proof-of-concept experiments, Magn. Reson. Med. doi: 10.1002/mrm.24702 (2013).

[3.26] H. Sato-Akaba, Y. Kuwahara, H. Fujii, H. Hirata, Half-life mapping of nitroxyl radicals with three-dimensional electron paramagnetic resonance imaging at an interval of 3.6 seconds, Anal. Chem. 81 (2009) 7501–7506.

[3.27] H. Sato-Akaba, H. Fujii, H. Hirata, Development and testing of a CW-EPR apparatus for imaging of short-lifetime nitroxyl radicals in mouse head, J. Magn. Reson. 193

(2008) 191–198.

[3.28] E. C. Burdette, F. L. Cain, J. Seals, In vivo probe measurement technique for determining dielectric properties at VHF through microwave frequencies, IEEE Trans. Microwave Theory and Tech, MTT-28 (1980) 414–427.

[3.29] J. H. Freed, D. S. Leniart, J. S. Hyde, Theory of saturation and double resonance effects in ESR Spectra. III. RF coherence and line shapes, J. Chem. Phys. 47 (1967) 2762–2773.

[3.30] K. Takeshita, T. Takajo, H. Hirata, M. Ono, H. Utsumi, In vivo oxygen radical generation in the skin of the protoporphyria model mouse with visible light exposure: An L-band ESR study, J. Invest. Dermatol. 122 (2004) 1463–1470.

[3.31] K. Takeshita, C. Chi, H. Hirata, M. Ono, T. Ozawa, In vivo generation of free radicals in the skin of live mice under ultraviolet light, measured by L-band EPR spectroscopy, Free Radic. Biol. Med. 40 (2006) 876–885.

Chapter 4

Parallel image-acquisition in CW-EPR imaging with a surface coil array: Proof-of-concept experiments

4.1. Introduction

Fast image-acquisition of electron paramagnetic resonance (EPR) is required for target free radical molecules in small animals such as mice or rats, since exogenously injected imaging agents, free radical molecules, are rapidly metabolized or reduced in living animals [4.1]. While endogenously generated free radical molecules are often involved in physiological and pathophysiological processes from the level of cells to whole animals, even humans [4.2,4.3], they can be very challenging to visualize because of the limited sensitivity of an EPR imager. Under these conditions, exogenously injected imaging agents have been used to investigate the biological status, such as reduction/oxidation status, tissue oxygenation, and pH in tissue. Hence, the visualization of imaging agents in small animals is an important field of study in biomedical research. The ability to visualize a wider area should also be desirable for future EPR imaging in large animals or large organs in a human subject. Regarding the skin of humans or animals, several dermatological studies have used EPR spectroscopy and imaging [4.4–4.9]. While there have been several reports of *in vivo* EPR imaging of the skin, the visualization areas were limited to the size of the coils used in the experiments. When a diagnosis or investigation is performed over a wide region of skin, the visualization of a larger area is required to completely cover the area being investigated.

To extend the area of visualization, phased array coils have been used in ^{1}H-magnetic resonance imaging (MRI) in a clinical setting to achieve fast image-acquisition, a large field-of-view (FOV), and high sensitivity [4.10–4.12]. In modern MRI, the transmitter channel for nuclear-spin excitation and the receiver channels for signal detection are separate

from each other. Thus, multiple receiver channels can be used in a phased array coil without increasing the number of transmitter channels in MRI. In commonly used reflection-type RF bridges in CW-EPR spectrometers, however, electromagnetic waves for electron-spin excitation and reflected waves that are modulated due to EPR absorption pass through the same transmission line. Hence, the phased array coil system used in MRI has not been used in CW-EPR imaging. In Chapter 2 and Chapter 3, the author reported a surface coil array that enables the sequential switching of individual coils for CW-EPR imaging [4.13,4.14]. However, the acquisition time increased with the number of coils under sequential acquisition [4.15]. Instead of sequential acquisition by the multiplexing of EPR detection in the time domain, parallel image-acquisition requires a different approach, such as multiplexing of EPR detection in the frequency domain, which has not been used in CW-EPR imaging previously. The purpose of this work was to perform proof-of-concept experiments for the multiplexing of EPR detection in the frequency domain. Through the experiments, the author also clarified technical challenges in the multiplex method in the frequency domain for further investigation. In this chapter, the author demonstrated parallel EPR signal acquisition and three-dimensional (3D) imaging of a phantom with a two-channel surface coil array, based on the multiplexing of EPR detection in the frequency domain.

4.2. Methods

4.2.1. Multiplexing of EPR detection in the frequency domain

The principle of parallel detection is to excite electron spins by the use of multiple RF frequencies and multiple coils in a polarizing magnetic field. This approach involves the multiplexing of EPR detection in the frequency domain. With different RF frequencies, multiple EPR absorption peaks appear at different magnetic fields that are governed by the Zeeman effect. With the use of multiple EPR detection systems, EPR absorption spectra can

be simultaneously detected at different RF frequencies. Mutual inductive coupling between the coils should be a practical consideration for the simultaneous detection of EPR absorption signals with multiple RF resonators. To prove the concept of parallel EPR imaging based on the multiplexing of EPR detection in the frequency domain, the author built a two-channel parallel detection system in a 750-MHz CW-EPR imager.

4.2.2. Experimental setup

Figure 4.1 presents an overview of the laboratory-built 750-MHz CW-EPR imager for parallel detection of the surface coil array. To suppress mutual inductive coupling between two coils, the resonance frequencies of the individual surface coil resonators were different from each other. The author set the resonance frequencies of the resonators to be approximately 50 MHz apart, which is the smallest difference at which the author could maintain the reflection of RF waves (S_{11}) to less than -1 dB at the resonance frequency of the other resonator. The details of the EPR spectrometer/imager have been reported elsewhere [4.16]. The RF bridges in this study were built according to the design of an L-band CW-EPR bridge described in the literature [4.17]. To detect EPR signals, a double balanced mixer (M2BC, M/A-COM Technology Solution Inc., Lowell, MA) and a low-pass filter were used for RF homodyne detection. The main magnet (27 mT), gradient coils and sweep coils were shared between the two resonators. Data acquisition was performed simultaneously with each resonator. After EPR data acquisition, images of EPR absorption were separately reconstructed and combined using MATLAB (MathWorks, Natick, MA)-based software to obtain the final image.

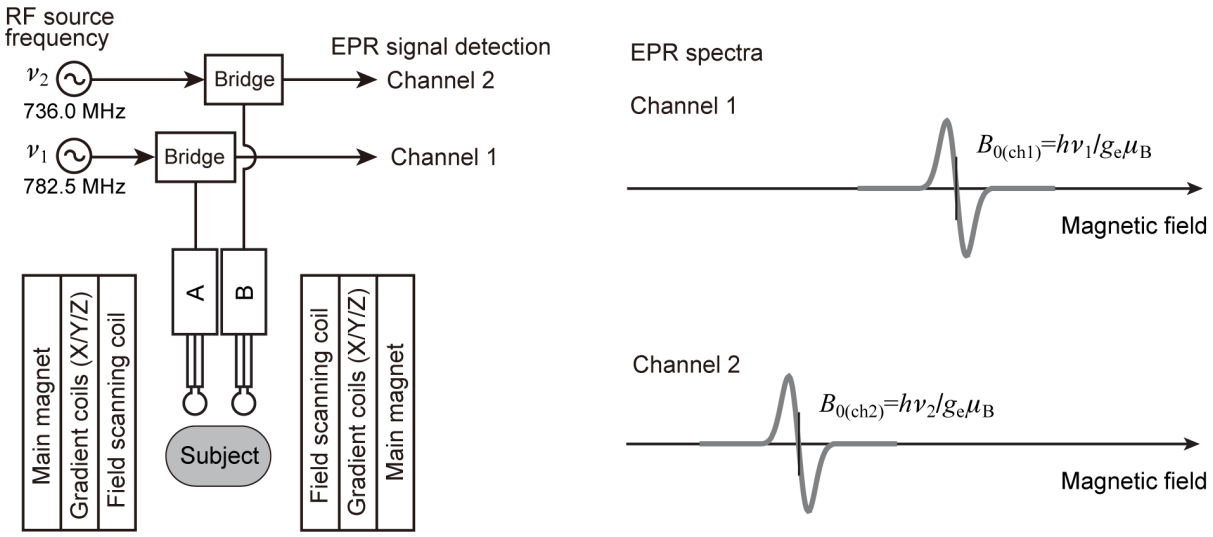


Fig. 4.1. Schematic diagram of the experimental setup for parallel EPR image-acquisition using a surface coil array. Two RF signal sources generate carrier signals with different frequencies (ν_1 and ν_2). The lower panel shows the concept of spectral detection from individual RF bridges at different frequencies. First-derivative EPR absorption spectra appear at different external magnetic fields, $B_{0(ch1)}$ and $B_{0(ch2)}$. These magnetic fields are determined by the RF frequencies (ν_1 and ν_2), electron g-factor g_e, Bohr magneton μ_B, and Plank constant h.

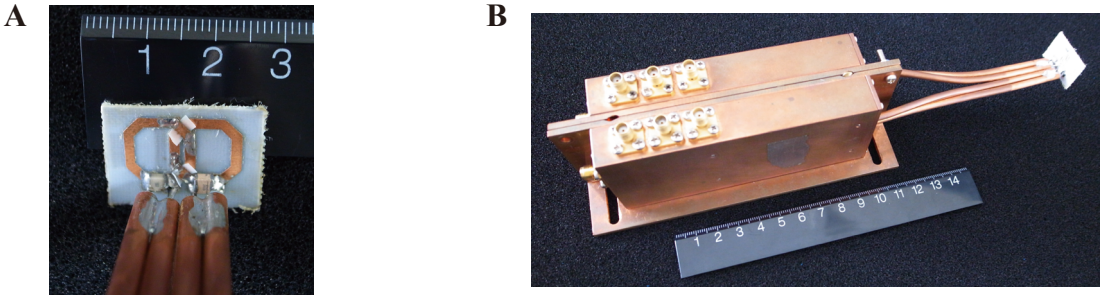


Fig. 4.2. Photographs of surface coils (A) and the whole resonators (B).

Figure 4.2 shows photographs of the surface coils and the whole resonators. The configuration of the surface coil resonators has been reported elsewhere [4.13]. Two surface coils were fabricated by the use of a copper-laminated substrate (NPC-H220A, Nippon Pillar Packing Corp., Osaka, Japan). The inner size of the coils was 8 × 8 mm and the width of the copper line s was 1.6 mm. The coils were overlapped to minimize mutual coupling with the other coil. To electrically insulate the coils from each other, polytetrafluoroethylene (PTFE)

sheets (0.1-mm thick) were inserted into the overlapping regions. To investigate the resonance frequency of each resonator and decoupling between the two coils, the author measured the scattering-matrix parameters of each resonator (S_{11} and S_{22}) and the transmission characteristics between the two resonators (S_{21} and S_{12}). The quality factor Q and the generation efficiency of RF magnetic fields Λ were also measured to clarify the performance of the resonators. The generation efficiencies of RF magnetic fields Λ were measured by the perturbing metal sphere method [4.18]. All characteristics of the resonators were measured using an RF network analyzer (E5062A, Agilent Technologies, Palo Alto, CA).

4.2.3. EPR spectroscopy

To demonstrate parallel detection capability with the two-channel surface coil array, EPR spectra were obtained when RF waves were fed to only one resonator or to both resonators simultaneously. The author used a glass cell (10 × 20 × 45 mm) filled with 2 mM 4-oxo-2,2,6,6-tetramethylpiperidine-1-oxyl (Tempone) aqueous solution to obtain first-derivative EPR absorption spectra. The parameters for data-acquisition of EPR spectra were as follows: scanning field 10 mT, magnetic field modulation 0.08 mT, modulation frequency 90 kHz, field scanning duration 1 s, time constant of lock-in amplifier 1 ms, applied RF power 4.0 mW for resonator A at 782.5 MHz and 4.5 mW for resonator B at 736.0 MHz, and 100 averages. Since two separate RF bridges were used for each resonator, RF powers could not be precisely adjusted to the same level.

4.2.4. Relation between the EPR signal intensity and the incident RF power

To clarify the status of power-saturation of the electron spin system when a single resonator was fed and when both channels were fed simultaneously, the EPR signal

intensities of channel 1 were plotted as a function of the incident RF power to the resonator in each case. The author used a Tempone phantom similar to the experiments described in section 2.3. The parameters for data-acquisition of EPR spectra were as follows: scanning field 10 mT, magnetic field modulation 0.08 mT, modulation frequency 90 kHz, field scanning duration 1 s, time constant of the lock-in amplifier 1 ms, and incident RF power to the resonator 0.4 mW to 12.6 mW.

4.2.5. EPR imaging

To demonstrate the feasibility of this method of parallel image-acquisition, the author measured 3D EPR images of a phantom that consisted of two quartz tubes (outer diameter 5 mm, inner diameter 4 mm) placed in parallel with a gap of 6 mm. The tubes were filled with 2 mM 2,2,6,6-tetramethylpiperidine-d_{16}-1-oxyl (perdeuterated Tempone) aqueous solution. The FOV was set to 100 mm. The parameters for EPR imaging were as follows: scanning field 10 mT, magnetic field gradient 100 mT/m, magnetic field modulation 0.09 mT, modulation frequency 90 kHz, field scanning duration 1 s, time constant of lock-in amplifier 1 ms, applied RF power 4.0 mW for resonator A at 782.5 MHz and 4.5 mW for resonator B at 736.0 MHz, number of projections 181, and two averages. The total image-acquisition time was 7.5 min. The one-step 3D filtered-back projection method was used in image reconstruction for individual surface coils [4.19].

4.3. Results

4.3.1. Decoupling of two resonators

Figure 4.3 shows the reflection (S_{11} and S_{22}) and transmission characteristics (S_{21} and S_{12}) of the surface coil resonators. Based on Figs. 4.3A and 4.3B, the resonance frequencies of the two resonators were 782.5 MHz (resonator A) and 736.0 MHz (resonator B). In both

traces, in addition to the main peak of the resonance frequency, a peak of less than -1 dB appeared at the frequency around the resonance frequency of the other resonator. The quality factor Q and the generation efficiency of RF magnetic fields Λ of resonator A were 146 and 53 μT/W$^{1/2}$, and those of resonator B were 152 and 59 μT/W$^{1/2}$ respectively. As shown in Figs. 4.3C and 4.3D, two peaks (S_{21} and S_{12}) appeared at the resonance frequencies of the two resonators. Based on the transmission characteristics shown in Fig. 4.3, decoupling of the two coils was -16 dB at 736.0 MHz and -21 dB at 782.5 MHz.

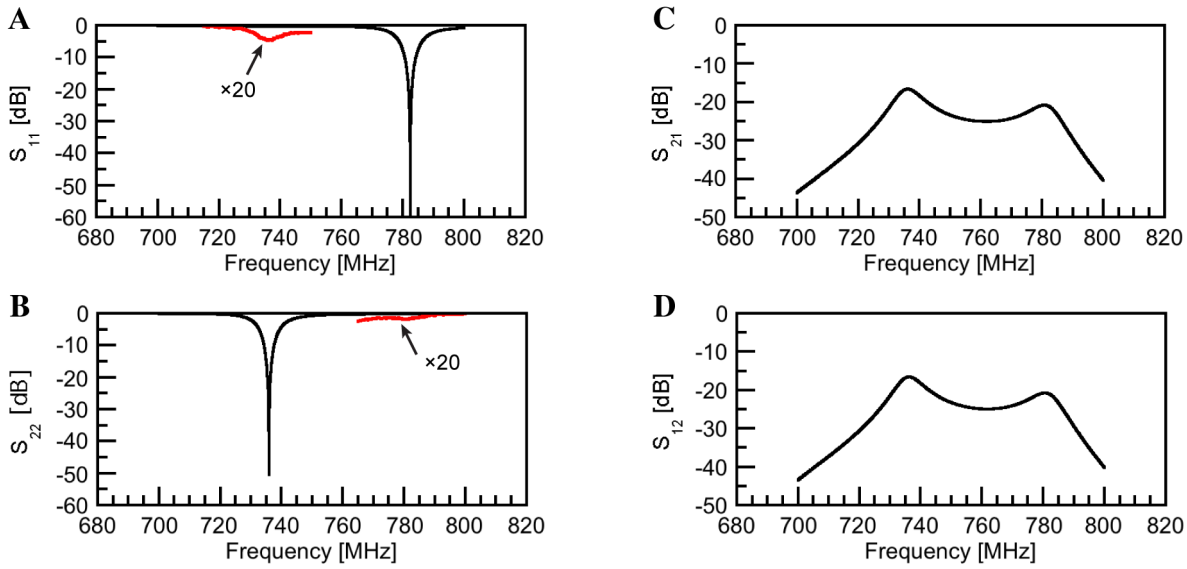


Fig. 4.3. Scattering-matrix parameters (S_{11} and S_{22}) of each resonator and the transmission characteristics for both directions (S_{21} and S_{12}) when resonator A is connected to port 1 and resonator B is connected to port 2 of the RF network analyzer. (A) Scattering-matrix parameter S_{11} for resonator A. (B) Scattering-matrix parameter S_{22} for resonator B. (C) Transmission characteristics from resonator A to resonator B (S_{21}). (D) Transmission characteristics from resonator B to resonator A (S_{12}).

4.3.2. EPR spectra in parallel detection

Figure 4.4 shows EPR spectra for when only one resonator was fed and when both resonators were fed simultaneously. Figures 4.4A and 4.4C show first-derivative EPR absorption spectra measured with resonator A. Figures 4.4B and 4.4D show first-derivative EPR absorption spectra obtained with resonator B. The signal-to-noise ratios (SNRs) with

one resonator were approximately 155 in both spectra in Figs. 4.4A and 4.4B, and the SNRs when the two resonators were operated at the same time were approximately 70 in both spectra (Figs. 4.4C and 4.4D).

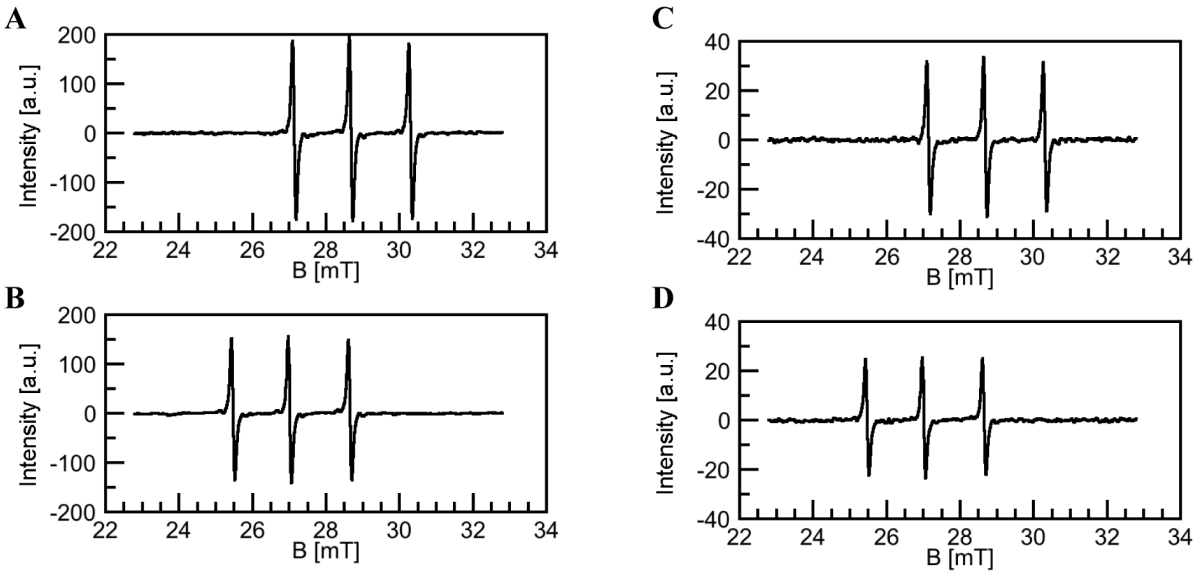


Fig. 4.4. EPR spectra obtained by the individual resonators when RF waves were fed to one resonator alone (4.4A and 4.4B) or to the individual resonators simultaneously (4C and 4D). EPR spectra shown in Figs. 4.4A and 4.4C were obtained from resonator A (782.5 MHz). Those shown in Figs. 4.4B and 4.4C were obtained from resonator B (736.0 MHz).

4.3.3. EPR signal intensity as a function of incident RF power

Figure 4.5 shows the relation between the EPR signal intensity and the square root of RF input power. Under the condition of single-resonator feeding, the EPR signal intensity increased in proportion to the square root of the RF input power. This means that the measured electron spin system was not saturated under these levels of incident RF power. In contrast, the EPR signal intensity under simultaneous feeding of both resonators did not increase regardless of the incident RF power. This suggests saturation of the receiver system in the EPR spectrometer, such as in an RF amplifier. This saturation of the EPR signal intensity is discussed later.

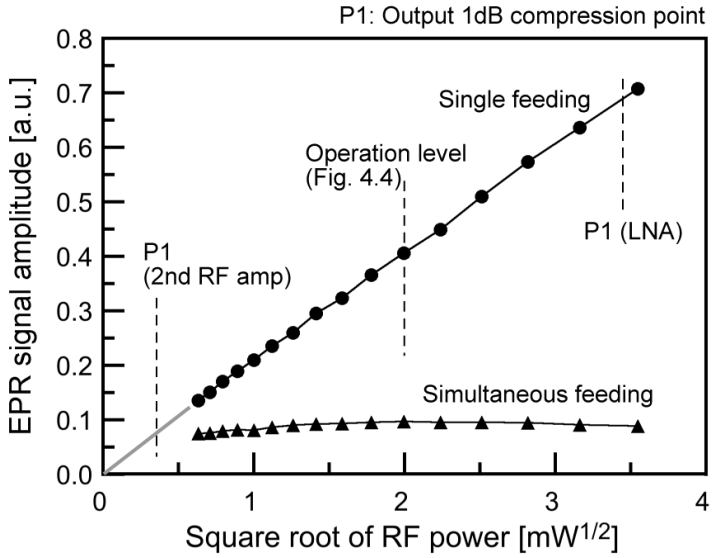


Fig. 4.5. Relation between the EPR signal intensity and the incident RF power when RF waves were fed to only one resonator (closed circles) or to both resonators simultaneously (closed triangles). The output 1 dB compression points (P1) of a low-noise amplifier (LNA) and the second RF amplifier are also indicated under a -16 dB decoupling of the resonators and a -3 dB transmission loss in a 180-degree hybrid. The gains of LNA at the first stage and an RF amplifier at the second stage were 17 dB and 19 dB, respectively.

4.3.4. EPR imaging in parallel detection

Figure 4.6 shows the arrangement of the tube phantom and the resulting 3D EPR images. In Figs. 4.6B–4.6G, the FOV was changed from 100 mm to 30 mm after image reconstruction. Figures 4.6B and 4.6C were obtained with individual resonators. The image shown in Fig. 4.6D was created by combining the two images in Figs. 4.6B and 4.6C. Figures 4.6E–4.6G show slice-selective images generated from the 3D combined image in the YZ-, XZ- and XY-planes. The threshold of surface rendering for all 3D images was set to 50% of the peak signal intensity.

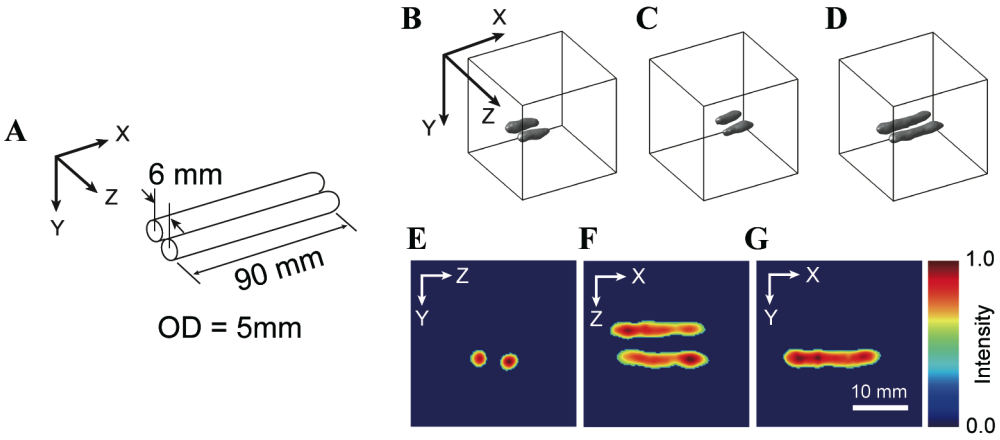


Fig. 4.6. 3D EPR images measured by parallel data-acquisition. (A) Arrangement of the tube phantom filled with 2 mM perdeuterated Tempone solution (1.1 mL). (B) 3D EPR images measured with resonator A at 782.5 MHz. (C) 3D EPR images measured with resonator B at 736.0 MHz. (D) Combined 3D EPR image. (E)-(G) slice-selective images generated from the 3D image in Fig. 4.6C. The threshold of surface rendering for all 3D images was set to 50% of the peak signal intensity.

4.4. Discussion

While small peaks appeared at the resonance frequency of the other resonator (Figs. 4.3A and 4.3B), the EPR spectra shown in Fig. 4.4 were not affected by the resonant peak of the resonator connected to the other receiver system. In addition, the transmission coefficients shown in Figs. 4.3C and 4.3D were -16 dB and -21 dB at the resonance frequencies. These results show that decoupling between coils was reasonably achieved by shifting the resonance frequencies of the resonators. However, according to the results in Fig. 4.4, the SNR achieved by simultaneous acquisition was decreased to approximately 40% of that under single-resonator feeding. Specifically, the signal intensity of EPR absorption was decreased to 17%, and the noise was decreased to 42% compared to data acquisition with single-resonator feeding. When the incident RF power of one channel was decreased, the SNR for the other channel recovered. Degraded SNR is crucial in simultaneous EPR detection using different RF frequencies. If the author can solve the problem of degradation in SNR, faster EPR image-acquisition should be possible with parallel acquisition.

The author found that the gain compression of an RF amplifier in the receiver system

was a major reason for EPR signal reduction under simultaneous feeding. This phenomenon is similar to intermodulation distortion in analog radio communications. The leakage signals from the incident RF power for the other channel were amplified with two RF amplifiers in the receiver system, i.e., a low-noise amplifier (LNA) (power gain of 17 dB, AFS1-00700080-08-13P-4, MITEQ Inc., Hauppauge, NY) at the first stage and an RF amplifier (power gain of 19 dB, ZJL-3G, Mini-Circuits Inc., Brooklyn, NY) at the second stage. If the leakage of RF signals in the surface coil array was -16 dB (see Fig. 4.3) below the incident RF power (4 mW (6 dBm)) and the transmission loss in the 180-degree hybrid used in the receiver system was -3 dB, the output of the RF amplifier at the second stage became 23 dBm, with the assumption of no gain compression. In reality, this output level of the RF amplifier was beyond the output 1 dB compression point (8 dBm) of the RF amplifier the author used. In Fig. 4.5, extrapolation of the plots for the EPR signal intensity (gray line) and the 1 dB compression point of the RF amplifier converted to the incident RF power to the resonator (-9 dBm) cross at a level similar to the EPR signal intensity under simultaneous feeding. This non-linearity in the receiver system can explain the decrease in the EPR signal intensity under simultaneous feeding. To avoid this reduction in the EPR signal, further investigations will be required, along with optimization of design of the surface coil array and the receiver system in the EPR spectrometer. Possible approaches to recovering the EPR signals under simultaneous feeding include (i) improved decoupling of surface coils, (ii) filtering of RF signal leakage from the other channel(s), (iii) use of an RF amplifier with an output 1 dB compression point that is high enough to prevent gain compression, and (iv) removal of the RF amplifier at the second stage after LNA.

Three-dimensional EPR imaging of the phantom is shown in Fig. 4.6. In Figs. 4.6E and 4.6F, the diameter of the tube measured from the images was approximately 3.1 mm, which is smaller than the inner diameter of the phantom tube. The intensity of EPR signals near the

wall of the tube was lower than that at the center of the tube. Since a signal intensity of less than 50% of the peak intensity was not seen in surface-rendered images, the signals near the wall of the tube were not visualized in surface-rendered images.

The acquisition time is essentially half of the total acquisition time for when the author used the two-channel surface coil array in a sequential acquisition manner under the same parameters. In this chapter, the acquisition time was longer than that for sequential acquisition, since the signal was accumulated twice due to the lower SNRs of detected signals. In addition to the challenge associated with the SNR, another technical concern is the width of field scanning, when multiple resonators (RF frequencies) are used. If a series of monotonically increasing RF frequencies is used in the experiments, the width of field scanning is also increased to record EPR spectra for all resonators. In that case, the author has to consider the limitation of field scanning in the experimental setup. However, if the resonators are well decoupled in the experiments, a series of monotonically increasing RF frequencies is not necessarily required. The author can repeatedly assign several RF frequencies to the multiple resonators that are electromagnetically decoupled in the surface coil array. Under these conditions, the width of field scanning does not increase in proportion to the number of coils in the array.

Since the circumference of the coil needs to be small in comparison to the electromagnetic wavelength to generate rather homogeneous RF magnetic fields in the coils [4.20–4.25], a single large coil is not feasible under the conditions of CW-EPR imaging. Thus, a parallel detection method using the surface coil array reported here may be a practical solution for the visualization of larger areas.

4.5. Conclusion

In conclusion, the author has demonstrated the feasibility of parallel EPR

image-acquisition with a surface coil array. For decoupling between the two coils, the two resonance frequencies were set to individual channels, and the author suppressed mutual coupling of the two coils. The author found that the decrease in SNR due to the interference of RF carriers is an important technical problem in the multiplex method reported here. Although there is still a problem of degradation in SNR, the concept of the multiplexing of EPR detection in the frequency domain was demonstrated in CW-EPR imaging.

References

[4.1] H. M. Swartz, M. Sentjurc, N. Kocherginsky, in *Nitroxide Spin Labels: Reactions in Biology and Chemistry*, edited by N. Kocherginsky and H. M. Swartz (CRC Press, Boca Raton, 1995), pp. 153–173.

[4.2] M. Valko, D. Leibfritz, J. Moncol, M. T. D. Cronin, M. Mazur, J. Telser, Free radicals and antioxidants in normal physiological functions and human disease, Int. J. Biochem. Cell Biol. 39 (2007) 44–84.

[4.3] S. Raha, B. H. Robinson, Mitochondria, oxygen free radicals, disease and ageing, Trends Biochem. Sci. 25 (2000) 502–508.

[4.4] P. M. Plonka, Electron paramagnetic resonance as a unique tool for skin and hair research, Exp. Dermatol. 18 (2009) 472–484.

[4.5] T. E. Herrling, N. K. Groth, J. Fuchs, Biochemical EPR imaging of skin, Appl. Magn. Reson. 11 (1996) 471–486.

[4.6] G. He, A. Samouilov, P. Kuppusamy, J. L. Zweier, In vivo EPR imaging of the distribution and metabolism of nitroxide radicals in human skin, J. Magn. Reson. 148 (2001) 155–164.

[4.7] G. He, V. K. Kutala, P. Kuppusamy, J. L. Zweier, In vivo measurement and mapping of skin redox stress induced by ultraviolet light exposure, Free Radic. Biol. Med. 36 (2004) 665–672.

[4.8] K. Takeshita, T. Takajo, H. Hirata, M. Ono, H. Utsumi, In vivo oxygen radical generation in the skin of the protoporphyria model mouse with visible light exposure: An L-band ESR study, J. Invest. Dermatol. 122 (2004) 1463–1470.

[4.9] K. Takeshita, C. Chi, H. Hirata, M. Ono, T. Ozawa, In vivo generation of free radicals in the skin of live mice under ultraviolet light, measured by L-band EPR spectroscopy, Free Radic. Biol. Med. 40 (2006) 876–885.

[4.10] P. B. Roemer, W. A. Edelstein, C. E. Hayes, S. P. Souza, O. M. Mueller, The NMR phased array, Magn. Reson. Med. 16 (1990) 192–225.

[4.11] M. A. Ohliger, D. K. Sodickson, An introduction to coil array design for parallel MRI, NMR Biomed. 19 (2006) 300–315.

[4.12] D. J. Larkman, R. G. Nunes, Parallel magnetic resonance imaging, Phys. Med. Biol. 52 (2007) R15–R55.

[4.13] A. Enomoto, H. Hirata, Sequential CW-EPR image acquisition with 760-MHz surface coil array, J. Magn. Reson. 209 (2011) 244–249.

[4.14] A. Enomoto, M. Emoto, H. Fujii, H. Hirata, Four-channel surface coil array for sequential CW-EPR image acquisition, J. Magn. Reson. 234 (2013) 21–29.

[4.15] J. S. Hyde, A. Jesmanowicz, W. Froncisz, J. B. Kneeland, T. M. Grist, Parallel image acquisition from noninteracting local coils, J. Magn. Reson. 70 (1986) 512–517.

[4.16] H. Sato-Akaba, Y. Kuwahara, H. Fujii, H. Hirata, Half-life mapping of nitroxyl radicals with three-dimensional electron paramagnetic resonance imaging at an interval of 3.6 seconds, Anal. Chem. 81 (2009) 7501–7506.

[4.17] T. Walczak, P. Lesniewski, I. Salikhov, A. Sucheta, K. Szybinski, H. M. Swartz, L-band electron paramagnetic resonance spectrometer for use in vivo and in studies of aqueous biological samples, Rev. Sci. Instrum. 76 (2005) 013107.

[4.18] J. H. Freed, D. S. Leniart, J. S. Hyde, Theory of saturation and double resonance effects in ESP spectra. RF coherence and line shapes, J. Chem. Phys. 47 (1967) 2762–2773.

[4.19] H. Sato-Akaba, H. Fujii, H. Hirata, Development and testing of a CW-EPR apparatus for imaging of short-lifetime nitroxyl radicals in mouse head, J. Magn. Reson. 193 (2008) 191–198.

[4.20] H. J. Halpern, D. P. Spencer, J. van Polen, M. K. Bowman, A. C. Nelson, E. M. Dowey, B. A. Teicher, Imaging radio frequency electron-spin-resonance spectrometer with high resolution and sensitivity for in vivo measurements, Rev. Sci. Instrum. 60 (1989) 1040–1050.

[4.21] S. Ishida, S. Matsumoto, H. Yokoyama, N. Mori, H. Kumashiro, N. Tsuchihashi, T. Ogata, M. Yamada, M. Ono, T. Kitajima, H. Kamada, E. Yoshida, An ESR-CT imaging of the head of a living rat receiving an administration of a nitroxide radical, Magn. Reson. Imaging. 10 (1992) 109–114.

[4.22] M. Chzhan, M. Shteynbuk, P. Kuppusamy, J. L. Zweier, An optimized L-band ceramic resonator for EPR imaging of biological samples, J. Magn. Reson. 105 (1993) 49–53.

[4.23] N. Devasahayam, S. Subramanian, R. Murugesan, J. A. Cook, M. Afeworki, R. G. Tschudin, J. B. Mitchell, M. C. Krishna, Parallel coil resonators for time-domain radiofrequency electron paramagnetic resonance imaging of biological objects, J. Magn. Reson. 142 (2000) 168–176.

[4.24] H. Hirata, T. Walczak, H. M. Swartz, Electronically tunable surface-coil-type resonator for L-band EPR spectroscopy, J. Magn. Reson. 142 (2000) 159–167.

[4.25] S. Petryakov, M. Chzhan, A. Samouilov, G. He, P. Kuppusamy, J. L. Zweier, A bridged loop–gap S-band surface resonator for topical EPR spectroscopy, J. Magn. Reson. 151 (2001) 124–128.

Chapter 5

Elimination of signal saturation under parallel detection in CW-EPR imaging

5.1. Introduction

Electron paramagnetic resonance (EPR) imaging has been used to visualize the distribution of target free radicals in small animals non-invasively [5.1–5.5]. For *in vivo* EPR imaging, fast image data acquisition is desirable, since exogenously injected target free radical molecules in living animals are rapidly reduced or metabolized in animal bodies [5.6–5.9]. In addition, EPR imaging should be able to achieve a visualization area broad enough to cover the whole body of larger animals or a broad area of large organs, such as skin [5.10–5.12]. However, it is not easy to extend the visualization area by using large-diameter surface coils, since the diameter of radio-frequency (RF) coils depends on the operating frequency used to generate the RF magnetic fields for exciting electron spins [5.13]. In proton magnetic resonance imaging (MRI), phased array coils have long been used to extend the visualization area without compromising the detection sensitivity or increasing the data acquisition time [5.14]. However, phased array coils cannot be applied to CW-EPR imaging due to the difference in their signal detection systems.

To assess the feasibility of using surface coil arrays in CW-EPR imaging, the author previously demonstrated (i) sequential data acquisition by multiplexing in the time domain [5.15–5.17] and (ii) parallel data acquisition by multiplexing in the frequency domain [5.18]. If EPR image data could be acquired with multiple channels simultaneously, parallel EPR signal detection should be more effective for *in vivo* EPR measurements than sequential EPR signal detection in terms of the acquisition time. In Chapter 4, the author demonstrated the concept of parallel EPR detection by multiplexing in the frequency domain [5.18]. However, a major technical problem with parallel EPR detection is the significant reduction in the

signal-to-noise ratio (SNR) for measured EPR spectra due to saturation of the EPR signal intensity under the simultaneous RF feeding to multiple channels. Due to the degradation of the SNR in EPR spectra, in the experiments in Chapter 4, a longer data acquisition time was required to obtain three-dimensional (3D) images with less noise and a spatial resolution sufficient to distinguish two tubes placed in close proximity. Furthermore, the sensitivity of EPR signal detection in *in vivo* measurements is generally lower than that in *in vitro* measurements, since RF electromagnetic waves are absorbed by conductive animal tissues. As a result of the lower sensitivity of EPR signal detection, it was expected that a longer acquisition time would be required for *in vivo* animal measurements. Thus, it was difficult to apply the parallel detection method proposed in Chapter 4 to the *in vivo* EPR imaging of living mice.

The purpose of this study was to improve the SNR in the parallel EPR detection scheme using multiple channels and to demonstrate the feasibility of *in vivo* EPR imaging with parallel EPR detection. The author previously learned that the main reason for the reduction in the SNR was saturation of an RF amplifier in the receiver system [5.18]. Thus, the author removed the amplifier from the RF bridge of the EPR spectrometer used in the author's laboratory to improve the parallel EPR detection system. In this study, the author clarified the influence of the saturation of the amplifier on parallel EPR signal detection. In addition, the author demonstrated *in vivo* 3D imaging of exogenously injected imaging agents in a subject mouse.

5.2. Methods

5.2.1. Experimental setup

Parallel detection for CW-EPR was performed with a surface coil array and multiple RF bridges corresponding to individual coils. This is because parallel detection in CW-EPR

was based on the multiplexing of EPR detection in the frequency domain. Figure 5.1A provides an overview of a laboratory-built 750-MHz CW-EPR imager for parallel detection using a surface coil array. Figure 5.1B shows a photograph of the surface coil array used in these experiments. The details of this surface coil array have been reported elsewhere [5.18]. With the use of multiple frequencies, it was possible to suppress mutual inductive coupling between the coils. However, the difference between the operating frequencies should be as small as possible to avoid broader magnetic field scanning that would cause low spatial resolution. Thus, the difference between the resonant frequencies of individual coils was set to approximately 50 MHz. This difference was the smallest value that was still sufficient to suppress mutual inductive coupling, as described in the author's previous report (Chapter 4 and [5.18]). The resonant frequencies of the individual coils were 783 MHz (channel 1) and 731 MHz (channel 2), respectively. The transmission characteristics (S_{12} and S_{21}) of the two coils were -18 dB at 731 MHz and -20 dB at 783 MHz. EPR signals were measured

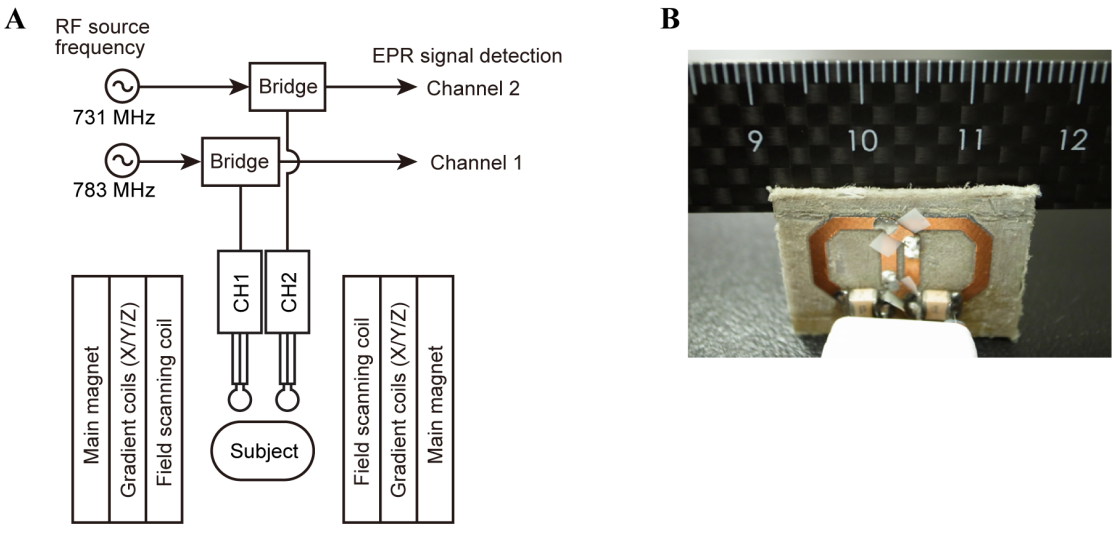


Fig. 5.1. Overview of the experimental setup for CW-EPR imaging with the multiplexing of EPR detection in the frequency domain. (A) Schematic diagram of the EPR imager using the parallel detection scheme. (B) Photograph of the two-channel surface coil array.

simultaneously using both channels. EPR image data obtained with the individual channels were reconstructed separately and combined using the root of sum of squares method.

Figure 5.2 shows a diagram of the individual RF bridge used in the CW-EPR imager that the author used. In the RF bridge, two RF amplifiers, which consisted of a low-noise amplifier (power gain of 17 dB, AFS1-00700080-08-13P-4, MITEQ Inc., Hauppauge, NY) at the first stage and an RF amplifier (power gain of 21 dB, ZJL-3G, Mini-Circuits Inc., Brooklyn, NY) at the second stage, were used before RF homodyne detection with a double balanced mixer (M2BC, M/A-COM Technology Solutions Inc., Lowell, MA). In addition, the output 1 dB compression points for each amplifier were 13 dBm and 8 dBm, respectively. Although the reflection waves from a surface coil resonator (an element of the surface coil array) were amplified by these two amplifiers, the author previously observed saturation of the signal intensity for the second amplifier. Thus, in the present study, the second RF amplifier was removed to prevent this saturation of the signal intensity and to improve the sensitivity of EPR signal detection.

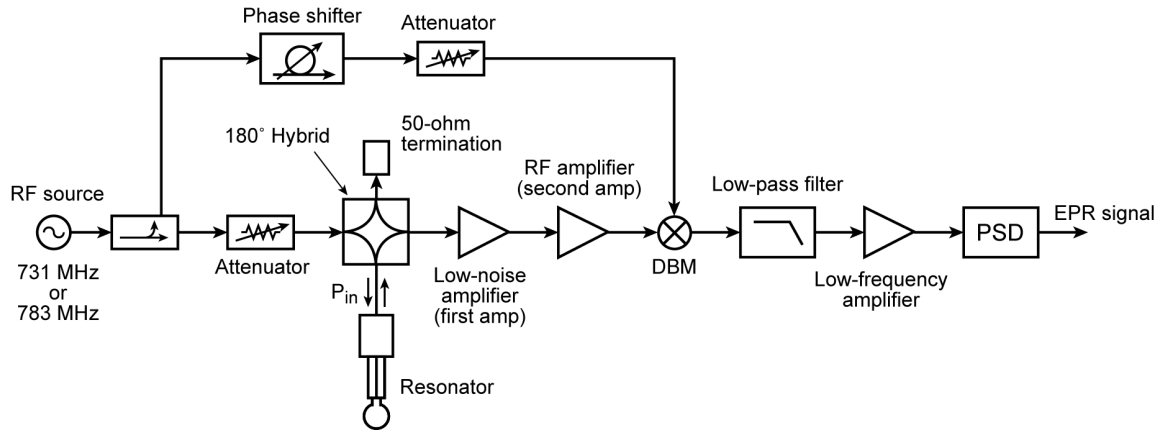


Fig. 5.2. Schematic diagram of the reflection-type RF circuit used for CW-EPR spectroscopy/imaging.

5.2.2. Relation between EPR signal intensity and incident RF power

To verify the influence of the second amplifier on saturation of the EPR signal intensity, the author determined the relation between the EPR signal intensity and the incident RF power. In this experiment, EPR signal intensities were measured as a function of the incident RF power when a single resonator was fed and when both resonators were fed simultaneously. The experiments were repeated with and without the second amplifier. The EPR signal intensity was measured using the peak-to-peak amplitude of EPR spectra obtained from channel 1. The incident RF power of each channel was adjusted with attenuators so that the incident RF powers of both channels were almost the same. The author used a quartz glass cell (10 × 20 × 45 mm) filled with 2 mM 4-oxo-2,2,6,6-tetramethylpiperidine-1-oxyl (Tempone) aqueous solution to obtain first-derivative EPR absorption spectra. The parameters for data-acquisition of EPR spectra were as follows: scanning field 10 mT, magnetic field modulation 0.08 mT, modulation frequency 90 kHz, field scanning duration 1 s, time constant of the lock-in amplifier 1 ms, data sampling 1024 points per field scanning, and incident RF power to the resonator approximately 0.02 mW to 11 mW at channel 1. EPR spectra were acquired 100 times at each level of incident RF power. The signal intensity of EPR spectra was obtained from the mean value of the peak-to-peak signal intensities calculated from these 100 EPR spectra.

5.2.3. Measured SNR with and without the second amplifier

To investigate the effect of removing the second amplifier on the SNRs of EPR spectra, the author compared the SNRs with and without the second amplifiers in RF bridges. The SNRs of EPR spectra were measured separately for each channel. The measurements were repeated 100 times at several levels of incident RF power. The SNRs were calculated from the ratio of the peak-to-peak signal intensity at the lower peak of a three-line first-derivative

EPR absorption spectrum divided by the two-fold standard deviation (2σ) of noise in the spectral baseline (100 points). A phantom cell similar to the experiments described in section 2.2 was used for measurements of the SNRs. The parameters for data-acquisition of EPR spectra were as follows: scanning field 10 mT, magnetic field modulation 0.08 mT, modulation frequency 90 kHz, field scanning duration 1 s, time constant of the lock-in amplifier 1 ms, data sampling 1024 points per field scanning, and incident RF power to the resonator approximately 0.5 mW, 1.0 mW, 5.0 mW, 10 mW and 16 mW at each channel.

5.2.4. Comparison of the SNRs under single feeding and simultaneous feeding

To clarify the influence of the second amplifier on parallel EPR detection, the author measured the SNRs of EPR signals when only a single resonator was fed and when both resonators were fed simultaneously at the same incident RF power. The SNRs were measured both with and without the second amplifiers in the RF bridges of both channels. SNRs were obtained in the same manner as in section 5.2.3. The parameters for data acquisition of EPR spectra were as follows: scanning field 10 mT, magnetic field modulation 0.08 mT, modulation frequency 90 kHz, field scanning duration 1 s, time constant of the lock-in amplifier 1 ms, data sampling 1024 points per field scanning, and incident RF power to the resonator approximately 4 mW.

5.2.5. Phantom imaging

To demonstrate parallel image-acquisition without saturation of the EPR signal intensity, 3D EPR images of a tube phantom were obtained. The phantom consisted of two quartz tubes (outer diameter 5 mm, inner diameter 4 mm) placed in parallel with a distance of 6 mm between the centers of the tubes. The tubes were filled with 2 mM 2,2,6,6-tetramethylpiperidine-d_{16}-1-oxyl (perdeuterated Tempone) aqueous solution. The

field-of-view (FOV) was set to 100 mm. The parameters for EPR imaging were as follows: scanning field 10 mT, magnetic field gradient 100 mT/m, magnetic field modulation 0.08 mT, modulation frequency 96 kHz, field scanning duration 1 s, time constant of lock-in amplifier 1 ms, applied RF power 6.9 mW for channel 1 at 783 MHz and 6.3 mW for channel 2 at 731 MHz, data sampling 512 points per field scanning, and number of projections 181. The total image-acquisition time was 3 min. The one-step 3D filtered-back projection method was used in image reconstruction for individual surface coils [5.19]. Since there was considerable noise in the EPR spectral baseline when the modulation frequency was set to 90 kHz, as in the other experiments, on the day the tube phantom imaging was performed, the modulation frequency was set to 96 kHz so that the noise level was almost the same as in the other experiments.

5.2.6. In vivo EPR imaging

To demonstrate the feasibility of *in vivo* parallel image acquisition, 3D EPR imaging was performed with a male C3H HeJ mouse (7 weeks old and weight 21 g). The subject mouse was anesthetized using isoflurane (4% induction and 1–2% to maintain) and intraperitoneally administered 300 μL of 300 mM 3-carbamoyl-2,2,5,5-tetramethylpyrrolidine-1-oxyl (3-CP) that was prepared in physiological saline solution. A subject mouse was placed on a bed in a prone position and covered by a polytetrafluoroethylene (PTFE) plate (0.5 mm thick) to suppress the noise derived from the heartbeat and respiration of the subject mouse [5.16]. For better handling of the subject mouse in co-registration imaging, several lines were drawn on the PTFE plate to visually adjust the position of the subject mouse in the magnet. Image scanning for the subject mouse was performed over time to observe the temporal change in the distribution of 3-CP imaging agents. The protocol for this animal experiment was approved by the Hokkaido University

Animal Care and Use Committee. The parameters for *in vivo* EPR imaging were as follows: scanning field 10 mT, magnetic field gradient 60 mT/m, magnetic field modulation 0.2 mT, modulation frequency 90 kHz, field scanning period 0.5 s, time constant of lock-in amplifier 0.3 ms, applied RF power 4.4 mW for channel 1 and 4.0 mW for channel 2, data sampling 512 points per field scanning, and number of projections 126. The total image acquisition time was 1.5 min per 3D image. While the FOV was 167 mm in image acquisition, the image data within the FOV of 60 mm were used for the presentation in this paper.

5.2.7. Proton NMR imaging

A 7-Tesla proton nuclear magnetic resonance (NMR) imaging scanner (Unity/INOVA 300/183, Varian, Palo Alto, CA) was used to obtain an anatomical image of the subject mouse. The position of the subject mouse was adjusted so that the center of the FOV of NMR imaging was at the center of the surface coil array based on the lines drawn on the PTFE plate. The same subject mouse was anesthetized using isoflurane (4% induction and 1–2% to maintain) during NMR image scanning. In this image acquisition, a spin-echo multi-slice T_2-weighted sequence was used. The FOV was set to 60 × 60 mm. Parameters for proton NMR imaging were as follows: repetition time 2.5 s, echo time 80 ms, matrix size 256 × 256, number of excitations 4, and slice thickness 1 mm, with a total acquisition time of approximately 45 min.

5.2.8. EPR/NMR image co-registration

EPR/NMR image co-registration was performed to identify the locations of the distribution of 3-CP obtained by EPR imaging on an anatomical map of the subject mouse. All EPR slice-selective images in the XY-plane (sagittal plane) were generated at the center of the combined 3D image each time. To suppress the noise and artifacts in the EPR images,

the threshold of noise suppression was set to 30% of the maximum intensity of all slice-selective EPR images. The FOV of the slice-selective EPR images was adjusted to that of the NMR image, and the EPR image was overlaid on the NMR image.

5.3. Results

5.3.1. Saturation of EPR signals

Figure 5.3 shows the relation between the EPR signal intensity and the square root of RF input power with and without the second amplifier. As shown in Fig. 5.3A, when the second amplifier was placed in the RF bridge, the EPR signal intensity was proportional to the square root of the RF input power when a single resonator was fed, whereas the EPR signal intensity did not increase when the incident RF power was more than around 0.4 mW when both resonators were fed simultaneously. This means that the receiver system in the EPR spectrometer was saturated under simultaneous feeding [5.18]. In contrast, when the second amplifier was removed from the RF bridge, the signal intensity was not saturated with an increase in the incident RF power regardless of simultaneous feeding (Fig. 5.3B).

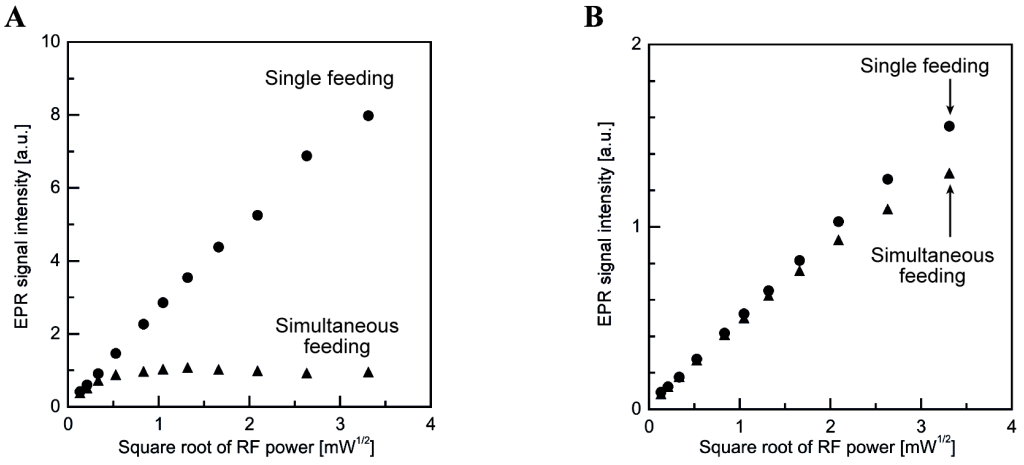


Fig.5.3. EPR signal amplitudes as a function of the RF power applied to the resonator(s). (A) Relation between the EPR signal amplitudes and the incident RF power was measured under signal-resonator feeding and simultaneous feeding with the second amplifier. (B) That relation was also measured without the second amplifier.

However, the linearity of the EPR signal intensity was slightly decreased beyond an incident RF power of 1 mW compared with the signal intensity under single-resonator feeding.

5.3.2. Effect of removing the second amplifier on the EPR spectrometer

Figure 5.4 shows a comparison of the SNRs of measured EPR spectra, i.e., the EPR signal intensity and the noise levels of individual EPR spectrometers with and without the second amplifier. All of the graphs in Fig. 5.4 show the mean of 100 spectra with the standard deviation for the SNR, the signal intensity, and the noise. In both channels, while there were differences in the SNRs with and without the second amplifier, the differences in the SNRs were smaller at higher levels of RF power. In Fig. 5.4A, for the EPR spectrometer assigned to channel 1, although the SNRs before the second amplifier was removed were higher than those after the second amplifier was removed at low incident RF powers, the SNRs after the second amplifier was removed were almost the same as those before the second amplifier was removed for an incident RF power of greater than 5.5 mW. In terms of the EPR signal intensity in channel 1 (Fig. 5.4B), the EPR signal intensity after the second amplifier was removed was approximately 10% of the EPR signal intensity before the second amplifier was removed at all values of incident RF power. For the noise level in channel 1 (Fig. 5.4C), although the noise levels before the second amplifier was removed increased in accordance with the incident RF power, the noise levels after the second amplifier was removed remained at the same level for all values of incident RF power. The same tendency was observed for channel 2 regarding the SNRs and signal intensity (Figs. 5.4D-5.4F).

Figure 5.5 shows a comparison of the SNRs, the EPR signal intensity and the noise levels measured under single-resonator feeding and simultaneous feeding, before and after removal of the second amplifier. All of the graphs in Fig. 5.5 show the mean of 100 spectra with the standard deviation for the SNR, the signal intensity, and the noise. With the second

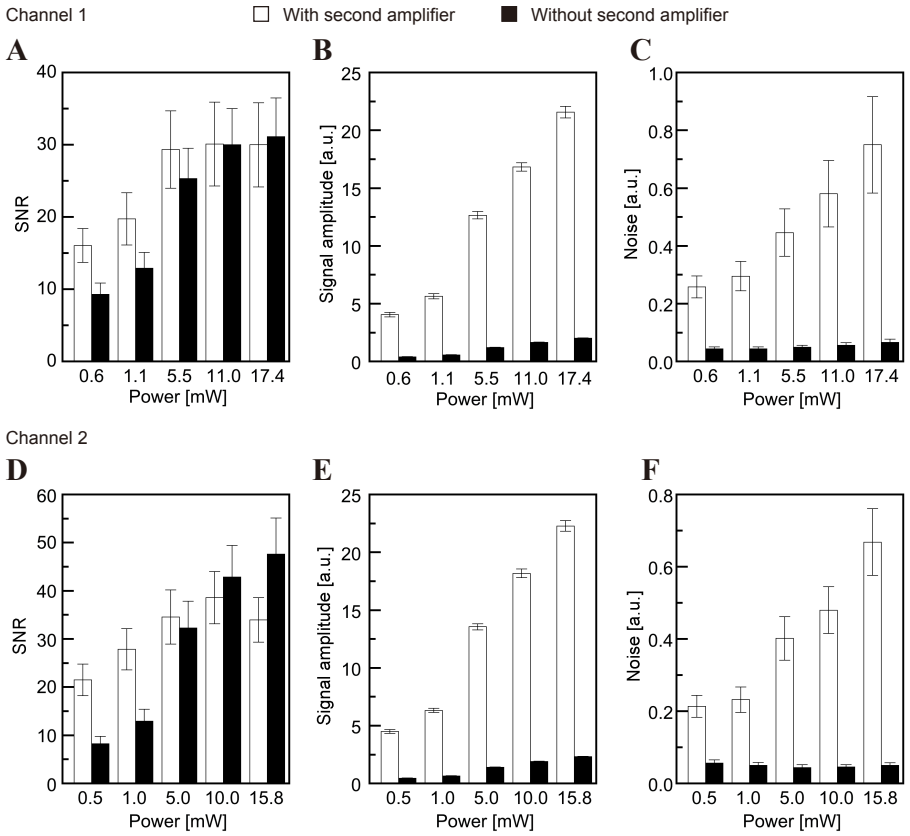


Fig. 5.4. Characteristics of measured EPR signals with and without the second amplifier. (A) The signal-to-noise ratio (SNR), (B) EPR signal amplitude, and (C) noise of EPR spectra measured with channel 1 are represented. Also (D) the SNR, (E) EPR signal amplitude, and (F) noise of EPR spectra measured with channel 2 are represented.

amplifier, the SNRs under parallel detection decreased to approximately 40% of those under single feeding in both channels, as shown in Fig. 5.5A. As shown in Fig. 5.5B, the EPR signal intensity under simultaneous feeding was also significantly decreased compared to that under single-resonator feeding in both channels. Specifically, the EPR signal intensities for each channel were decreased to approximately 20% (channel 1) and 30% (channel 2) of those under single feeding. The noise levels for each channel were also decreased to 44% and 78% of those under single feeding, respectively (Fig. 5.5C). In contrast, when the second amplifiers were removed, the reduction in the SNRs under parallel detection was smaller than that before the second amplifier was removed for both channels (Fig. 5.5A). While the SNRs under simultaneous feeding were approximately 70% of those under single feeding, the EPR

signal intensities under simultaneous feeding were not decreased compared to those under single feeding (Fig. 5.5B). However, the noise levels under simultaneous feeding were increased by approximately 30% and 40% compared to those under single feeding (Fig. 5.5C).

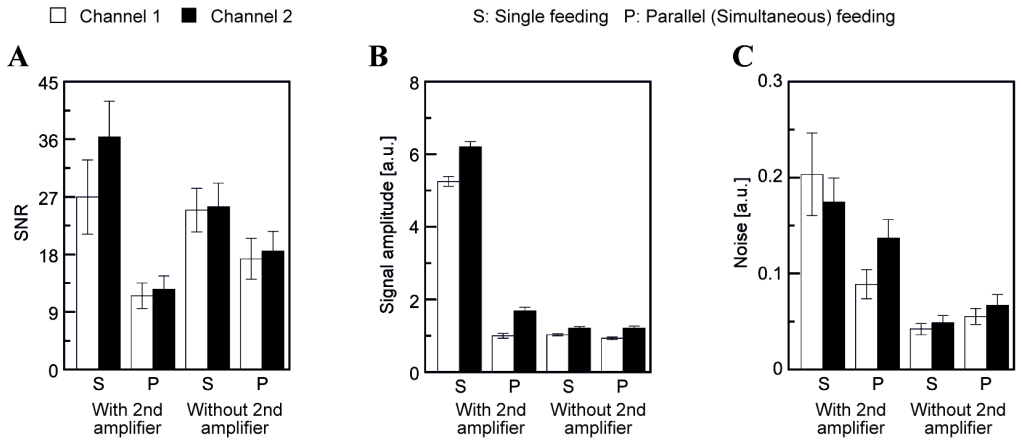


Fig. 5.5. Difference in the SNR, EPR signals, and noise between the conditions of single-resonator feeding and parallel (simultaneous) feeding. (A) The SNR, (B) EPR signal amplitude, and (C) noise were measured with and without the second amplifier.

5.3.3. Phantom imaging

Figure 5.6 shows the results of 3D EPR imaging of the phantom and slice-selective images. Figure 5.6A illustrates the arrangement of the phantom tubes. The FOV of 3D images was 30 mm and was a central region of the reconstructed image with a FOV of 100 mm. Surface-rendered images obtained with the individual channels are shown in Fig. 5.6B. The combined image of these two images is shown in Fig. 5.6C. Figure 5.6D shows slice-selective images in the XY-, XZ- and YZ-planes. For the XY-plane, two slice-selective images were obtained at the position of each tube. The threshold of slice-selective images was set to 50% of the maximum intensity of its 3D image. The subject size measured from slice-selective images was approximately 3.0 mm in diameter and 16.5 mm in length.

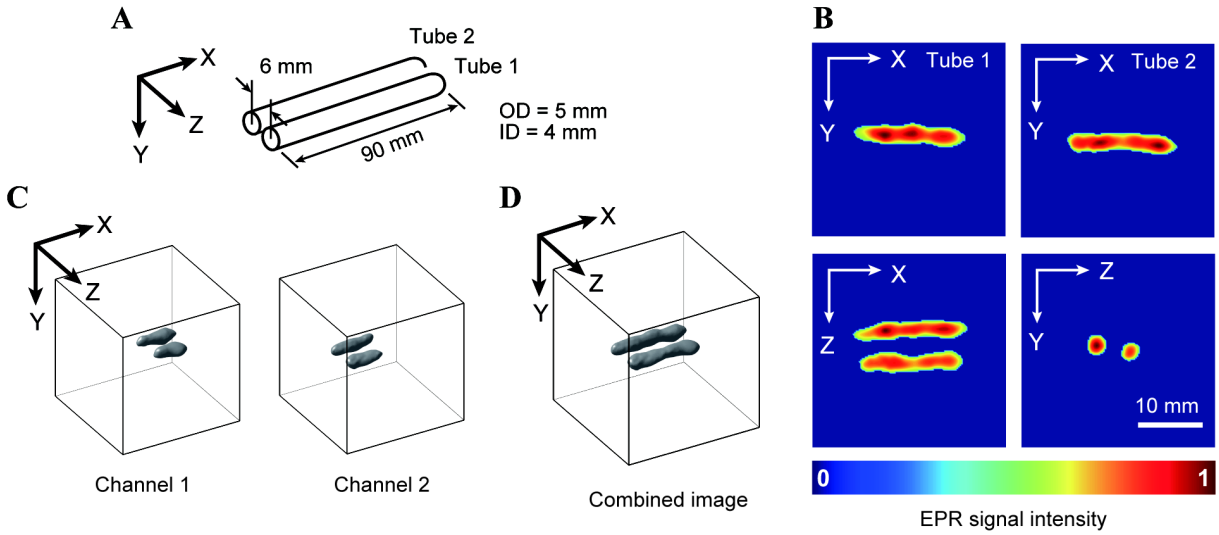


Fig. 5.6. EPR imaging of the tube phantom. (A) The arrangement of two tubes filled with 3-CP solution, (B) surface-rendered images of channel 1 and channel 2 in the parallel detection scheme, (C) the combined image by two images in panel C, and (D) slice-selective images of the phantom tubes.

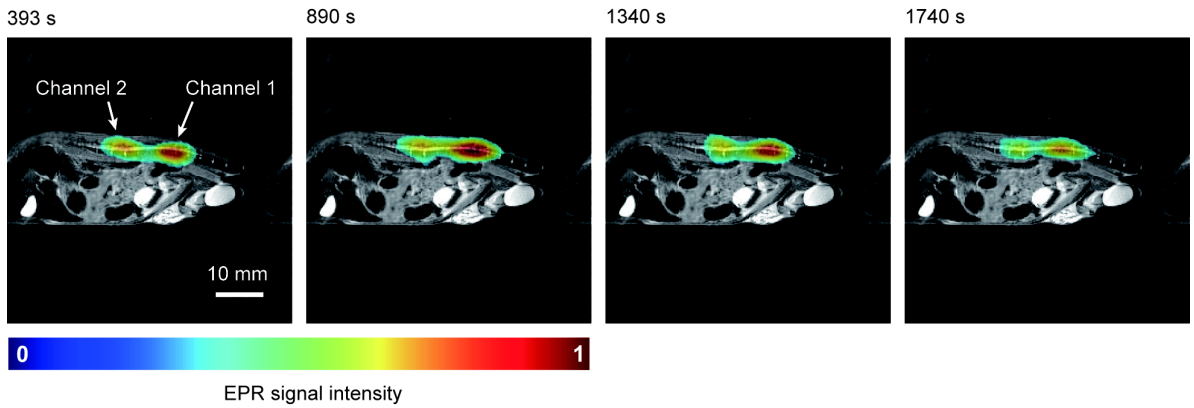


Fig. 5.7. Time-course of EPR/NMR co-registration images of 3-CP in the subject mouse. The times above the images are the starting time of the measurements after the injection of 3-CP imaging agent. FOV of both EPR and NMR images is 60 mm. EPR image intensities were normalized by the maximum signal intensity in the series of the images.

5.3.4. In vivo imaging

Figure 5.7 shows the temporal change in the distribution of the imaging agent (3-CP) on NMR images of the subject mouse (sagittal plane). The times shown above the images represent the starting time of image acquisition. Slice-selective EPR images were generated from combined 3D EPR images. The FOV of EPR images was 60 mm, since the FOV of the

NMR image was set to 60 mm. The EPR signal intensities were normalized by the maximum value of all EPR images. The depth of the visualized area of EPR signals from 3-CP was approximately 4.5 mm in the subject mouse. The signal intensity of channel 1 decreased over time. For channel 2, the signal intensity slightly increased but then decreased after 1340 s.

5.4. Discussion

The experimental results showed that the SNR of measured EPR spectra under the parallel detection scheme could be improved by eliminating the saturation of the RF amplifier in the RF bridge. As shown in Fig. 5.3B, the EPR signal intensity was not saturated under simultaneous feeding when the second amplifier was removed from the RF bridge. However, the linearity of the signal intensity under simultaneous feeding was slightly lower than that under single-resonator feeding. Since the signal intensity did not decrease when the saturation of the EPR signal intensity was completely eliminated, the signal intensity was slightly saturated beyond an RF power of 1 mW in channel 1 under simultaneous feeding in Fig. 5.3B. However, the EPR signal intensity in channel 2 was not saturated when the incident RF power was less than approximately 10 mW (data not shown). While the same RF components were used for the RF bridges of both channels, the tendency of saturation was slightly different for channel 1. The 1 dB compression point of the first amplifier in channel 1 might be lower than that of the first amplifier used in channel 2. In addition, with regard to the transmission coefficient, since the RF power leakage from channel 2 to channel 1 was approximately 4 dB larger than that from channel 1 to channel 2, it was easier for the signal intensity on channel 1 to be saturated than that on channel 2. Despite this saturation tendency, the decrease in signal intensity on channel 1 under simultaneous feeding was less than 20% of the signal intensity under single feeding with the incident RF power used in this study (Fig. 5.3B).

The SNR was not significantly affected by the presence of the second amplifier when a higher RF incident power was applied, although a decrease in the signal intensity was observed when the second amplifier was removed, as shown in Fig. 5.4B. The signal intensity without the second amplifier was decreased to 10% of that with the second amplifier. Since the measured power gain of the second amplifier was 21 dB, which means that the input voltage was amplified 11.2-fold, the decrease in signal intensity after removal of the amplifier was reasonable. In addition, the noise levels were decreased to 10% to 20% of that when the second amplifier was used. Moreover, the increase in the noise level with a higher incident RF power was modest when the second amplifier was removed (Fig. 5.4C), compared with the increase in the noise level before removal of the second amplifier.

As shown in Fig. 5.5C, while the significant reduction in the SNR was eliminated by removal of the second amplifier, the SNR still decreased 30% under simultaneous feeding, compared with that under single feeding. While the signal intensities of both channels remained at almost the same level under both single feeding and simultaneous feeding (Fig. 5.5B), the noise levels were slightly increased under simultaneous feeding in both channels (Fig. 5.5C). The increase in the noise level was mainly caused by RF signal leakage from the other channels. In contrast, the noise level was decreased under simultaneous feeding with the second amplifier (Fig. 5.5B). There may be some other reason for this reduction in noise when the second amplifier was used. To clarify the details of the reduction in noise, further studies with this EPR spectrometer will be needed [5.20].

To obtain a higher SNR under parallel detection, the RF power leakage from the other channel should be very low. Thus, an additional decoupling method could be required to decrease the transmission coefficient between the coils. For example, better decoupling between the coils could be achieved by using theoretical calculations for the electromagnetic fields or by inserting a decoupling interface (compensator) [5.21]. In addition to improving

the decoupling between the coils, it could be effective to use a low-noise amplifier (first amplifier) with an output 1 dB compression point that is higher than that used in this study to prevent saturation of the EPR signal intensity.

Due to the improvement in the SNR with parallel detection, the acquisition time was shortened because the measured EPR signals did not require averaging. As shown in Fig. 5.6C, the 3D image of the tube phantom was acceptable in terms of spatial resolution, since the two tubes could be distinguished from each other. In previous report on the proof of concept regarding the method of parallel detection (Chapter 4), the measured signals had to be averaged three times to obtain an adequate SNR in the resultant 3D image. Moreover, since it was possible to obtain sufficient SNRs in a short acquisition time in these experiments, the method of parallel detection in this study could be successfully used for *in vivo* EPR measurements. As shown in Fig. 5.7, the temporal change in the distribution of 3-CP in the subject mouse could be visualized *in vivo*. This result suggests that the method of parallel detection could be useful for observing the pharmacokinetics of exogenously injected imaging agents over a broader area of small animals. While the distribution of the signal intensity was almost homogeneous in slice-selective images of the phantom tubes, the slice-selective images in *in vivo* imaging were not as homogeneous. This observation could be due to the inhomogeneity of biological tissues or a difference in the characteristics of the channels. To increase the homogeneity of the image intensity, the inhomogeneity of the signal intensity for the individual channels needs to be compensated for by calculating the distribution of the electromagnetic fields in a mouse body.

5.5. Conclusions

In this study, the SNR of measured EPR spectra was improved by suppressing the saturation of the EPR signal intensity under simultaneous feeding for two channels. To

eliminate the saturation of EPR signals, the author removed one of the amplifiers in the RF bridge of each channel. Although the noise level was slightly increased due to leakage of the incident RF power from the other channel, the SNRs obtained by the parallel detection method were improved enough to reconstruct 3D EPR images without the need for signal averaging. The author also demonstrated the *in vivo* 3D imaging of 3-CP in a subject mouse with parallel detection. Although there are still technical issues, such as the homogeneity of the EPR signal intensity, the parallel detection scheme can be used for the visualization of a broader region in small animals.

References

[5.1] L. J. Berliner, H. Fujii, X. M. Wan and S. J. Lukiewicz, Feasibility study of imaging a living murine tumor by electron-paramagnetic resonance, Magn. Reson. Med. 4 (1987) 380–384.

[5.2] H. J. Halpern, D. P. Spencer, J. van Polen, M. K. Bowman, A. C. Nelson, E. M. E. M. Dowey and B. A. Teicher, Imaging radio frequency electron-spin-resonance spectrometer with high resolution and sensitivity for in vivo measurements, Rev. Sci. Instrum. 60 (1989) 1040–1050.

[5.3] S. Ishida, S. Matsumoto, H. Yokoyama, N. Mori, H. Kumashiro, N. Tsuchihashi, T. Ogata, M. Yamada, M. Ono, T. Kitajima, H. Kamada and E. Yoshida, An ESR-CT imaging of the head of a living rat receiving an administration of a nitroxide radical, Magn. Reson. Imaging. 10 (1992) 109–114.

[5.4] G. He, R. A. Shankar, M. Chzhan, A. Samouilov, P. Kuppusamy and J. L. Zweier, 1999 Noninvasive measurement of anatomic structure and intraluminal oxygenation in the gastrointestinal tract of living mice with spatial and spectral EPR imaging Proc. Natl. Acad. Sci. U. S. A. 96 4586–91

[5.5] F. Hyodo, S. Matsumoto, N. Devasahayam, C. Dharmaraj, S. Subramanian, J. B. Mitchell and M. C. Krishna, Pulsed EPR imaging of nitroxides in mice, J. Magn. Reson. 197 (2009) 181–185.

[5.6] N. Kocherginsky and H. M. Swartz, Chemical Reactivity of Nitroxides, in: N. Kocherginsky and H. M. Swartz (Eds.), Nitroxide Spin Labels, Boca Raton: CRC Press, 1995, pp 27–66.

[5.7] H. Sato-Akaba, H. Fujii and H. Hirata, Improvement of temporal resolution for three-dimensional continuous-wave electron paramagnetic resonance imaging, Rev. Sci. Instrum. 79 (2008) 123701.

[5.8] H. Sato-Akaba, Y. Kuwahara, H. Fujii and H. Hirata, Half-life mapping of nitroxyl radicals with three-dimensional electron paramagnetic resonance imaging at an interval of 3.6 seconds, Anal. Chem. 81 (2009) 7501–7506

[5.9] Z. Chen, L. A. Reyes, D. H. Johnson, M. Velayutham, C. Yang, A. Samouilov and J. L. Zweier, Fast gated EPR imaging of the beating heart: Spatiotemporally resolved 3D imaging of free-radical distribution during the cardiac cycle, Magn. Reson. Med. 69 (2013) 594–601

[5.10] B. Epel, C. R. Haney, D. Hleihel, C. Wardrip, E. D. Barth and H. J. Halpern, Electron paramagnetic resonance oxygen imaging of a rabbit tumor using localized spin probe delivery, Med. Phys. 37 (2010) 2553–2559.

[5.11] K. Takeshita, T. Takajo, H. Hirata, M. Ono and H. Utsumi, In vivo oxygen radical generation in the skin of the protoporphyria model mouse with visible light exposure: An L-band ESR study, J. Invest. Dermatol. 122 (2004) 1463–1470.

[5.12] G. He, A. Samouilov, P. Kuppusamy and J. L. Zweier, In vivo EPR imaging of the distribution and metabolism of nitroxide radicals in human skin, J. Magn. Reson. 148 (2001) 155–164.

[5.13] S. Petryakov, A. Samouilov, M. Chzhan-Roytenberg, E. Kesselring, Z. Sun and J. L. Zweier, Segmented surface coil resonator for in vivo EPR applications at 1.1 GHz, J. Magn. Reson. 198 (2009) 8–14.

[5.14] P. B. Roemer, W.A. Edelstein, C. E. Hayes, S. P. Souza and O. M. Mueller, The NMR phased array, Magn. Reson. Med. 16 (1990) 192–225.

[5.15] A. Enomoto and H. Hirata, Sequential CW-EPR image acquisition with 760-MHz surface coil array, J. Magn. Reson. 209 (2011) 244–249.

[5.16] A. Enomoto, M. Emoto, H. Fujii and H. Hirata, Four-channel surface coil array for sequential CW-EPR image acquisition, J. Magn. Reson. 234 (2013) 21–29.

[5.17] A. Enomoto, H. Hirata, S. Matsumoto, K. Saito, S. Subramanian, M. C. Krishna and N. Devasahayam, Four-channel surface coil array for 300-MHz pulsed EPR imaging: Proof-of-concept experiments, Magn. Reson. Med. 71 (2014) 853–858.

[5.18] A. Enomoto and H. Hirata, Parallel image-acquisition in continuous-wave electron paramagnetic resonance imaging with a surface coil array: Proof-of-concept experiments, J. Magn. Reson. 239 (2014) 29–33.

[5.19] H. Sato-Akaba, H. Fujii and H. Hirata, Development and testing of a CW-EPR apparatus for imaging of short-lifetime nitroxyl radicals in mouse head, J. Magn. Reson. 193 (2008) 191–198.

[5.20] S. Pfenninger, W. Froncisz, J. S. Hyde, Noise analysis of EPR spectrometers with cryogenic microwave preamplifiers, J. Magn. Reson. Ser. A. 113 (1995) 32–39.

[5.21] R. F. Lee, R. O. Giaquinto and C. J. Hardy, Coupling and decoupling theory and its application to the MRI phased array, Magn. Reson. Med. 48 (2002) 203–213

Chapter 6

Four-channel surface coil array for 300-MHz pulsed EPR imaging: Proof-of-concept experiments

6.1. Introduction

The concept of phased array coils in MR imaging was introduced by Roemer *et al.* [6.1] as an efficient approach to improve signal-to-noise ratio (SNR). In this approach, multiple smaller resonators, decoupled from each other, each covering a specific field of view (FOV) is used in place of a larger single resonator. Because smaller resonators will have superior sensitivity, though covering a smaller fraction of FOV, combining data from multiple resonators can in fact lead to overall improvement of SNR. The individual resonators can be operated simultaneously with as many receiver chains, or can be multiplexed and measured in an inter-leaved fashion. Such an array concept has now become very popular and modern MRI machines which have up to 64 or 128 receive channels to enable the use of arrays with large number of individual coil elements. This has also led to the development of parallel imaging modalities with special pulse sequences and partial k-space strategies to speed up the throughput of clinical imagers [6.2–6.6]. For small animal imaging, the use of phased array coils can replace the conventional bird-cage or other similar resonators [6.7,6.8].

While the use of array resonators has now become routine in several MR imaging applications, such strategies have not been attempted in time-domain electron paramagnetic resonance (EPR) imaging. Time domain EPR imaging, although conceptually similar in principles and methodology to MRI, was challenging to implement for *in vivo* applications because of the microsecond range relaxation times of the paramagnetic systems in comparison with that of the nuclei whose relaxation times are in the millisecond to seconds range. Therefore, nanoseconds excitation pulses, switches with nanoseconds time resolution for rapid

isolation, and quenching of transmit power are needed to minimize the resonator ringing which can otherwise outlive the duration of the free induction decay which typically last for a few microseconds. Resonators with very low *Q* and T/R isolators (diplexers) with fast switching in ~100 ns range are used in most systems. Apart from this, attempts to spatially encode paramagnetic systems with even mm resolution in small objects, few cm in diameter, require uniformly exciting and capturing frequency bandwidths in the order of tens of MHz which is a challenge. Pulse widths in the order of tens of nanoseconds and power levels of several hundred Watts are necessary. Small animal FT-EPR imaging modalities have been developed in the author's laboratory and elsewhere [6.9–6.16] in the time-domain mode and routine use of EPR imaging is being made in mouse models of tumor to study and map tumor hypoxia (regions of tissue where the pO_2 is less than 5 mmHg). The importance of mapping out tumor hypoxia stems from the fact that hypoxic tumor cells are about 3–4 times more resistant [6.17–6.19] to radiation and chemotherapeutic killing compared with normal cells, and a mapping of tumor hypoxia can help plan radiotherapy based on pO_2 levels and improve the prognosis of radiation treatment of cancer. In order to apply EPR imaging to larger animals and ultimately to humans, it is necessary to scale up the resonator volume/size. It will also be necessary to use much higher power (~kW) and much smaller pulse widths (~10 ns) which may lead to unacceptable specific absorption rate [6.20]. It is in this context that the author believes that array resonators will help make the transition from small animals to human subjects and topical imaging of tumors by Fourier transform electron paramagnetic resonance (FT-EPR). Array coils have been used effectively in MR imaging of the entire spinal cord, for example, in the study of multiple sclerosis [6.21]. In this chapter, the author described the use of planar surface coil array of 22 mm diameter as well as a pseudo volume resonator formed by four surface coils with adjacent pair arranged orthogonally. The results obtained demonstrate the feasibility of using such resonator configuration in FT-EPR imaging

and increase the size of the object being imaged without significantly increasing the rate of radiofrequency (RF) power deposition. Because each array element needs to transmit and receive only fractional FOVs, the individual bandwidth coverage is also reduced enabling the use of lower power and reasonable pulse widths.

6.2. Methods

6.2.1. 300 MHz spectrometer/imager

The 300 MHz FT-EPR imager operating in the laboratory and the way in which the author performed EPR imaging have been described in detail previously [6.22]. In brief, it consists of 10 mT electromagnet with an effectively uniform volume of 5 cm^3 field with field homogeneity of 10 ppm. Cylindrical parallel loop resonators [6.22–6.26] with sizes 25 mm diameter × 25 mm length and 25 mm diameter × 50 mm length are routinely used for mouse imaging. The magnet is also equipped with a three-axis gradient system capable of a maximum gradient of 40 mT/m in any direction. Single point imaging modality is used for image formation [6.9] where the system is subjected to pulses of 70 ns duration at 200 W and the free induction decays are collected in presence of gradients that are stepwise ramped from a −G to +G in ΔG steps. The magnetization measured at a particular time delay from the pulse in monitored as a function of rastering the gradients in either a plane (for 2D) or along all the Cartesian axes (3D) forms the k-space which upon 2- or 3-dimensional FT yields the image. Because the entire free induction decays are collected one can generate as many images as one needs as a function of delay from the pulse until the SNR becomes too low. The FOV of images are given by

$$\mathrm{FOV} = \frac{2\pi}{\gamma \Delta G \tau} \qquad (6.1)$$

where γ is the electron gyromagnetic ratio, ΔG is the gradient step, and τ is the delay from the

trailing end of the pulse. An increase in the number of steps will increase the image resolution proportionately. It will be possible to use a sequence of images as a function τ and generate images of identical FOV (by interpolation or other numerical methods [6.27]) with intensities weighted by the apparent relaxation time inline image from which one can obtain the pO_2 because inline image linearly depends on pO_2. The way in which quantitative oximetry is performed using FT-EPR and single point imaging has already been detailed previously [6.22,6.25].

The 300 MHz EPR imager used in this study is described earlier [6.11,6.22] and was used for the phantom and *in vivo* experiments with array coils. The array coil resonators (surface loops) used is illustrated schematically in Fig. 6.1. The resonator typically consisted of three or four surface coil elements. When a part of the resonator circuit is manually shorted by conductive wire, the resonance frequency of the resonator was shifted away from 300 MHz thereby suppressing mutual coupling between adjacent coils.

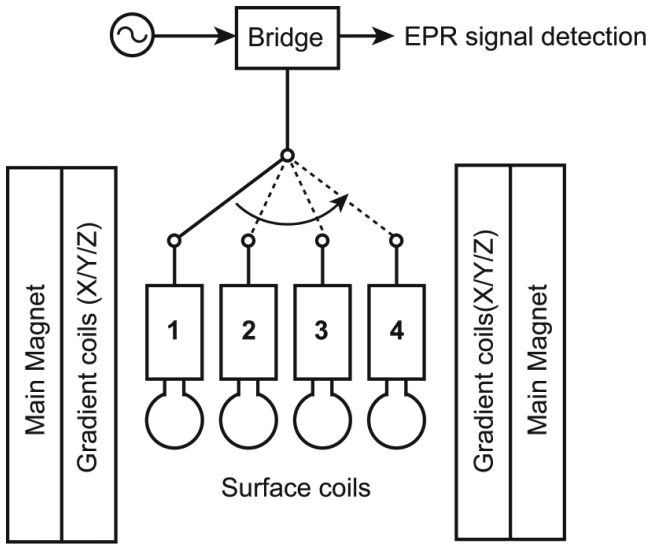


Fig. 6.1. Scheme of sequential pulsed EPR image acquisition. Surface coils were selected by sequentially connecting them one by one to RF source, whereas the others were shorted which let to frequency offset and minimization of coupling.

6.2.2. Individual Surface Coils

Figure 6.2 illustrates the configuration of the surface coil resonator. The resonator consists of a surface coil, parallel coaxial lines, and a balun constructed by half-wave line [6. 28–6.30]. Frequency adjustment was achieved by inserting the capacitors in series to the transmission line and changing the capacitive reactance using trimmer capacitors which are illustrated as C_T in Fig. 6.2. Impedance matching adjustment was also achieved by same way as the frequency adjustment using trimmer capacitors which are shown as C_{M1} and C_{M2} in Fig. 6.2. While *Q* was lowered mainly by over coupling, further reduction was achieved using a resistor in parallel to the transmission line. The surface coil was made from 18 AWG tinned copper wire. The coil diameter was 22 mm and the distance between centers of the coils was 16.5 mm to minimize coupling between each other. To electrically insulate the coils from each other, the coils were covered with heat shrink tube. The coupling circuit was made from copper laminate substrate.

Nonmagnetic chip capacitors (American Technical Ceramics, Huntington Station, NY)

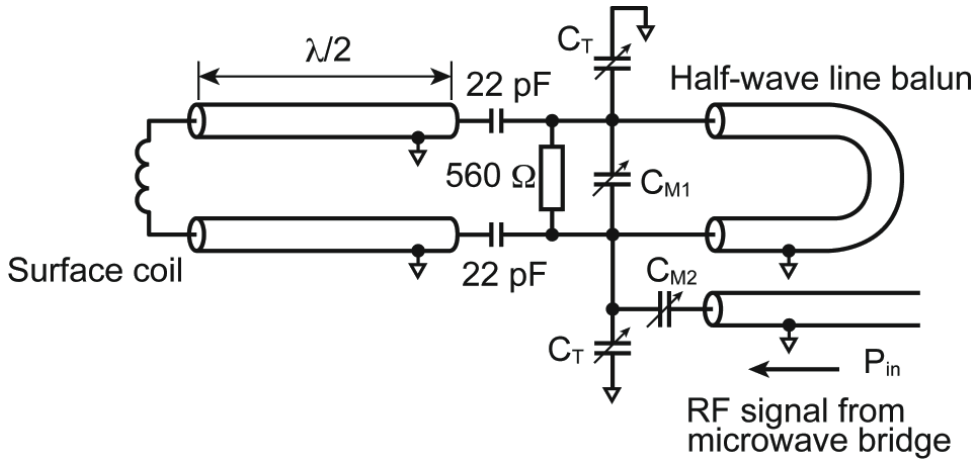


Fig. 6.2. Configuration of individual surface coil at 300 MHz. Parallel transmission line and a half-wave line balun were formed with 50-Ω coaxial lines. Trimmer capacitors were adjusted by adjusting the impedance matching between the resonator and the transmission line connected to the bridge. 560-Ω resistor was used to reduce the quality factor *Q* and the ringing time of the resonator.

and trimmer capacitors (Johanson Manufacturing, Boonton, NJ) were used in both tuning and impedance matching. To shift the resonance frequency of the "passive" coils, the end of the parallel transmission on the side of a coupling circuit was shorted as mentioned previously causing a considerable shift in the resonance frequency. The parallel transmission line and the half-wave balun were made from coaxial semi-rigid cables (model UT-141C-form, UT-141C-TP, Micro Coax, PA).

6.2.3. Chemicals

Triarylmethyl (Oxo63), methyl tris(8-carboxy-2,2,6,6-tetrakis-(2-hydroxyethyl)-benzo [1,2-d:4,5-d']bis[1,3]dithiol-4-yl), procured from GE Healthcare (Wauwatosa, WI) was used for all experiments in this article.

6.2.4. Animal Preparation

Female C3H mice were obtained from the Frederick Cancer Research Center, Animal Production (Frederick, MD 21702). The mouse was 12–16 week and weighed 27.2 g. Squamous cell carcinoma (SCC-VII) cells were implanted in the right hind leg of mouse and grown in 10 days. The tumor size was ~12.4 mm width, 14.2 mm length, and 11.0 mm thickness. The mouse was anesthetized using isoflurane® (induced at 3.0% and maintained at 1.5% in 750 mL/min medical air). Oxo63 (75 mM) was given as a 1.125 mmol/kg bolus followed by 0.04 mmol/kg/min continuous injection via tail vein cannulation and imaging was started immediately thereafter. Experiments were carried out in compliance with the Guide for the Care and Use of Laboratory Animal Resources (1996), National Research Council, and approved by the National Cancer Institute Animal Care and Use.

6.2.4. Phantom imaging

Fig. 6.3A, B shows the photographs of the resonator made of three coils elements and the phantom for 2D imaging. To investigate the area of visualization of the surface coil array, the author constructed a plane surface coil array using three resonators and measured 2D EPR images of a flat rectangular cuvette-like cell phantom (22 × 52 × 10 mm^3) filled with 3 mM Oxo63 aqueous solution. The parameters for 2D EPR imaging were as follows: FOV = 75 × 75 mm; maximum magnetic field gradient = 6.0 mT/m; applied microwave power = 100 W; number of projections = 361 (19 × 19 steps along X and Z directions in 0.66 mT/m steps); number of transients averaged = 10,000.

Figure 6.3C, D shows the photographs of the surface coils and the phantom used for 3D imaging, and Fig. 6.3E shows the resonator with four individual coils with their tuning and matching circuits. To obtain 3D images, the author configured the surface coil array like a volume coil using four resonators on the surface of a cylindrical polyethylene tune fixed with adhesive tape, and measured 3D EPR images of a cylindrical phantom (14.8 mm in diameter

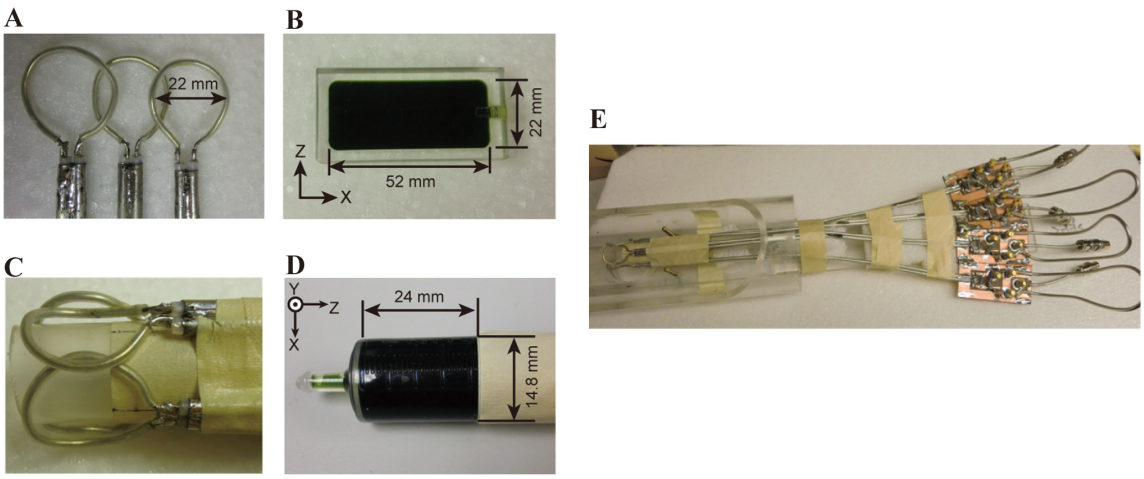


Fig. 6.3. Photographs of surface coil array and the phantoms. (A) Three-channel coil array for 2D imaging, (B) the rectangular cuvette-like phantom filled with Oxo63 solution, (C) four-channel coil array configured around a cylindrical polyethylene tune to simulate a cylindrical volume coil, (D) a syringe phantom filled with 3 mM Oxo63 solution, and (E) overall view of the surface coil array.

and 24 mm in length) filled with 3 mM Oxo63 aqueous solution. In 3D imaging with the surface coil array, four individual surface coils were placed and fixed with adhesive tape around a cylindrical plastic tube (21 mm in diameter). The parameters for 3D EPR imaging were the same as mentioned above for 2D imaging, except with 6859 projections (19 × 19 ×19 steps along the X, Y, and Z directions in 0.66 mT/m steps) and an FOV of 75 × 75 × 75 mm^3. *In vivo* measurements of the mouse leg tumor were also carried out by placing the tumor-bearing leg in the array coil assembly and using the same parameters. The 2D and 3D images were obtained by FT of k-space generated from a single time point at a delay of 700 ns from the pulse, after zero-filling to a matrix size of 64 × 64 and 64 × 64 × 64, respectively.

6.3. Results

6.3.1. Phantom imaging

To test the feasibility of using a set of array coils to image an object, which is larger than a component single coil, the author has performed both 2D and 3D imaging on phantoms. For 2D imaging of a large sized phantom depicted in Fig. 6.3B consisting of a flat rectangular glass cell filled with 3 mM Oxo63 solution was used. The diameter of the individual array coil was 22 mm, and three coils were arranged in a plane overlapping with each other over a region of 5 mm (Fig. 6.3A). The three coils were insulated from each other and each coil was used to capture the image from the phantom within its RF flux domain. Gradients were applied in a Cartesian raster parallel to the plane of the array in steps of 0.6 mT/m in the range +6 to -6 mT/m. Figure 6.4A shows the 2D EPR images of the flat rectangular cell obtained by single point imaging using the individual resonators in XZ-plane. Figure 6.4B shows the combined EPR image measured with the surface coil array. Before combining 2D EPR images obtained by individual resonators, they were normalized due to the differences in sensitivity between coils. The area of visualization in the individual images of Fig. 6.4A was

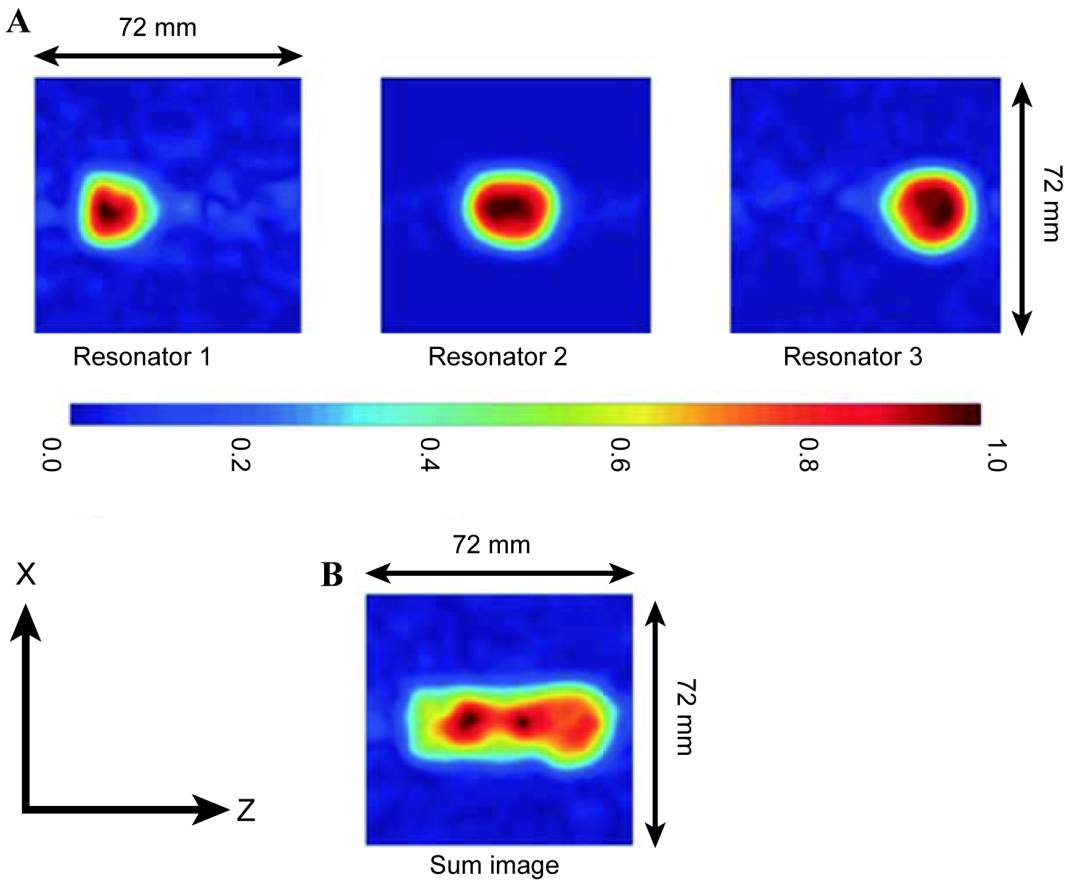


Fig. 6.4. 2D EPR images of a rectangular phantom with a "three-channel" surface coil. (A) Images from individual coils and (B) the combined image with scale factors based on the relative sensitivity of the coils.

approximately equal to the inner area of each coil, whereas the combined image Fig. 6.4B had the FOV larger than the phantom. The FOV of the image was 72 mm × 72 mm. Thus, it is possible to expand the effective FOV of the image to the total array area enabling larger objects to be imaged. Further, it is obvious that the power required should be much less than what would be required if single large coil was used.

To test the feasibility of using a combination of array coils to perform 3D imaging instead of a volume coil, the author used four surface coils placed on the surface of a cylindrical tube (Fig. 6.3C). Figures 6.5A–6.5D shows the surface-rendered 3D images of the phantom tube obtained by individual resonators. Figures 6.5E–6.5G shows the surface-rendered image combined from 3D EPR images measured with individual coils for various combinations. Although the individual images were not scaled, the combined image

(Fig. 6.5G) generated a smooth cylinder of dimension in satisfactory agreement to that of the actual phantom. Figure 6.5H–6.5J shows the slices from the 3D image along XY, YZ, and XZ planes generated from the combined image with dimensions correctly reproducing the distribution of the spin in the phantom. It is apparent from the figure that the RF flux does not reach far enough from the coil plane leading to a small cylindrical hole (indicated by an arrow) on the center of the combined image. This can be corrected either by scaling the individual images radially or by using a coil of larger radius. Nevertheless, this data suggests that it is possible to scale up EPR images to larger subjects by using multiple array coils.

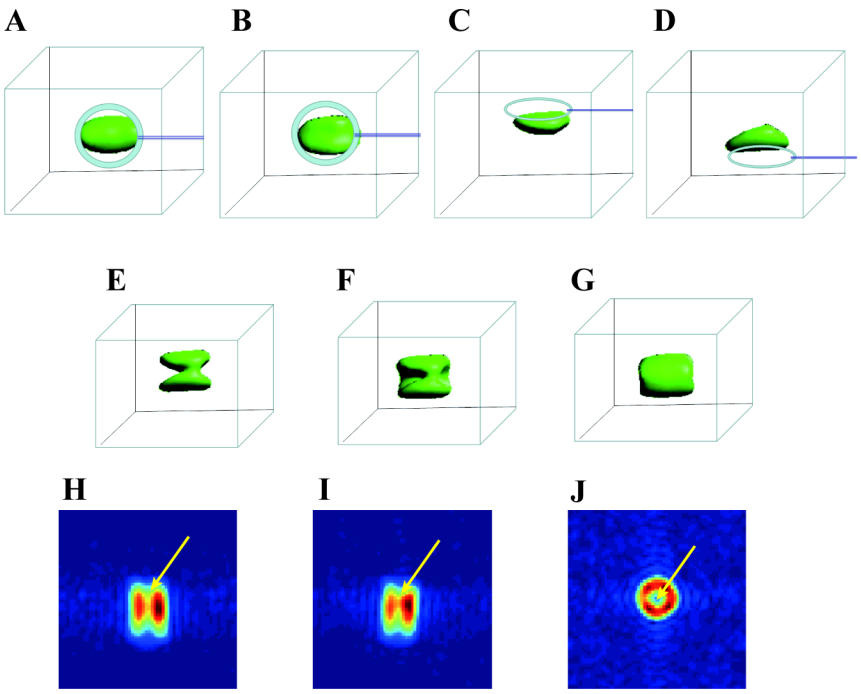


Fig. 6.5. EPR images measured from the tube phantom with four-channel surface coil array. (A)–(D): Surface-rendered images obtained with individual coils. Combined surface-rendered images [(E) is the sum of (C) and (D), (E) is the sum of (C), (D), and (B), and (G) is the sum all four individual images. Slices generated from the 3D image along mutually orthogonal axis are shown in (H)–(J). The central hollow region (see text) is indicated by the arrows.

6.3.2. In vivo imaging

Using the coil arrangement described above, 3D imaging of the tumor-bearing leg of C3H mouse was carried out. The positioning of the mouse leg in the Lucite enclosure surrounded by four surface coil resonators is shown in Fig. 6.6A. 3D image data was collected sequentially using each individual coil with the gradient increment step of 0.66 mT/m steps from +6 to -6 mT/m in 19 × 19 × 19 Cartesian raster. The free induction decay data from each coil were processed according to the procedure used for single point imaging. The surface-rendered 3D images from the individual coils are shown in Fig. 6.6B and a combined image obtained by summing the individual images is shown in Fig. 6.6C. Because the individual images are all measured under identical gradient settings taking care that the FOV covered by each element is large enough to cover the entire object, the resolution of the individual and the combined images are expected to the same.

Figure 6.6D shows a few slices through the composite 3D image of the mouse-leg tumor. These slices resemble what would be obtained from an actual image using a single volume coil suggesting that it is possible to perform 3D imaging using suitably configured surface coil array. Eventually, one can multiplex the coils or interleave the measurement using power levels that would be much less than what would be required if a single volume coil is used. The main motivation for this work is to demonstrate that if one has to scale up EPR imaging to larger subjects, the way to reduce specific absorption rate would be through the use of surface coil array and combining the images after suitable scaling. Further work is in progress to model the actual RF flux profile and to generate 3D scale factors that can reproduce the spin density correctly and enable T_2 or T_2^* based quantitative oximetry.

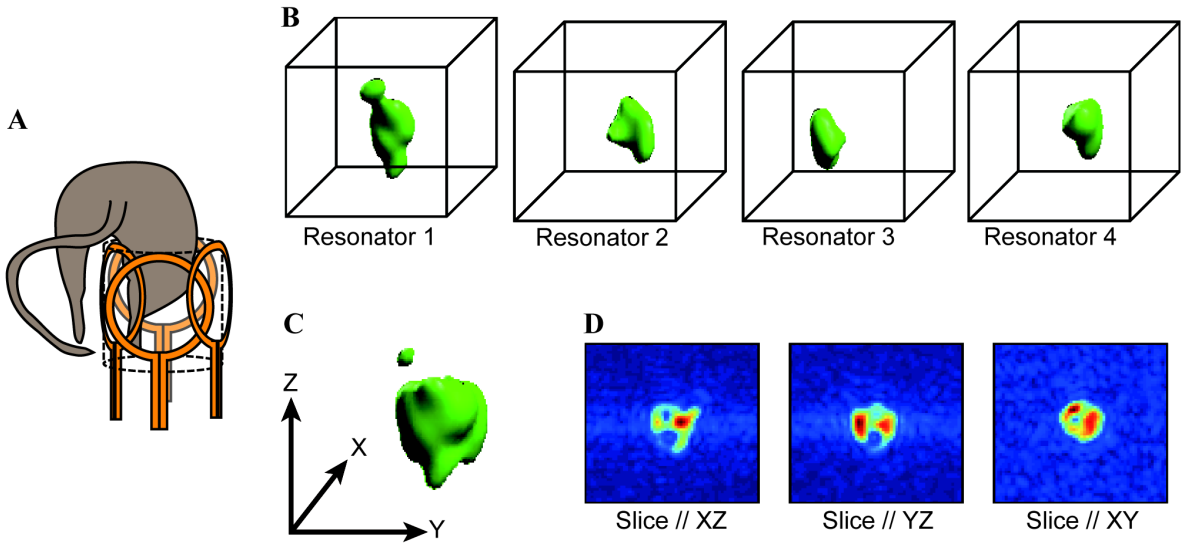


Fig. 6.6. EPR images of an SCC tumor bearing leg of a C3H mouse, measured with a surface coil array of four coils positioned on the surface of cylindrical tube mimicking a cylindrical volume resonator. (A) Schematic showing the positioning of the tumor-bearing leg inside the polyethylene tube surrounded by four surface coils. (B) Surface rendered 3D images from the individual coils. (C) Combined surface-rendered 3D image. (D) 2D slices of images generated from the combined image.

6.4. Discussion and conclusions

It is possible to use a combination of smaller surface coils to image a larger object compared with a single coil. It is also possible using appropriate configuration of the coils to emulate volume coils in an attempt to image large objects. This capability is useful in time-domain EPR imaging because the short transverse relaxation times of paramagnetic spin probes used for imaging (trityls, deuterated nitroxides, LiPc and derivatives) compels the use of resonators of low Q that will help shortening the resonator ring down time and allow capturing the time response within a fraction of a microsecond. On the same ground, it is also important to use pulses of 20–80 ns duration to cover the band width to be excited and detected even under moderate spatial encoding gradients. With the line widths of the spin probes on the order of 0.5 MHz, one needs to cover tens of MHz to have meaningful image resolution. This further imposes additional requirements on the power to be packed in

ultra-short pulses requiring 200–500 W amplifiers, depending on the volume of the resonator, even for small animal imaging. Scaling up of the imaging object (and hence the resonator volume) brings with it further increase in required pulse power leading to unacceptable specific absorption rate. Power reduction strategies using stochastic excitation [6.31,6.32] or specialized chirp sequences [6.33] have been tried in MR imaging. Another practical way to alleviate the increase in power requirements and at the same time scale up the object size (FOV) is by the use of multiple resonators, also a well-known development in the MRI field [6.1]. These coils may be phased array coils which are multiplexed and used sequentially in a time-shared fashion or in parallel using multiple receiver channels. The use of multiple array resonators is likely to be a solution to accomplish pulse EPR imaging of large objects and eventually human anatomy with acceptable specific absorption rate levels. The feasibility that is demonstrated here may well encourage extension of such a strategy to make time-domain EPR imaging a viable *in vivo* molecular imaging modality.

References

[6.1] P. B. Roemer, W. A. Edelstein, C. E. Hayes, S. P. Souza, O. M. Mueller, The NMR phased array, Magn. Reson. Med. 16 (1990) 192–225.

[6.2] J. W. Carlson, An algorithm for NMR imaging reconstruction based on multiple RF receiver coils, J. Magn. Reson. 74 (1987) 376–380.

[6.3] K. P. Pruessmann, M. Weiger, M. B. Scheidegger, P. Boesiger, SENSE: senitivity encoding for fast MRI. Magn. Reson. Med. 42 (1999) 952–962.

[6.4] M. A. Griswold, P.M. Jakob, R. M. Heidemann, M. Nittka, V. Jellus, J. Wang, B. Kiefer, A. Haase, Generalized autocalibrating partially parallel acquisitions (GRAPPA), Magn. Reson. Med. 47 (2002) 1202–1210.

[6.5] U. Katscher, P. Boernert, C. Leussler, J. S. van den Brink, Transmit sense, Magn. Reson. Med. 49 (2003) 144–150.

[6.6] B. P. Sutton, L. Ciobanu, X. Zhang, A. Webb, Parallel imaging for NMR microscopy at 14.1 Tesla, Magn. Reson. Med. 54 (2005) 9–13.

[6.7] C. E. Hayes, W. Edelstein, J. Schenck, O. M. Mueller, M. Eash, A highly homogeneous radiofrequency coil for wholebody NMR imaging at 1.5 T, J. Magn. Reson. 63 (1985) 622–628.

[6.8] P. Roeschmann, High-frequency coil system for a magnetic resonance imaging apparatus, US Pat 4, 746, 866, 1988.

[6.9] S. Subramanian, N. Devasahayam, R. Murugesan, K. Yamada, J. Cook, A. Taube, J. B. Mitchell, J. A. B. Lohman, M. C. Krishna, Single-point (constant-time) imaging in radiofrequency Fourier transform electron paramagnetic resonance, Magn. Reson. Med. 48 (2002) 370–379.

[6.10] S. Subramanian, J. W. Koscielniak, N. Devasahayam, R. H. Pursley, T. J. Pohida, M. C. Krishna, A new strategy for fast radiofrequency CW EPR imaging: direct

detection with rapid scan and rotating gradients, J. Magn. Reson. 186 (2007) 212–219.

[6.11] S. Subramanian, J. B. Mitchell, M. C. Krishna, Time-domain radio frequency EPR imaging. In: Berliner LJ, editor. Biological magnetic resonance, Vol. 18. New York: Kluwer Academic; 2003. pp 153–197.

[6.12] S. Subramanian, R. Murugesan, N. Devasahayam, J. A. Cook, M. Afeworki M, Pohida T, Tschudin RG, Mitchell JB, Krishna MC. High-speed data acquisition system and receiver configurations for time-domain radiofrequency electron paramagnetic resonance spectroscopy and imaging. J Magn Reson 1999;137:379–388.

[6.13] M. Elas, R. Bell R, D. Hleihel, *et al*. Electron paramagnetic resonance oxygen image hypoxic fraction plus radiation dose strongly correlates with tumor cure in FSA fibrosarcomas, Int. J. Rad. Oncol. Biol. Phys. 71 (2008) 542–549.

[6.14] M. Elas, B. B. Williams, A. Parasca, *et al*., Quantitaive tumor oxymetric images from 4D electron paramagnetic resonance imaging (EPRI): methodology and comparison with blood oxygen level-dependent (BOLD) MRI, Magn. Reson. Med. 49 (2003) 682–691.

[6.15] C. Mailer, V. S. Subramanian, C. A. Pelizzari, H. J. Halpern, Spin echo spectroscopic electron paramagnetic resonance imaging, Magn. Reson. Med. 55 (2006) 904–912.

[6.16] S. Subramanian, K. I. Matsumoto, J. B. Mitchell, M. C. Krishna, Radio frequency continuous-wave and time-domain EPR imaging and Overhauser-enhanced magnetic resonance imaging of small animals: instrumental developments and comparison of relative merits for functional imaging, NMR Biomed. 17 (2004) 263–294.

[6.17] J. M. Brown, Tumor hypoxia, drug-resistance, and metastases, J. Natl. Cancer. Inst. 82 (1990) 338–339.

[6.18] M. Hockel, K. Schlenger, B. Aral, M. Mitze, U. Schaffer, P. Vaupel, Association between tumor hypoxia and malignant progression in advanced cancer of the uterine cervix, Cancer Res. 56 (1996) 4509–4515.

[6.19] M. Hockel, P. Vaupel, Tumor hypoxia: definitions and current clinical, biologic, and molecular aspects, J. Natl. Cancer. Inst. 93 (2001) 266–276.

[6.20] SAR. ICNIRP guidelines for limiting exposure to time-varying elec- tric, magnetic and electromagnetic fields (up to 300 GHz), Health Phys. 74 (1998) 494–522.

[6.21] M. Filippi, T. A. Yousry, H. Alkadhi, M. Stehling, M. A. Horsfield, R. Voltz, Spinal cord MRI in multiple sclerosis with multicoil arrays: a comparison between fast spin echo and fast FLAIR. J. Neurol. Neurosurg. Psych. 61 (1996) 632–635.

[6.22] N. Devasahayam, S. Subramanian, R. Murugesan, F. Hyodo, K. I. Matsumoto, J. B. Mitchell, M. C. Krishna, Strategies for improved temporal and spectral resolution in in vivo oximetric imaging using time-domain EPR, Magn. Reson. Med. 57 (2007) 776–783.

[6.23] N. Devasahayam, S. Subramanian, R. Murugesan, J. A. Cook, M. Afeworki, R. G. Tschudin, J. B. Mitchell, M. C. Krishna, Parallel coil resonators for time-domain radiofrequency electron paramagnetic resonance imaging of biological objects, J. Magn. Reson. 142 (2000) 168–176.

[6.24] R. Murugesan, M. Afeworki, J. A. Cook, N. Devasahayam, R. Tschudin, J. B. Mitchell, S. Subramanian, M. C. Krishna, A broadband pulsed radio frequency electron paramagnetic resonance spectrometer for biological applications, Rev. Sci. Instrum. 69 (1998) 1869–1876.

[6.25] K. Matsumoto, S. Subramanian, N. Devasahayam, T. Aravalluvan, R. Murugesan, J. A. Cook, J. B. Mitchell, M. C. Krishna, Electron paramagnetic resonance imaging of tumor hypoxia: enhanced spatial and temporal resolution for in vivo pO_2

determination, Magn. Reson. Med. 55 (2006) 1157–1163.

[6.26] S. Matsumoto, H. Yasui, S. Batra, *et al*., Simultaneous imaging of tumor oxygenation and microvascular permeability using Overhauser enhanced MRI, Proc. Natl. Acad. Sci. USA. 106 (2009) 17898–17903.

[6.27] M. Halse, D. J. Goodyear, B. MacMillan, P. Szomolanyi, D. Matheson, B. J. Balcom, Centric scan SPRITE magnetic resonance imaging, J. Magn. Reson. 165 (2003) 219–229.

[6.28] A. Enomoto, H. Hirata, Sequential CW-EPR image acquisition with 760-MHz surface coil array, J. Magn. Reson. 209 (2011) 244–249.

[6.29] H. Hirata, G. He, Y. Deng, I. Salikov, S. Petryakov, J. L. Zweier, A loop resonator for slice-selective in vivo EPR imaging in rats, J. Magn. Reson. 190 (2008) 124–134.

[6.30] G. A. Rinard, R. W. Quine, S. S. Eaton, G. R. Eaton, Microwave coupling structures for spectroscopy, J. Magn. Reson. Part A. 105 (1993) 137–144.

[6.31] R. R. Ernst, Magnetic resonance with stochastic excitation, J. Magn. Reson. 3 (1970) 10–27.

[6.32] R. Pursley, J. Kakareka, G. Salem, N. Devasahayam, S. Subramanian, R. G. Tschudin, M. C. Krishna, T. J. Pohida, Stochastic excitation and Hadamard correlation spectroscopy with bandwidth extension in RF FT-EPR, J. Magn. Reson. 162 (2003) 35–45.

[6.33] B. Bluemich, Q. Gong, E. Byrne, M. Greferath, NMR with excitation modulated by Frank sequences, J. Magn. Reson. 199 (2009) 18–24.

Chapter 7

Decoupling and remote switching of four-channel coils in 300-MHz pulsed EPR imaging

7.1. Introduction

or studies in various disease models, highly sensitive measurements of a subject animal by electron paramagnetic resonance (EPR) imaging are needed. However, despite this demand, phased array coils have not yet been used in pulsed EPR imaging. In proton magnetic resonance imaging (MRI), phased array coils have often been used to obtain a large field-of-view (FOV), a higher signal-to-noise ratio (SNR), and better homogeneity of signal intensities over a broader area of a subject [7.1]. Phased array coils for use in MRI have been well documented [7.2, 7.3], and are used clinically for diagnosis of the human spinal cord, human brain, and other tissues [7.4-7.6]. Since the receive channels in a modern MRI scanner are separated from the transmit channels, multiple receive coils can be flexibly used in a parallel detection scheme. In contrast to multiple receive channels in MRI, a radiofrequency (RF) resonator can be used for both the transmit and receive channels in EPR imaging. For the use of a coil array in a pulsed EPR imager, two approaches are possible with respect to the data acquisition scheme. One approach is to separate the transmit coil(s) and the receive coil(s), as in MRI. Another approach is to drive multiple transmit/receive resonators sequentially without any modification of the pulsed EPR imaging system. However, it is challenging to apply the phased array coil concept of MRI to pulsed EPR imaging directly, since the ring-down time of the transmit coil(s) and the dead time of the receive channels are in the range of sub-microseconds. The resonator for pulsed EPR imaging requires a low quality (Q) factor of approximately 30 to accommodate the imaging bandwidth and minimize the dead time.

The author previously reported proof-of-concept experiments for a four-channel coil

array for 300-MHz pulsed EPR imaging using the sequential acquisition method (Chapter 6). In sequential data acquisition, the resonance frequencies of resonators were shifted to suppress mutual inductive coupling between neighboring coils when those resonators were not energized. In the surface coil array in continuous-wave (CW)-EPR imaging, a PIN diode switch was used to shift the resonance frequency of the resonator [7.7, 7.8]. The PIN diode switch enables the remote switching of the resonators electronically.

A fundamental question arose regarding active detuning of the resonators using PIN diodes or soldering pieces of metal wire between the transmission lines in the coil array in pulsed EPR imaging: is active detuning of the resonators really needed in a coil array for pulsed EPR imaging? Due to the low *Q*-factors and low coupling coefficients of the loop resonators, the author expected that reasonable decoupling of the loop resonators could be achieved in pulsed EPR imaging. If the mutual coupling among the loop resonators is not significant, the author should be able to remotely switch the loop resonators in a sequential acquisition scheme of pulsed EPR imaging without any active decoupling.

The purpose of this study was to assess the decoupling of a coil array due to low *Q*-factors in a 300-MHz pulsed EPR imaging. In this study, the author achieved decoupling between loop resonators without active shifting of their resonance frequencies and the suppression of spurious resonance peaks near the resonance frequencies. The author also demonstrated three-dimensional (3D) imaging of a phantom *in vitro* and a mouse tumor model *in vivo* with a coil array with the present decoupling method.

7.2. Methods

7.2.1. Configuration of a pulsed EPR imaging system

Figure 7.1 shows the configuration of the EPR imager and the four-channel coil array. The 300-MHz pulsed EPR imager at the National Cancer Institute was used for all

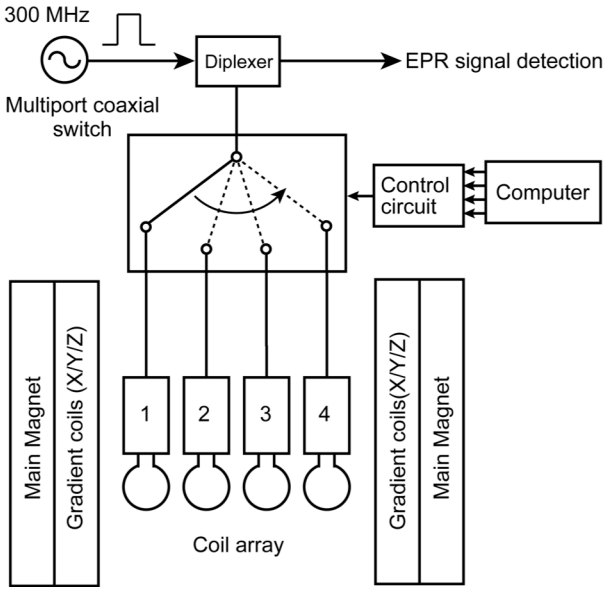


Fig. 7.1. Schematic diagram of the four-coil array and remote control of the coils.

experiments. The details of the 300-MHz pulsed EPR imager have been reported elsewhere [7.9]. The four-channel coil array consists of four loop resonators, a multiport coaxial switch (87104B, Agilent Technologies, Santa Clara, CA), and a switching control circuit. EPR data acquisition was sequentially performed by a personal computer. One of the resonators was selected by the signal from the computer through the switching circuit and the multiport coaxial switch. A Darlington transistor array (ULN2003, STMicroelectronics, Geneva, Switzerland) was used for the switching circuit to control the multiport coaxial switch. Under a certain gradient, the four coils were sequentially selected and image data were sequentially acquired with individual coils. After data acquisition, the gradient was changed and data acquisition with the four coils was performed under the new gradient as in the previous step [7.10]. The image data were stored for each channel for reconstruction of the individual images. Finally, the images were combined by the square root of the sum of the squares method.

For switching of the four coils, the resonance frequencies of all resonators were set to

300 MHz. Generally, the author required a method to prevent bimodal resonance characteristics due to mutual inductive coupling between the coils. In the pulsed EPR imager, a resonator with a low *Q*-factor of less than 30 was required to reduce its ring time [7.11]. When the *Q*-factor of the coils was low enough to satisfy this requirement, the influence of coupling between the neighboring coils on the reflection characteristics also decreased. Thus, bimodal resonance characteristics did not appear. Moreover, the coupling constant between coils was essentially low compared to when the coils were placed in the same plane because the adjacent coils are orthogonal and the opposite coils are sufficiently far apart. Based on these circumstances, it was possible to suppress bimodal resonance peaks.

7.2.2. Loop resonator

Figure 7.2 illustrates the circuit of an individual loop resonator. Each resonator has a single-turn loop, a parallel transmission line and a half-wave line balun [7.12]. To simplify impedance matching between the coil resonator and RF feeding line (50-ohm characteristic impedance), the author inserted a λ/4-length parallel transmission line composed of two coaxial lines between the coil and the coupling circuit (where λ is the wavelength of RF electromagnetic waves in the coaxial lines) [7.13, 7.14]. Capacitors were placed in series to

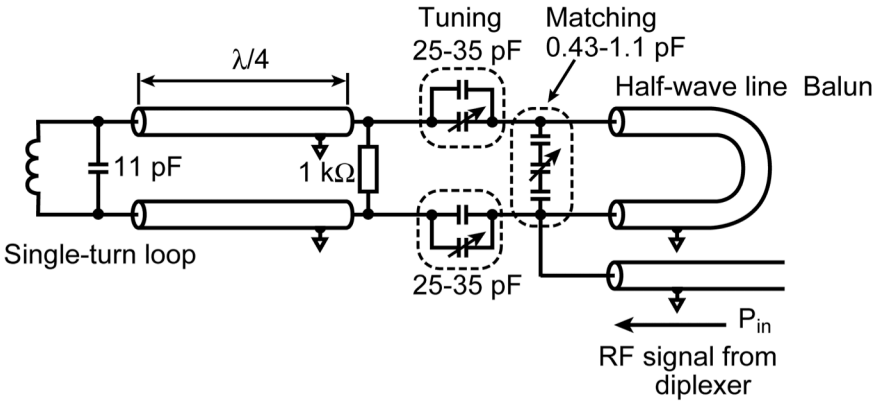


Fig. 7.2. Diagram of an individual loop resonator.

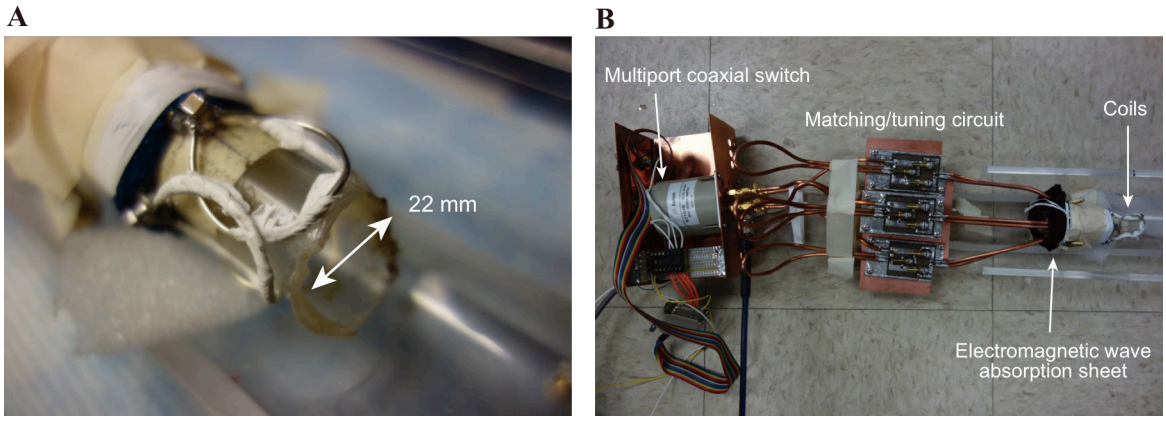


Fig. 7.3. Photographs of the constructed four-coil array. (A) Four coils around the phantom tube. (B) Photographs of the whole structure of the four-coil array and a multiport coaxial switch.

the transmission line for adjustment of the resonance frequency and in parallel to the transmission line for impedance matching. The resonance frequency was adjusted through the use of non-magnetic chip capacitors (American Technical Ceramics, Huntington Station, NY and Voltronics, Denville, NJ) and trimmer capacitors (Voltronics, Denville, NJ), so that the total capacitance can be varied from approximately 25 pF to 35 pF. Impedance matching of the resonator was adjusted in the same way as frequency adjustment, and the total capacitance was varied from 0.43 pF to 1.1 pF. A low Q-factor was achieved by the insertion of a chip resistor (1 kΩ) and overcoupling of the resonator to the feeding line [7.15]. The diameter of a single-turn loop was 22 mm, and four coils were placed around a plastic cylinder with an outer diameter of 22 mm, as shown in Fig. 7.3A. A single-turn loop was made from 18 AWG tinned copper wire and non-magnetic chip capacitors (American Technical Ceramics, Huntington Station, NY) were added to form a parallel LC-circuit. A copper laminated substrate (FR-4 equivalent, 34R, Sanhayato, Tokyo) was used for the coupling circuit. Each coil was wrapped with polytetrafluoroethylene (PTFE) tape to electrically insulate it from adjacent coils. The parallel transmission line and the half-wave line balun were made from 50-ohm non-magnetic semi-rigid coaxial lines (3.6 mm in

diameter, SC-358/50-SC, Coax Corp., Yokohama, Japan). As shown in Fig. 7.3B, the author wrapped the parallel transmission line with an electromagnetic wave absorption sheet (DFA-2.25, Nittobo, Tokyo, Japan) to prevent the leakage of RF signals from the coils to the outer conductors of the parallel transmission line that caused spurious resonance peaks near the excitation frequency.

7.2.3. Chemical

Oxo63, methyl tris(8-carboxy-2,2,6,6-tetrakis- (2-hydroxyethyl)-benzo [1,2-d:4,5-d']bis(1,3)dithiol-4-yl), was used for all experiments.

7.2.4. Phantom imaging

To demonstrate the feasibility of the switching of the four coils, the author acquired 3D EPR images of a cylinder phantom (14.8 mm in diameter and 35.5 mm in length) filled with 3 mM Oxo63 solution. In 3D pulsed EPR imaging, an acquisition protocol of single-point imaging was used [7.16]. The measurement parameters for 3D EPR imaging were as follows: FOV 50 mm, magnetic field gradient 6.0 mT/m, applied microwave power 200 W, number of projections 4913, with 50000 averages. The excitation pulse width was set to 60 ns and the repetition rate T_R was set at 8 μs.

7.2.5. In vivo mouse imaging

A tumor-bearing mouse was used for *in vivo* measurements. Squamous cell carcinoma (SCC-VII) cells were implanted in the right hind leg of a female C3H mouse (8 weeks old and weight 19.8 g). The tumor was approximately 10 mm wide, 10 mm long, and 12 mm thick when the author performed *in vivo* mouse imaging. The mouse right hind leg was placed in the coil array. The mouse was anesthetized using isoflurane (induced at 3.0% and

maintained at 1.5% in 750 mL/min medical air). Oxo63 was given as a 1.89 mmol/kg bolus followed by 0.03 mmol/kg/min continuous injection via a tail vein of the mouse. Animal experiments were performed in compliance with the Guide for the Care and Use of Laboratory Animal Resources (1996), National Research Council, and approved by the National Cancer Institute Animal Care and Use Committee. Measurement parameters for 3D EPR imaging of the tumor-bearing mouse were as follows: FOV 50 mm, magnetic field gradient 7.1 mT/m, applied microwave power 200 W, number of projections 4913, and total acquisition time 57 minutes with 20000 averages. The pulse width was set to 60 ns so that the flip angle was 90º to allow the repetition rate T_R to be 8 μs, which is lower than T_2^*.

7.3. Results

7.3.1. Construction of the coil array

Figure 7.4 shows the reflection characteristics (scattering matrix parameter S_{ii}, i = 1–4) of each coil resonator. The resonance frequencies of the individual resonators were 300 MHz and their Q-factors ranged from 25 to 30. Bimodal characteristics did not appear in any of the channels. In addition, resonance peaks caused by the leakage of electromagnetic waves from the coils did not appear in the reflection characteristics.

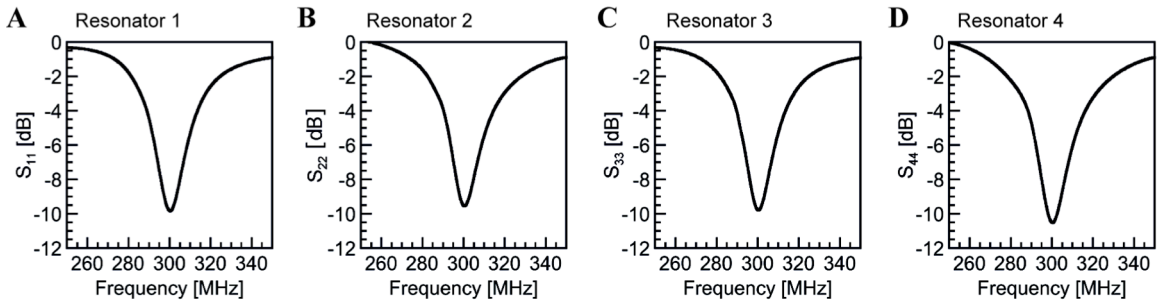


Fig. 7.4. Reflection characteristics of the individual resonators. Scattering-matrix parameters of each coil resonator, S_{11} of resonator 1 (A), S_{22} of resonator 2 (B), S_{33} of resonator 3 (C), and S_{44} of resonator 4 (D).

7.3.2. Phantom imaging

Figure 7.5 shows the results of 3D imaging of the phantom tube. Figure 7.5A shows a photograph of the phantom tube and the coils, and Fig. 7.5B shows individual images obtained with each coil. Figure 7.5C shows combined images merged with other individual images. Figure 7.5D shows slice-selective images in the XY-, XZ-, and YZ-planes obtained from the combined 3D image dataset (Fig. 7.5C). In all of the slice-selective images, the intensity at the center of the image was low due to an inhomogeneous RF magnetic field B_1 for the depth direction, which is related to the surface coil diameter. The diameter of the 3D image was approximately 15 mm and the length (Z-direction) was approximately 20 mm, which was similar to the dimensions of the measured phantom.

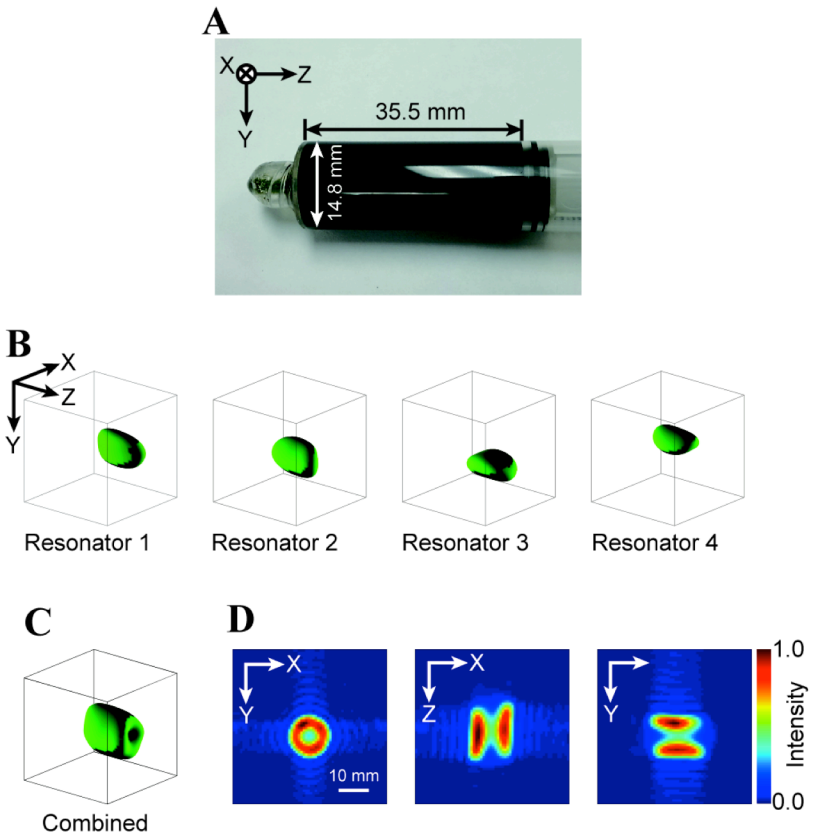


Fig. 7.5. Three-dimensional EPR imaging for the phantom tube. (A) Photograph of the tube containing OX063 solution, (B) EPR images obtained with each coil, (C) Combined 3D image, and (D) Orthogonal slices of images generated from the 3D data shown in Fig. 7.5(C).

7.3.3. In vivo imaging

Figure 7.6A illustrates the arrangement of the mouse hind leg and the four coils. Figures 7.6B and 7.6C show 3D images of the tumor-bearing right hind leg obtained with individual coils and the combined image, respectively. Figure 7.6D shows slice-selective images in the XY-, XZ-, and YZ-planes that were selected at the center of the four coils. The dimensions of the image of the tumor measured from the slice-selective images approximately matched the actual tumor size. As in the phantom measurements, there was a low-signal intensity region in the center of the subject image. The distribution of the signal intensity was stronger on the left side of the image in slice-selective images, although the signal intensity was almost the same as in the results with the phantom image.

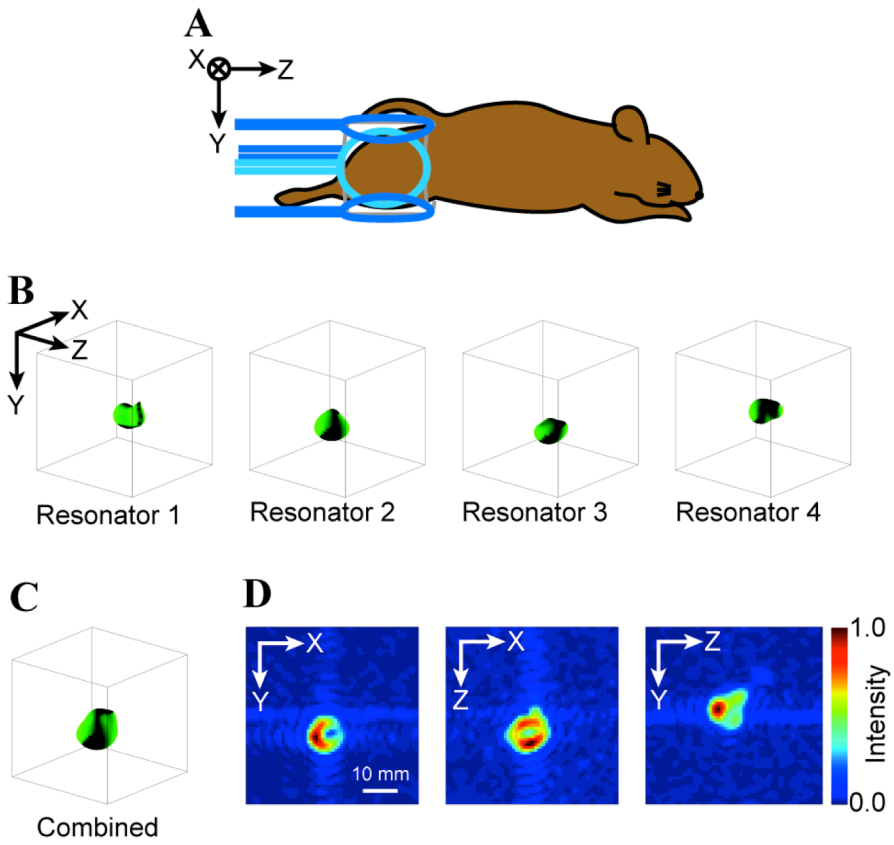


Fig. 7.6. *In vivo* 3D EPR imaging of a mouse tumor-bearing right hind leg. (A) Arrangement of the coils and the subject mouse, (B) EPR images obtained with each coil, (C) Combined 3D image, and (D) Slice-selective images generated from the 3D data shown in Fig. 6(C).

7.4. Discussion and Conclusions

As shown in Fig. 7.4, each coil showed single-peak resonance characteristics, which indicates that it was possible to passively decouple neighboring coils. Furthermore, the transmission coefficients between pairs of coils were all less than -12 dB (data not shown). Thus, this decoupling method that used the combination of low mutual coupling coefficients and low *Q*-factors was effective for use in a coil array in pulsed EPR imaging. The orthogonal coil arrangement used in this study resulted in low mutual coupling coefficients. In contrast to conventional decoupling methods for coils such as inductive decoupling or capacitive decoupling which require complicated calculations, with decoupling method suggested in this study it is easy to suppress mutual coupling between low *Q*-factor coils. In addition, spurious resonance peaks were not observed in the reflection characteristics of the coil resonators. If the electric fields around the single-turn loop for a coil are completely balanced, the leakage of RF signals to the outer conductors of the parallel transmission line should not occur. In reality, however, the coils were slightly deformed and the overlapping of the coils was not the same for all four coils. To prevent spurious resonance peaks near the excitation frequency caused by the leakage of RF signals, it is important to wrap the parallel transmission line with an electromagnetic wave absorption sheet.

With regard to 3D imaging of the phantom (Fig. 7.5), the author successfully obtained individual EPR images with four coils that were not actively decoupled. The author experimentally verified that active decoupling is not necessary in a coil array for pulsed EPR imaging. This result suggests that simple coil designs might be possible for pulsed EPR imaging, since low-field pulsed EPR spectroscopy and imaging require a low *Q*-factor of the resonator to overcome the problem of the dead time of data acquisition.

As shown in Figs. 7.5 and 7.6, although the dimensions of the images corresponded to the subject phantom, the intensity at the center of the image was low. This is because the

diameter of the coil was too small to store enough RF magnetic energy to reach the center of the phantom. While the use of larger-diameter coils should make it possible to detect signals from deeper within the subject, the efficiency of RF magnetic field generation decreases with an increase in the diameter of a coil. If the author considers the low *Q*-factor of the resonator for pulsed EPR imaging, the low efficiency of the coil should limit the coil diameter to obtain sufficient signal intensity. Thus, further investigations are required to visualize deeper within subjects using a coil array. In contrast to the switching method with a PIN diode switch used in a surface coil array for CW-EPR imaging [7.7, 7.8], no diodes were used in the circuit to switch the resonators in the coil array for pulsed EPR imaging. It is important to prevent additional signal loss due to decoupling of the circuits to improve the sensitivity of the resonator(s).

Switching of the coils using signals from a computer makes it possible to arbitrarily change the protocol for the timing of switching. In previous studies, timing could be switched by only a single method; i.e., resonators could be switched after a set of projection data was obtained for the entire acquisition of a single image with a single coil. However, with such a protocol, it was difficult to visualize a subject under the same conditions for all resonators, since there is a gap in time between the start of the first coil and that of the last coil. The time-consuming operation of sequentially switching the coils is disadvantageous for EPR imaging in live animals, since the reagents are rapidly reduced or metabolized. In contrast, with the measurement protocol in this study, involving interleaved use of all the coils, the author could visualize the subject under almost uniform conditions for all of the resonators with minimal influence from the pharmacokinetic elimination of the spin probe.

Despite the remote switching of the coils, the total acquisition time of animal imaging in this study was not so different from that in a previous study using manual switching due to the number of averagings. To obtain a SNR high enough to reconstruct the images, large

averagings are required for EPR imaging using a coil array because of the low sensitivity of the coils. Thus, the sensitivity of the coil array must be further improved to decrease the number of averagings. The sensitivity of the loop resonator could be improved by optimizing the circuit design with a 3D electromagnetic wave simulator [7.13]. Thus, it may be possible to increase the conversion efficiency of RF magnetic fields B_1 without increasing the Q-factor of the coil by optimizing the design of the coil array for pulsed EPR spectroscopy and imaging.

In conclusion, the author demonstrated sequential acquisition in 300-MHz pulsed EPR imaging with the remote selection of a four-coil array without the use of an active decoupling method. The low Q-factors for the four coils resulted in less mutual interference with neighboring coils. A better understanding of the decoupling characteristics of the coils described here might be useful for future considerations of parallel detection in pulsed EPR imaging.

References

[7.1] P. B. Roemer, W. A. Edelstein, C. E. Hayes, S. P. Souza, O. M. Mueller, Magn. Reson. Med. **16**, 192–225 (1990)

[7.2] R. F. Lee, R. O. Giaquinto, C. J. Hardy, Magn. Reson. Med. **48**, 203–213 (2002)

[7.3] M. A. Ohliger, D. K. Sodickson, NMR Biomed. **19**, 300–315 (2006)

[7.4] W.A. Willinek, J. Gieseke, M. von Falkenhausen, B. Neuen, H.H. Schild, C.K. Kuhl, Radiology **228**, 669–675 (2003)

[7.5] J. von Meyenburg, B. J. Wilm, A. Weck, J. Petersen, E. Gallus, J. Mathys, E. Schaetzle, M. Schubert, P. Boesiger, K. von Meyenburg, N. Goebels, S. Kollias, Radiology 267, 869–879 (2013)

[7.6] B. J. Hillman, S. E. Harms, G. Stevens, R. G. Stough, A. B. Hollingsworth, K. F. Kozlowski, L. J. Moss, Radiology 265, 51–58 (2012)

[7.7] A. Enomoto, M. Emoto, H. Fujii, H. Hirata, J. Magn. Reson. 234, 21–29 (2013)

[7.8] A. Enomoto, H. Hirata, J. Magn. Reson. 209, 244–249 (2011)

[7.9] N. Devasahayam, S. Subramanian, R. Murugesan, F. Hyodo, K. Matsumoto, J. B. Mitchell, M. C. Krishna, Magn. Reson. Med. 57, 776–783 (2007)

[7.10] J. S. Hyde, A. Jesmanowicz, W. Froncisz, J. B. Kneeland, T. M. Grist, J. Magn. Reson. 70, 512–517 (1986)

[7.11] N. Devasahayam, S. Subramanian, R. Murugesan, J. A. Cook, M. Afeworki, R. G. Tschudin, J. B. Mitchell, M. C. Krishna, J. Magn. Reson. 142, 168–176 (2000)

[7.12] A. Enomoto, H. Hirata, S. Matsumoto, K. Saito, S. Subramanian, M. C. Krishna, N. Devasahayam, Magn. Reson. Med. 71, 853–858 (2014)

[7.13] H. Sugawara, H. Hirata, S. Petryakov, P. Lesniewski, B. B. Williams, A. B. Flood, H. M. Swartz, IEEE Trans. Biomed. Eng. 61, 1894–1901 (2014)

[7.14] T. Haga, H. Hirata, P. Lesniwski, K. M. Rychert, B. B. Williams, A. B. Flood, H. M.

Swartz, L-band surface-coil resonator with voltage-control impedance-matching for EPR tooth dosimetry, Concepts Magn. Reson. B 43, 32–40 (2013)

[7.15] G. A. Rinard, R. W. Quine, S. S. Eaton, G. R. Eaton, W. Froncisz, J. Magn. Reson. Ser. A 108, 71–81 (1994)

[7.16] S. Subramanian, N. Devasahayam, R. Murugesan, K. Yamada, J. Cook, A. Taube, J. B. Mitchell, J. A. B. Lohman, M. C. Krishna, Magn. Reson. Med. 48, 370–379 (2002)

Chapter 8

Concluding remarks

The main purpose of this study was to extend the visualization area in EPR imaging, since the visualization area with a conventional surface coil is limited to the size of the coil. To make it possible to visualize a broader region, the author demonstrated the feasibility of a surface coil array for use in CW-EPR and pulsed EPR imaging. Surface coil arrays were developed based on the multiplexing of EPR signal detection in both the time domain and the frequency domain. For the development of a surface coil array, the suppression of mutual inductive coupling was the most important challenge that had to be solved. In addition to extension of the visualization area, the author showed that the surface coil array for EPR imaging was sensitive enough to perform *in vivo* measurements in mice.

Chapters 2, 3 and 4 demonstrate a surface coil array for 750-MHz CW-EPR imaging with the multiplexing of EPR signal detection in both the time domain and frequency domain. For a surface coil array with the multiplexing of EPR signal detection in the time domain, decoupling between adjacent coils was achieved by shifting the resonant frequency of each channel that was not being fed. Data acquisition was performed sequentially with individual coils. Since mutual inductive coupling between the coils was adequately suppressed by shifting the resonant frequency, the performance of each channel was not degraded compared with a conventional single surface coil. With a four-channel surface coil array, the author demonstrated that a surface coil array with the multiplexing of EPR signal detection in the time domain could be applied to *in vivo* EPR imaging. While a broader visualization area was realized with a surface coil array with multiplexing in the time domain without sacrificing the sensitivity, the acquisition time increased with the number of coils, which is a disadvantage for *in vivo* imaging.

To solve the problem of a long acquisition time, the author demonstrated a two-channel surface coil array which enables simultaneous data acquisition (parallel detection) in CW-EPR. For decoupling between the coils for parallel detection, the multiplexing of EPR signal detection in the frequency domain was used. For decoupling between the coils, the resonant frequencies of each channel were set to be approximately 50 MHz apart. Although a slight decrease in the SNR due to the leakage of incident RF power from the other channel was observed in parallel detection, it was possible to perform faster 3D imaging compared to the sequential method with a spatial resolution that was acceptable for use in *in vivo* EPR imaging. Based on these results, a surface coil array with the multiplexing of EPR signal detection in the frequency domain could be useful for EPR imaging of the whole body of small animals or large organs in humans, such as the skin. However, the leakage of RF power will become a more severe problem when the number of coils is increased in the future, since the total leakage of incident RF power from multiple channels will be greater than the leakage from just one channel. Thus, an additional method to decrease the transmission coefficient between the coils will be required to enhance the applicability of the parallel detection method.

Chapters 5 and 6 demonstrate the feasibility of a surface coil array for use in 300-MHz pulsed EPR imaging. A surface coil array for use in pulsed EPR imaging was realized by multiplexing of EPR signal detection in the time domain, similar to the surface coil array for CW-EPR in Chapter 2. Since the electronic components, including the PIN diodes, were not used for switching due to a high incident RF power, the resonant frequency was shifted manually each time switching was required. The performance of the surface coil array was sufficient to perform 3D EPR imaging of mice *in vivo.* However, since manual switching leads to a longer acquisition time and is less practical, another method for decoupling the coils was required for remote switching. Thus, the author proposed an alternative decoupling

method based on the characteristics of the resonators for pulsed EPR, i.e., a low *Q* factor and a low coupling coefficient derived from orthogonal arrangement of the surface coils. Since the resonant frequency of each channel did not need to be shifted with this decoupling method, remote switching of the coils was possible by selecting the channel with an RF switch. In addition, it was possible to perform 3D EPR imaging with the surface coil array. Thus, this study demonstrated the feasibility of using a surface coil array in pulsed EPR imaging for small animals. Moreover, it was possible to maintain the operating frequency for all of the channels of the surface coil array regardless of which channel was being fed. This result suggests that parallel imaging in pulsed EPR imaging may be possible in the future. However, since several tens of thousands of averagings were required to obtain EPR spectra in *in vivo* imaging, improvement of the sensitivity is an essential problem for the use of a surface coil array in pulsed EPR.

Although there are still some problems in the use of a surface coil array in both CW and pulsed EPR imaging, extension of the visualization area was achieved. In particular, for CW-EPR, the parallel detection method achieved fast EPR imaging over a broader area. The parallel detection method may become an important technique for *in vivo* EPR imaging using imaging agents with life-times that range from several minutes to several tens of minutes. In contrast to the method of parallel detection, since sequential EPR imaging is as sensitive as imaging with a single surface coil, this method could be advantageous for use in *in vivo* EPR imaging that does not require a short acquisition time, but does require high sensitivity, such as in animal experiments that use the continuous administration of imaging agents. Thus, if the remaining problems can be solved in the future, the technique of using a surface coil array for EPR imaging as proposed in this study should contribute to the various fields of study that use EPR imaging.

Publications and Honors

Peer-Reviewed Scientific Journals

1. **A. Enomoto,** K. Saito, S. Subramanian, M. C. Krishna , H. Hirata, N. Devasahayam, Decoupling and remote switching of four-channel coils in 300-MHz pulsed EPR imaging, ***Applied Magnetic Resonance*** (submitted) .
2. **A. Enomoto**, H. Hirata, Elimination of signal saturation under parallel detection in continuous-wave electron paramagnetic resonance imaging, ***Measurement Science and Technology*** (submitted).
3. **A. Enomoto**, H. Hirata, Parallel image-acquisition in continuous-wave electron paramagnetic resonance imaging with a surface coil array: Proof-of-concept experiments, ***Journal of Magnetic Resonance***, 239 (2014) 29–33.
4. **A. Enomoto**, H. Hirata, S. Matsumoto, K. Saito, S. Subramanian, M. C. Krishna, N. Devasahayam, Four-channel surface coil array for 300-MHz pulsed EPR imaging: Proof-of-concept experiments**,** ***Magnetic Resonance in Medicine***, 71 (2014) 853–858.
5. **A. Enomoto**, M. Emoto, H. Fujii, H. Hirata, Four-channel surface coil array for sequential CW-EPR image acquisition, ***Journal of Magnetic Resonance***, 234 (2013) 21–29.
6. **A. Enomoto**, H. Hirata, Sequential CW-EPR image acquisition with 760-MHz surface coil array**,** ***Journal of Magnetic Resonance***, 209 (2011) 244–249.

Conference Proceedings/Abstracts

1. **A. Enomoto** and H. Hirata, Feasibility Study of parallel image-acquisition in CW-EPR Imaging, Proceedings of Joint Annual Meeting of ISMRM-ESMEMB 2014, p. 2917, Milan, Italy (2014).

2. **A. Enomoto** and H. Hirata, Parallel image acquisition in CW-EPR imaging with surface coil array, The 52th Annual Meeting of The Society of Electron Spin Science and Technology, Saitama, 1J-07 (2012). (in Japanese)
3. **A. Enomoto**, H. Hirata, S. Matsumoto, K. Saito, S. Subramanian, M. C. Krishna, N. Devasahayam, Development of four-channel surface coil array for 300 MHz pulsed EPR imaging, EPR2013, Hanover, Th03 (2013).
4. **A. Enomoto**, M. Emoto, H. Fujii and H. Hirata, Development of four-channel surface coil array for 750 MHz CW-EPR Imaging, The 51th Annual Meeting of The Society of Electron Spin Science and Technology, Sapporo, 3B-14 (2012). (in Japanese)
5. **A. Enomoto** and H. Hirata, Four-channel surface coil array for 750-MHz CW-EPR Imaging, The 2nd International Symposium on Electron Spin Science, Matsushima, P27 (2012).
6. **A. Enomoto**, S. Subramanian, H. Hirata, M. C. Krishna, N. Devasahayam, Development of the surface coil array for pulsed EPR imaging, The 20th JSPS Core-to-Core Seminar: International Redox Core Symposium, Fukuoka, Japan (2012).
7. **A. Enomoto** and H. Hirata, Development of 4-Channel Surface Coil Array for CW-EPR Imaging, The 50th Annual Meeting of The Society of Electron Spin Science and Technology, Sendai, 2A-15 (2011). (in Japanese)
8. **A. Enomoto** and H. Hirata, Feasibility Study of a Surface Coil Array for CW-EPR, Imaging, The 49th Annual Meeting of The Society of Electron Spin Science and Technology, Nagoya, P-49 (2010). (in Japanese)
9. **A. Enomoto** and H. Hirata, Feasibility Study of Surface Coil Array for CW-EPR Imaging, EPR 2010, Puerto Rico, P-12 (2010).

Awards and Scholarship

2014 ***ISMRM Magna Cum Laude Merit Award***, Joint Annual Meeting of ISMRM-ESMRMB 2014, Milan, Italy.*

2013 ***Best Presentation Award***, The 52th Annual Meeting of the Society of Electron Spin Science and Technology, Saitama, Japan.

2012 ***Research Fellowship for Young Scientists***, Japan Society for the Promotion of Science (24-1486).

*ISMRM: International Society for Magnetic Resonance in Medicine

ESMRMB: European Society for Magnetic Resonance in Medicine and Biology

Acknowledgements

The author would like to express the author's deepest gratitude to Prof. Hiroshi Hirata. He has been the author's mentor and provided the author numerous supports, incisive comments and suggestions throughout the all of the author's undergraduate and Ph.D. training. The author could not have completed this study without his continuing and persistent help. The author would also like to thank Prof. Takashi Tateno and Prof. Tomomi Nemoto. They gave the author insightful comments and suggestions about this dissertation. The author also owes an important debt to Prof. Hirotada Fujii and Dr. Miho Emoto of Sapporo Medical University. They provided the author the technical help related to animal experiments and helpful advices. The author is really grateful to the members the Radiation Biology Branch at National Cancer Institute (NCI), National Institutes of Health (USA), Dr. Murali C. Krishna, Mr. Nallathamby Devasahayam, Dr. Sankaran Subramanian, Dr. Shingo Matsumoto and Dr. Keita Saito. They gave the author enormous technical supports related to pulsed EPR experiments, constructive comments and warm encouragement during and after the author's visit to NCI. Especially, Mr. Devasahayam and Dr. Matsumoto kindly supported the author for not only the author's study but also the author's stay in the United States. In addition, the author is grateful to Dr. Jonathan Goodwin who was a postdoctoral fellow at the EPR imaging group in Hokkaido University for a critical reading of a part of this dissertation.

The author is also deeply grateful to Ms. Ayumi Hishiyama who is the secretary of the author's laboratory for her various supports. Also the author wishes to thank the author's family and the author's best friends for their moral support and warm encouragement.

Finally, the author gratefully appreciates the financial support of Research Fellowship of the Japan Society for Promotion of Science for Young Scientists (24-1486) that made it possible to complete this doctoral study.